Acceleration sensitivity study on coupled resonators for designing anti-shock tuning fork gyroscopes

Praveen Singh Thakur

2014

Acceleration sensitivity study on coupled resonators for designing anti-shock tuning fork gyroscopes

by

Praveen Singh Thakur

A dissertation submitted in partial fulfillment
of the requirements for the degree of
Doctor of Engineering
(Micro Engineering)
in the Kyoto University
2014

Dedication

This thesis is dedicated to my parents santhosha and kishan singh, my brother naveen singh and sister in-law kavitha singh

Acknowledgements

I would like to express my deep appreciation and sincere gratitude to my mentors and advisors, Professor Osamu Tabata and Professor Toshiyuki Tsuchiya for their guidance, support, encouragement and financial support. I have been honoured to work under their supervision and learn from their advice and useful insights throughout my PhD program.
I would like to thank my dissertation defence committee members, Professor Takashi Hikihara and Professor Shinji Nishiwaki for their interest in my work. It has been a great privilege to benefit from their input and help in construction of my dissertation.
This research would not have been enabled without any single help and support that I had received from the other professors and each of my colleagues in Nano Micro System Laboratory at Kyoto University. Particularly; I would like to thank Professor Koji Sugano and Professor Yoshikazu Hirai for their discussions in lab meeting and help in the fabrication and valuable insights on my research. I also thank my former colleagues Tsujimoto, Mohammed, Tokusaki, Kataoka, Kitamura, Taniyama, nakano and Uesugi for their help and invaluable discussions in MEMS fabrication. In addition, I would like to thank all the staffs in the laboratory, Fuji, Honda, Watanabe, Matoba, Okino and Kawano for all their help. I would like to thank also the nano-hub staff for their help in clean room facility especially Sato, Inoue and Kanehira.
I like to thank my friends who made my life in Kyoto pleasant John, Muhannad, Bam, Chris, Akemi, Masako, Joseph, Lema, Titus, Nagendra kumar, Aman Arora, Mahesh, Kabir, Vijay and especially Fukui-san family and Tanaka-san family who cared like a family member.
Finally, I thank my bother, maheshwar and nagarjun for his invaluable support and encouragement. Last but not least, I wish to thank shoko, naoko and Akiko for all their help, support and positive attitude during the course of my Ph.D study.

Contents

List of figures

List of tables

Abstract

Acceleration sensitivity study on coupled resonators for designing anti-shock tuning fork gyroscopes

Gyroscopes are physical sensors that measure the angular motion of an object. The operation principle of vibratory gyroscopes relies on the transfer of energy between two vibration modes due to Coriolis effect. MEMS vibratory gyroscopes have successfully commercialized for consumer electronics and automotive applications due to small size, weight and cost. However, in automobiles, the harsh environmental conditions such as wide temperature range, high humidity, and severe vibrations demand high reliability for long operation time. For MEMS vibratory gyroscopes, one of the major issues for reliable operation is the acceleration sensitivity (acceleration output) that is false or error output caused by mechanical vibrations (accelerations). In automobile, since many sources of shocks and vibrations are existing and inevitable, vibratory gyroscopes, that detect a rotation by inertia force, are always susceptible to acceleration. A tuning fork gyroscope (TFG) is best suitable for this kind of application due to differential operation and common mode rejection. TFG usually have two vibration modes in the sense-axis, that are the in-phase and anti-phase modes. In the in-phase mode, two sense resonators move in the same phase and in the anti-phase mode, they move in 180^{o} phase difference. An ideal TFG should not have any acceleration outputs, since the sense resonators vibrate in anti-phase mode against Coriolis acceleration whereas linear acceleration causes identical motion (as in-phase mode), which is cancelled by differential amplifier as common-mode signal. However, there are no ideal or perfectly symmetric TFGs. TFGs indeed produce acceleration output. The cause of the acceleration output is attributed to stiffness unbalance due to fabrication error that results into different displacement amplitudes of two sense resonators which cannot be rejected by differential amplifier. But, there is no clear understanding on the detailed mechanism of source of acceleration sensitivity and reduction methods.

In this thesis, we identified the source of the acceleration output and proposed a method to suppress the acceleration output for designing anti-shock TFG. Similar to the quadrature vibration in a single-mass gyroscope, in which the driving vibration is coupled along the sensing axis, the sense in-phase vibration excited by linear acceleration would be coupled to the sense anti-phase vibration due to stiffness unbalance in the fabricated TFG. It is not possible to distinguish whether the sense anti-phase vibration is excited due

to Coriolis acceleration or external linear acceleration. The anti-phase vibration will appear on the gyro output as acceleration output. In addition, we have proposed a method to reduce the anti-phase vibration by decoupling two modes in sense resonators (frequency decoupling) to suppress the coupling between modes like the way designing the drive and sense resonators with independent suspension beams to minimize the quadrature coupling. In the proposed frequency decoupling method, which is "sense in-phase mode (ω_{in}) should be separated as far as possible from the sense anti-phase mode (ω_{anti})", anti-phase frequency is kept constant. The large frequency decoupling (decoupling ratio, $DR=(\omega_{anti}-\omega_{in})/\omega_{anti}$) value implies two modes separated largely. By using the decoupling method, large *DR* designs shows smaller anti-phase vibration amplitude (or acceleration output). The main advantage of the decoupling method is that it does not change the rate sensitivity of TFG. The other merits compared to conventional techniques is a simple designing that results in no increase in the device space compared to traditional methods such as inserting mechanical low-pass filters. To verify the source of acceleration output and frequency decoupling method, theoretical and numerical analysis is carried out on a TFG, and, simulations and experiments were carried out on in-plane and out-of-plane coupled resonators.

In the theoretical analysis, sense resonators motion against shock is derived and in the numerical analysis, the motion equations are modelled using Matlab/Simulink for three decoupling ratio designs; 0.09, 0.13 and 0.29. The theoretical analysis showed that acceleration sensitivity is proportional to stiffness unbalance, inverse to decoupling ratio and cubic of anti-phase frequency, and the angular rate sensitivity is inverse to the anti-phase frequency. In the numerical analysis of stiffness unbalanced TFGs, a sensing resonator displacement against shock signal showed a peak amplitude at sense anti-phase frequency in Fourier spectrum and a large decoupling ratio design, 0.29 has smaller acceleration output than *DR* design of 0.09.

We designed in-plane coupled resonators, which represents the sense resonators of z-axis TFG, to avoid the hindrances caused by fully functional TFG on the measurements. Each coupled resonator consists of two unit resonators and they are coupled with two types of coupling schemes; one is with frame and the other is with spring. Three decoupling ratio values of 0.09, 0.13 and 029 were set similar to numerical analysis and they were fabricated on SOI wafer. The anti-phase frequency is fixed at 16.5 kHz. The resonators were packaged at 100 Pa. The finite element analysis (FEA) is carried out on symmetric resonator and stiffness unbalanced resonators. The frequency sweep simulations showed

that in symmetric resonators, there is no anti-phase motion whereas in unbalanced resonators, resonators vibrated in anti-phase motion at anti-phase frequency. In the measurements, an acceleration amplitude of 1-g (9.8 m/sec^2) with frequency sweep signal is applied. The frequency response showed that resonators vibrated in anti-phase motion, since the resonators were unbalanced after fabrication. There were discrepancies in the measured frequencies and decoupling ratio. The measured results were normalized with theoretically derived equation for better comparison. The normalized results did not show any difference on anti-phase amplitudes in two types of coupling. The large decoupling ratio designs had smaller anti-phase vibration output.

We designed out-of-plane coupled resonators, which represents the sense resonators of x-axis TFG. In addition to two types of coupling methods, two types of motions; translational and torsional, were selected. The *DR*s and frequencies were set same as in-plane resonators and fabricated on SOI wafer. To apply the in-phase oscillation on coupled resonators, the coupled resonators were excited using piezo-actuator and observed using laser Doppler vibrometer. The measured frequency response showed that resonators are excited in anti-phase mode against in-phase oscillation. The measured results were normalized same as in-plane results. The normalized results did not show any difference on anti-phase amplitudes in two types of coupling and two types of motion. The larger *DR* designs showed smaller anti-phase amplitudes. From the measurements of in-plane and out-of-plane coupled resonators, we compared the resonators for selection of best resonator. Our comparison against *DR* deviation, stiffness unbalance revealed that spring-coupled (translational) designs are best choice as sense resonators used in TFG. Therefore, anti-shock TFGs can be designed by setting the large decoupling ratio in sense resonator and selecting the spring-coupling method.

Chapter 1
Introduction

A gyroscope is a sensor that measures the angle or angular velocity [1]. Based on the various physical principles, gyroscopes are categorized as mechanical gyroscopes, optical gyroscopes, nuclear magnetic resonance (NMR) gyroscopes, and vibratory gyroscopes [2] [3]. In 1852, French scientist Foucault devised a gimbaled wheel gyroscope to measure the earth rotation. A gimbaled gyroscope is an example of mechanical gyroscopes which operates on the principle of conservation of angular momentum [4]. Foucault joined the Greek words "skopein" meaning to see and "gyros" meaning rotation and coined the word *Gyroscope* for his suspended wheel. Mechanical gyroscopes measure the angle of rotation. A gimbaled gyroscope comprised of a spinning wheel mounted on two gimbals (for two-axis input). The rotating parts introduce bearing friction and wear that affects long term performance. To minimize these effects, high-precision bearings and special lubricants are very much needed that increases cost and maintenance. Therefore, bulky gimbaled gyroscope is not suitable in the view point of cost and size. The optical gyroscopes operate on the principle of Sagnac effect (Georges Sagnac reported in 1913-1914), which induces a path difference between two oppositely traveling beams against the rotation [5]. Fiber optic gyroscope (FOG) [6-8] and ring laser gyroscope (RLG) [9] [10] are categorized as optical gyroscopes. FOG and ROG are used in many high performance applications. NMR gyroscopes are currently in development. The operation principle is based on the change in the precession frequency of noble-gas molecules' magnetic movement (the Larmor frequency) due to rotation [11] [12]. Vibratory gyroscopes measure the Coriolis force, which was discovered by and named after the French scientist Gaspard Gustave Coriolis in 1835. The operation principle lies on transfer of energy between two vibratory modes due to Coriolis effect. The hemispherical resonator gyroscope (HRG) is an example of vibratory gyroscope [13]. It is noted that HRG measures angle of rotation. Among all high performance gyroscopes, the HRG achieved best angle random walk (ARW) and bias stability [14]. In general, gyroscopes can be classified into three different categories based on their performance range: inertial-grade, tactical-grade, and rate-grade devices. The required performance specification for each aforesaid class of gyroscopes is given in Table 1.1 [15].

Table 1.1 Performance requirements for different classes of gyroscopes [15].

Parameter	Rate Grade	Tactical Grade	Inertial Grade
Angle Random Walk ($^o/\sqrt{hr}$)	> 0.5	0.05-0.5	<0.001
Bias Drift (^{o}/hr)	10-1000	0.1-10	<0.01
Scale factor accuracy (%)	0.1-1	0.01-0.1	<0.001
Full scale range (^{o}/sec)	50-1000	> 500	>400
Max. Shock in 1msec, g's	10^3	10^3-10^4	10^3
Bandwidth (Hz)	> 70	~ 100	~ 100

The HRG, FOG and RLG performance parameters are in the range of inertial grade applications. In the high-performance applications, cost and size are not a concern. But, in the rate grade applications such as automotive and consumer applications, they are important parameters. The high-performance RLG and FOG cannot be developed in miniature size, since the accuracy of Sagnac effect gyroscopes depends on the length of the optical path that increases the design area [3].

Vibratory gyroscopes are easy to implement in several millimetre sizes and possible to integrate with the integrate circuit (IC) on the same substrate using micromachining technology. By using this technology, it is possible to realize functional blocks such as masses, flexures, actuators, detectors and levers that can be combined to build a complete system on a chip. The micromachined functional blocks is realized by adapting the standard IC fabrication process such as photolithography based pattern transfer methods and successive patterning of thin/thick structural layers and with the arrival of dry etching methods. The miniaturization of the systems and batch processing method realize the reduction in device size, weight, cost and power consumption.

Due to these advantages, micro-machined (MEMS) vibratory gyroscopes found multitude of applications. Initially, MEMS Coriolis vibratory gyroscopes are developed for automotive applications [19-23]. The continuous improvements in performance parameters are expanding the application spectrum from automotive to aerospace and consumer applications. The automotive sector has multiple applications namely anti-skid, roll-over detection and next generation airbag and anti-lock brake systems (ABS) [24]. The improvements in designs for shock survivability and reliability found many applications in consumer market [27]. The consumer applications include image stabilization in digital cameras, smart user-interfaces in handhelds, gaming, and inertial pointing devices.

1.1 Coriolis vibratory gyroscopes

Vibratory gyroscopes operation is based on the transfer of energy between two vibration modes (drive mode and sense mode) due to Coriolis effect. The Coriolis force (F_c) induced on a vibrating mass is

$$\vec{F}_c = 2m\left(\vec{v} \times \vec{\Omega}\right) \qquad \text{---- 1.1}$$

where v is velocity of vibrating mass or resonator (m) and Ω is applied angular velocity. The induced force (F_c) is proportional to the rotation input. The resonator is continuously oscillated using driving actuation mechanism and the induced Coriolis force is sensed using sensing mechanism.

The driving actuation mechanism can be implemented with piezo electric, electro magnetic or electro static, whereas the sensing mechanism can be implemented with capacitive [28-30], piezo electric [31] [32], piezo resistive [33-36], tunneling [37] and electro magnetic [38]. So far, most of the fabricated gyroscopes are electro static actuation and sensing type, since it is easy to fabricate electrodes on the silicon wafer and capacitance is insensitive to temperature. Comb-type electrodes are generally used for implementing driving scheme and parallel plate electrodes are used for sensing scheme.

A typical z-axis MEMS vibratory gyroscope is implemented as shown in Fig. 1.1. A resonator is suspended by four crab-leg suspension springs and has four anchor points. The resonator is used for both driving and sensing. It has two-degree of freedom (2-DOF) along x- and y-axes i.e. it has two resonance frequencies (modes). The resonance frequency along drive-axis (x-axis) is called as drive-mode frequency and along sense-axis (y-axis) is called as sense-mode frequency. The resonator has drive electrodes and sense electrodes. The drive electrodes are connected to opposite phase voltages to apply linear continuous oscillation force and sense electrodes are arranged in differential manner i.e. for the same displacement, a set of electrodes has increasing capacitance and the remaining set has decreasing capacitance. Here, in this gyroscope, capacitance change on two sides of the resonator is opposite. Differential capacitance sensing is generally used to linearize the capacitance change with the displacement. The input of differential amplifier comes from the sense electrodes via trans-impedance amplifiers. The demodulation system recovers only the signal whose frequency is at resonator oscillation frequency (driving frequency).

As a gyroscope, the resonator is continuously oscillated at a frequency, f_d (driving or operation frequency) along the x-axis (drive-axis) to keep the linear momentum. On

rotating the gyroscope around the *z*-axis (input-axis), Coriolis force is induced on the oscillating resonator along *y*-axis (sense-axis) at the driving frequency, f_d. The force (F_c) induced displacement results into differential capacitance change. The trans-impedance amplifiers coverts change in impedance to voltage signal and differential amplifier adds the differential voltage signals. Finally, the demodulation system produces the gyroscope output signal at the f_d. In the vibratory gyroscopes, the operation frequency is generally set at the drive-mode frequency to increase the drive velocity, and drive-mode frequency is designed near the sense-mode frequency to amplify the Coriolis response with Q-factor. The vibratory gyroscopes are classified into two types based on the occurrence of drive and sense modes and their mode-shapes; degenerate-mode and non-degenerate-mode gyroscopes as shown in Fig. 1.2.

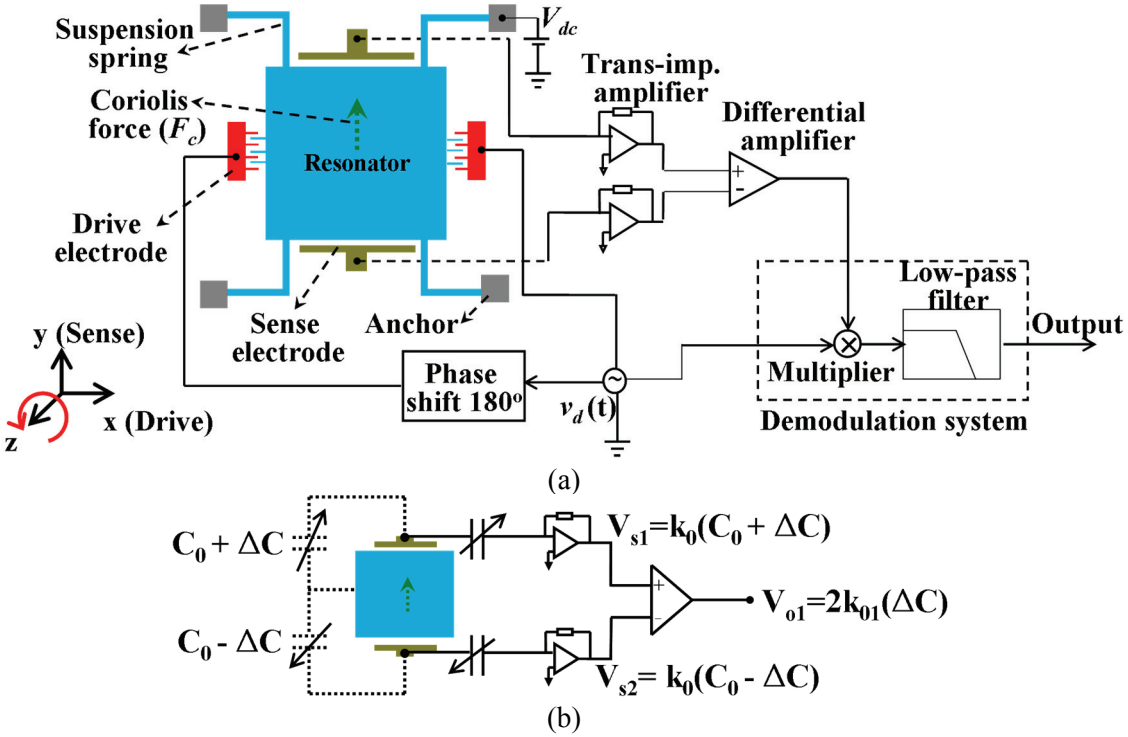

Figure 1.1 (a) Schematic diagram of single resonator vibratory gyroscope (b) the addition of differential capacitance change by differential amplifier in sensing circuit.

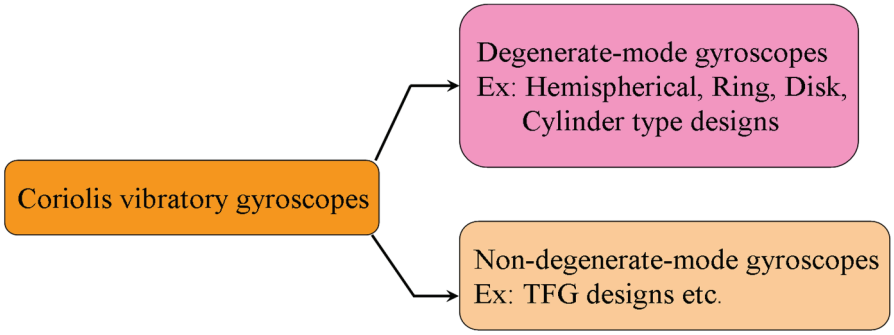

Figure 1.2 Classification of MEMS vibratory gyroscopes.

1.1.1 Degenerate mode gyroscopes

In degenerate-mode gyroscopes, the drive and sense modal frequencies and their mode-shapes are indistinguishable since the mass and stiffnesses are symmetric along both the drive- and sense-axes. This allows measuring the angle of rotation directly. The degenerate-mode gyroscopes can be designed with continuous mass such as hemispherical [13], ring [39-48], star [49-50], disk [51-58] and cylinder types [59-62] as shown in Fig. 1.3. The degenerate-modes appear as primary elliptical mode (n=2), or secondary elliptical mode (n=3) based on the crystallographic orientation.

The operation principle of ring type degenerate-mode gyroscope is shown in Fig. 1.4. The ring forms the nodes and anti-nodes. During the drive mode, opposite nodes either contract or expand and anti-nodes do not vibrate. If the gyroscope is rotated around the *z*-axis (yaw-axis), the Coriolis force is induced along the sense-axis which is 45° apart from the drive-axis. The ring, star and cylinder type gyroscopes are designed with several thousands of kHz. The disk shape gyroscopes are having higher frequency due to bulk acoustic modes and operate as Bulk Acoustic Wave (BAW) gyroscopes.

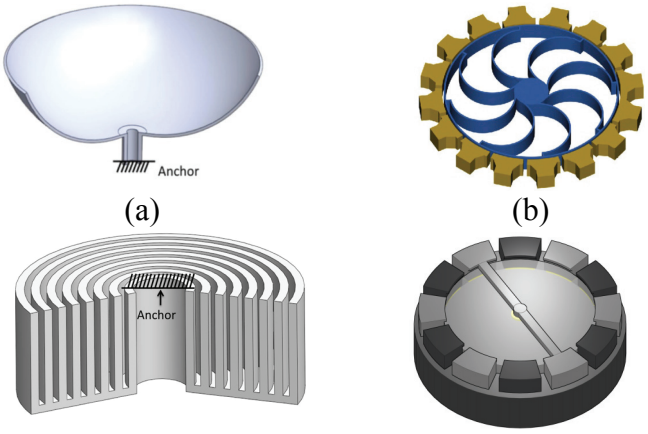

Figure 1.3 Schematic diagrams of degenerate mode gyroscopes (a) hemispherical (b) ring (c) cylinder (d) disk types.

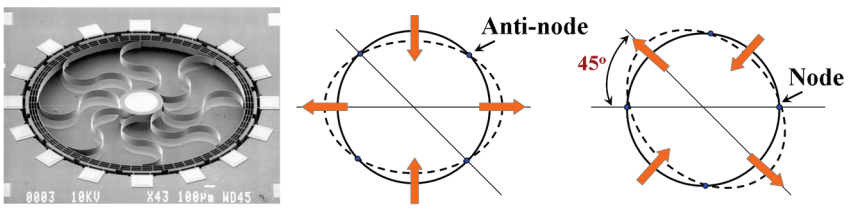

Figure 1.4 (a) SEM image of ring type gyroscope [41] (b) drive mode (c) sense mode.

1.1.2 Non-degenerate mode gyroscopes

In non-degenerate-mode gyroscopes, the drive and sense modal frequencies and their shapes are distinguishable, since the mass and stiffnesses are not symmetric along the drive- and sense-axes. Twin-mass tuning fork gyroscope (TFG) or Quad-mass TFG are examples of non-degenerate-mode gyroscopes [29] [31] [66-74]. Twin-mass TFG wherein two resonators are used for sensing, is formed by coupling two single resonator gyroscopes or decoupled gyroscopes. Quad-mass TFG wherein four resonators are used for sensing are formed by coupling two twin-mass TFGs. A z-axis TFG [72] and x-axis TFG [68] are shown in Figs 1.5 and 1.6. In these designs, each resonator acts as both drive and sense resonator. During operation as a gyroscope, two drive resonators are continuously oscillated in anti-phase direction (180^o phase difference between two resonators) as shown in Figs 1.5(b) and 1.6(b). On rotating the gyroscopes around input axis, Coriolis force is induced on the sense resonators in anti-phase direction as shown in Figs 1.5(c) and 1.6(c). The differential capacitance changes of sensing electrodes are added by a differential amplifier and produces gyro output at driving frequency. The main advantage of TFG operation is to reject external acceleration (caused by shocks) by differential amplifier as common mode signal i.e. two sense resonators move with same displacement and phase (0^o phase difference). Therefore, ideal TFGs are indeed having zero acceleration sensitivity. The twin-mass TFGs are simple and consume less area of silicon compare to quad-mass TFGs.

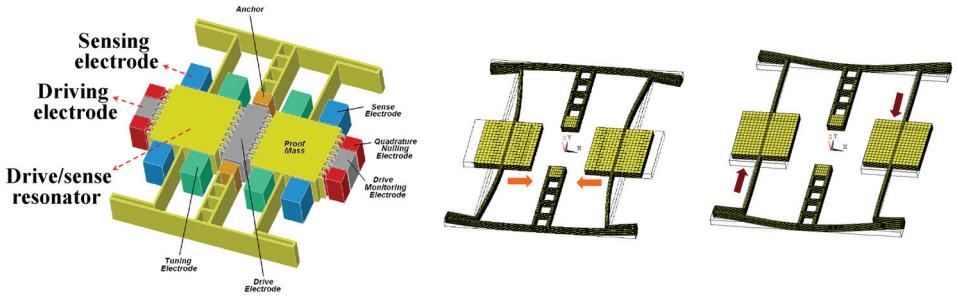

(a) (b) (c)

Figure 1.5 (a) Schematic diagram of a z-axis TFG (b) drive mode (c) sense mode.

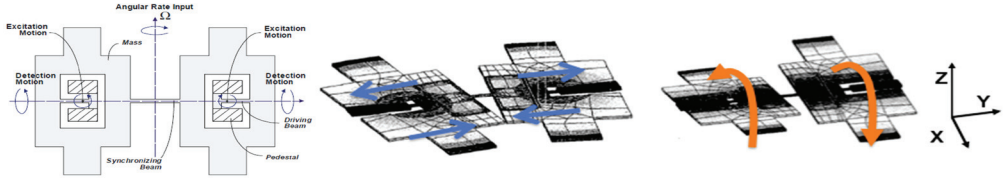

(a) (b) (c)

Figure 1.6 (a) Schematic diagram of a x-axis TFG (b) drive anti-phase mode (c) sense anti-phase mode.

1.2 Research motivation

In automobiles, the harsh environmental conditions such as wide temperature range, high humidity, and severe vibrations demand high reliability for long operation time. For MEMS vibratory gyroscopes, one of the major issues for reliable operation is the acceleration sensitivity (acceleration output) that is false or error output generated by mechanical vibrations (accelerations). In automobile, since many sources of shocks and vibrations are existing and inevitable, vibratory gyroscopes that detect a rotation by inertia force, are always susceptible to acceleration. For example, in the single resonator gyroscope shown in Fig. 1.1, the sensing resonator looks similar to an accelerometer structure and displaces along the sense-axis by linear acceleration. If the acceleration contains a signal around the operation frequency, the signal will be appeared as rotation output since it cannot be distinguished from the Coriolis force. For these kinds of applications, symmetric TFGs are best suitable to eliminate the acceleration output due to the differential operation (anti-phase driving) and common-mode rejection.

However, there are no ideal or perfectly symmetric TFGs. Previously reported TFGs [98] showed the acceleration sensitivity. The gyroscope reported by Mochida et al. had an acceleration output of ~5 deg/s/g (6% of full scale) when it was oscillated along the sensing axis at the driving frequency as shown in Fig. 1.7. In these reports, although the source of the output was attributed to the asymmetry in which there would be unbalance in mass and/or stiffness of supporting beam caused by fabrication error, the detailed mechanism on source of acceleration sensitivity and reduction method have not been reported. Yoon et al. in ref. [97] proposed and analyzed the three sources of acceleration output in three types of ideal TFGs. The most significant error source was the

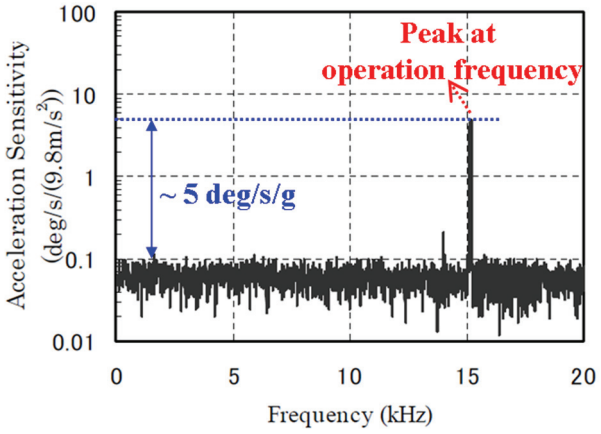

Figure 1.7 A 1-g (9.8 m/sec^2) acceleration with frequency sweep is applied along the sensing axis that resulted in a peak signal at driving frequency. This gyroscope shows ~ 5 deg/s/g (nearly 6% of full scale output) [98].

non-linearity at sense electrodes due to large displacements and simultaneous application of rotation input. However, none of three sources explains the measured acceleration output since their analysis did not consider the structural asymmetry, which is unavoidable in microfabricated structures and most likely situation of sudden shocks only (not including rotation input). So far there is no clear understanding on the mechanism of source of acceleration output. There exists various kinds of TFGs and they seem to have different acceleration sensitivities.

There are two traditional ways to suppress the acceleration output; designing the TFG on mechanical low-pass filter [76] and rubber damping. As we know that if a shock signal whose frequency spectrum is lower than gyroscope operation frequency is applied, then the capacitance change signals are filtered by demodulation system, since the demodulation system recovers the signal whose frequency is at operation frequency. If a shock consists of wide frequency spectrum whose frequency is around the gyro operation frequency, then demodulation circuit cannot reject. By designing a gyroscope on isolation stage which consists of a mechanical low pass filter whose frequency is smaller than gyroscope operation frequency, the isolation stage passes only low frequency signals to the gyroscope. Isolation stage can be designed with a glass wafer on which gyroscope is bonded [76]. The major disadvantage of this approach is that it also increases the complexity of the total system. On the other hand, by placing a rubber damping, it suppresses the vibration energy applied on gyro. But, it increases the size of the total system which is not a viable solution.

1.3 Research objectives and methods

The objective of this research is to find the source of acceleration sensitivity in the sense resonators of tuning fork gyroscopes (TFGs) and develop novel design techniques for suppressing the acceleration sensitivity that will lead to develop anti-shock TFGs.

1. The source of acceleration sensitivity in a fabricated TFG is identified as the excitation of anti-phase mode against a shock signal due to stiffness unbalance. The anti-phase motion appears on the gyro output as acceleration output.
2. To suppress the acceleration sensitivity, we proposed a method to decrease the vibration coupling between two sense-axis modes i.e. sense in-phase and anti-phase modes that results into smaller anti-phase vibration amplitude against the acceleration input. The method is termed as frequency decoupling method, which is “sense in-phase mode should be separated as far as possible from the sense anti-phase mode”. By keeping the anti-phase frequency constant and vary the in-phase frequency in the frequency decoupling method, the angular rate sensitivity does not change.
3. At first, the source of acceleration sensitivity of a TFG is analyzed through theoretical and numerical analysis. In the theoretical analysis, we derived a relationship between the acceleration sensitivity and frequency decoupling value. The numerical analysis was carried out on unbalanced TFGs.
4. To verify the frequency decoupling method through FEA and experiments, in-plane coupled resonators are designed with two types of coupling schemes; frame and spring. Two types of coupling methods chosen to also evaluate the effect of coupling scheme on the vibration sensitivity. To verify the versatility of applying the frequency decoupling method in x-axis TFGs, we also designed four out-of-plane coupled resonators, two of them are frame-coupled and the other two are spring-coupled. Each coupled-resonator adopted either translational or torsional motion to verify the effect of coupling method and motion types on acceleration sensitivity. From the measurements of in-plane and out-of-plane coupled resonators, we will provide which design is best choice for selecting as sense resonators to design anti-shock TFGs.

1.4 Outline of dissertation

In Chapter 2, the details of technical background on the Coriolis vibratory gyroscopes and proposed method to suppress the acceleration sensitivity are described. In Chapter 3, theoretical and numerical analysis of acceleration sensitivity and its suppression method of a TFG is reported. In Chapter 4, design of in-plane coupled resonators to verify the source of acceleration sensitivity and frequency decoupling method through FEA simulations and experiments are reported. The measurement setup for applying in-phase mechanical oscillations and measurement results are discussed. In chapter 5, we designed four types of out-of-plane coupled resonators using SOG and SOI process. The measurement setup for measuring the frequency response by applying continuous oscillations vertically to the resonators is explained. The measurement results of in-plane and out-of-plane coupled resonators are compared to select the best choice of resonator used in TFG. Finally, in Chapter 6, Conclusions and future works are reported.

Chapter 2
Technical background

2.1 The equations of motion of vibratory gyroscopes

The motion of a vibrating body in a rotating frame can be explained from the stationary inertial frame by adding an additional fictious force in motion equation. The fictious force named as Coriolis force after Gustave Gaspard de Coriolis, a French scientist who mathematically derived it in 1835.

The acceleration experienced by a moving body in a rotating reference frame can be derived as follows. In the Fig. 2.1, *XYZ* is a non-inertial reference system which does not accelerate or rotate and *xyz* system translates and rotates with respective to *XYZ*. A point 'p' in the *xyz* system is vibrating with velocity $\vec{v}_r$. Suppose that $\vec{r}_i$ and $\vec{R}$ are position vectors of 'p' and O' with respect to O in the *XYZ* system. Then,

$$\vec{r}_i = \vec{R} + \vec{r} \qquad \text{---- 2.1}$$

where $\vec{r}$ is the position vector of 'p' with respect to point O'. If the *xyz* is rotated, the velocity of point 'p', $\vec{v}_i$ as viewed from the inertial frame is related to the velocity of point p with respect to O', $\vec{v}_r$ by

$$\vec{v}_i = \dot{\vec{R}} + \vec{v}_r + (\vec{\Omega} \times \vec{r}) \qquad \text{---- 2.2}$$

where $\vec{\Omega}$ $(=\dot{\theta})$ is the rotation rate of the *xyz* system. The acceleration of point 'p' with respect to inertial frame is given by

$$\vec{a}_i = \ddot{\vec{R}} + \dot{\vec{v}}_r + (\dot{\vec{\Omega}} \times \vec{r}) + (\vec{\Omega} \times (\vec{\Omega} \times \vec{r})) + 2(\vec{\Omega} \times \vec{v}_r) \qquad \text{---- 2.3}$$

where $\dot{\vec{\Omega}}$ $(=\ddot{\theta})$ is the angular acceleration of the *xyz* system. The term $\dot{\vec{v}}_r$ or $\vec{a}_r$ is

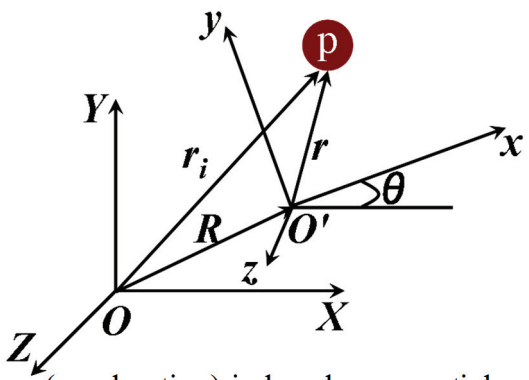

Figure 2.1 Coriolis force (acceleration) induced on a particle, which is vibrating in the *xyz* system, by applying the rotation around one of the axis with respect to fixed frame *XYZ* system.

the acceleration of point 'p' with respect to O'. The term $\ddot{\vec{R}}$ is the absolute acceleration of point O'. The term $\dot{\vec{\Omega}}\times\vec{r}$ is similar to tangential acceleration and $\vec{\Omega}\times(\vec{\Omega}\times\vec{r})$ represents centripetal acceleration. The last term in the equation $2(\vec{\Omega}\times\vec{v}_r)$ represents Coriolis acceleration, which is perpendicular to the velocity (of vibrating direction) and rotation input directions. The equations of motion are applied to two degree-of-freedom (2-DOF) mass 'm' as shown in Fig. 2.2. To operate as a gyroscope, mass is continuously oscillated with a displacement '*x*' along the drive-axis (x-axis) with an angular frequency ω_d (driving or operation frequency). By rotating the *xyz* system around z-axis, '$\vec{\Omega}_z$', the Coriolis force is induced on the mass along the sense-axis (*y*-axis) at the operation frequency.

$$m\ddot{x}+c_x\dot{x}+(k_x-m(\vec{\Omega}_y^2+\vec{\Omega}_z^2))x+m(\vec{\Omega}_x\vec{\Omega}_y-\dot{\vec{\Omega}}_z)y=F_d+2m(\vec{\Omega}_z\times\dot{y}) \qquad \text{---- 2.4}$$

$$m\ddot{y}+c_y\dot{y}+(k_y-m(\vec{\Omega}_x^2+\vec{\Omega}_z^2))y+m(\vec{\Omega}_x\vec{\Omega}_y+\dot{\vec{\Omega}}_z)x=-2m(\vec{\Omega}_z\times\dot{x}) \qquad \text{---- 2.5}$$

where F_d is the driving force (= $F_0\sin(\omega_d t)$) for keeping linear momentum. For a constant angular rate input $\dot{\vec{\Omega}}_z=0$ and for angular rates much smaller than the driving frequency of the gyroscopes, the terms $\vec{\Omega}_x^2$, $\vec{\Omega}_y^2$ and $\vec{\Omega}_x\vec{\Omega}_y$ can be neglected. The simplified 2-DOF equations of motion becomes;

$$m\ddot{x}+c_x\dot{x}+k_xx=F_d+2m(\vec{\Omega}_z\times\dot{y}) \qquad \text{---- 2.6}$$

$$m\ddot{y}+c_y\dot{y}+k_yy=-2m(\vec{\Omega}_z\times\dot{x}) \qquad \text{---- 2.7}$$

The two final terms, $2m(\vec{\Omega}_z\times\dot{y})$ and $2m(\vec{\Omega}_z\times\dot{x})$ in the equation are the rotation-induced Coriolis forces. Since the Coriolis force induced displacement along the sense-axis is in 'nm' range, the term $2m(\vec{\Omega}_z\times\dot{y})$ is negligible.

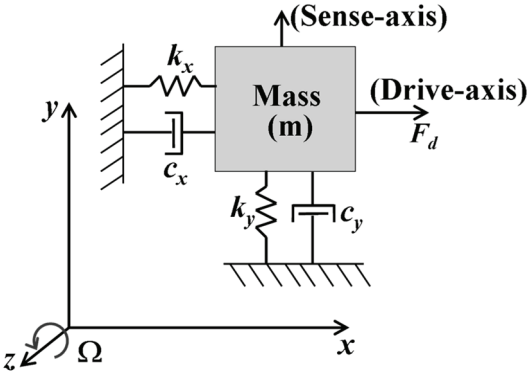

Figure 2.2 Operation principle of a lumped mass-spring-damper model as a gyroscope.

Finally, the equations of motion are;

$$m\ddot{x} + c_x\dot{x} + k_x x = F_d \qquad \text{---- 2.8}$$

$$m\ddot{y} + c_y\dot{y} + k_y y = -2m(\vec{\Omega}_z \times \dot{x}) \qquad \text{---- 2.9}$$

The Coriolis force applied on the mass along the sense-axis is

$$F_c = 2m(\vec{\Omega}_z \times \dot{x}) \qquad \text{---- 2.10}$$

The induced Coriolis force is proportional to velocity of the mass along the drive-axis and applied angular rate input. In capacitive gyroscopes, rate induced displacement along sense-axis results in to capacitance changes, which are added by a differential amplifier in Application-Specific-Integrated-Circuit (ASIC) and produces rate output after demodulation at operation frequency.

The displacement amplitude along sense-axis against Coriolis force can be increased by having the large displacement amplitude along the drive-axis or setting the operation frequency near the resonance frequency along sense-axis that will be discussed in next section.

2.2 Rate sensitivity of a gyroscope

The mass (or resonator) is having two resonance modes along drive-axis and sense-axis as shown in Fig. 2.3. The two resonance modes along drive-axis and sense-axis are named as drive-mode (ω_d) and sense-mode (ω_s), respectively.

By applying the Fourier transform to the equation of motion along drive-axis, which is Eq. 2.6, the drive displacement $x(s=j\omega)$ against the force F_D becomes;

$$\frac{x(j\omega)}{F_D(j\omega)} = \frac{1}{m\cdot\left[\left(\frac{k_x}{m} - \omega^2\right) + j\cdot\frac{\omega.c_x}{m}\right]} = \frac{1}{k_x\cdot\left[\left(1 - \left(\frac{\omega}{\omega_D}\right)^2\right) + j\cdot\frac{\omega}{Q_x.\omega_D}\right]} \qquad \text{---- 2.11}$$

The drive displacement is maximized at $\omega=\omega_d$. Then,

$$\left.\frac{x(j\omega)}{F_D(j\omega)}\right|_{\omega=\omega_d} = \frac{1}{j}\cdot\frac{Q_x}{k_x} \qquad \text{---- 2.12}$$

The drive displacement is amplified by the amount of Q-factor at resonance. The Q-factor is limited by air damping, thermo elastic damping, anchor loss and material damping. The

Q-factor is increased by operating in the vacuum. Therefore, large drive displacement amplitude can be achieved by vibrating the resonator at drive-mode resonance frequency. In general, gyroscope operation frequency is set at drive-mode frequency to utilize the amplification by Q-factor. Under rotation, the Coriolis force is induced along the sense-axis at drive-mode resonance frequency. The displacement response along the sense-axis can be maximized, if the ω_d is near the ω_s as shown in Fig. 2.3(b). The sense displacement at $\omega_d=\omega_s$ is derived as follows.

For drive-mode displacement of $x(t)$ and applied angular rate input Ω_z at ω_z angular frequency, the equation of motion along sense-axis becomes;

$$m\ddot{y}(t)+c_y\dot{y}(t)+k_y(t)=-2m\Omega_z\dot{x}(t)-m\dot{\Omega}_z x(t) \qquad \text{---- 2.13}$$

where $x(t)=x_D\cdot\cos(\omega_d t)$ and $\Omega_z(t)=\Omega_z\cdot\cos(\omega_z t)$

The Eq. 2.11 can be rewritten as

$$\Omega_z\cdot x_D\left[\left(\omega_d+\frac{\omega_z}{2}\right)\cdot\sin\left((\omega_d+\omega_z)t\right)+\left(\omega_d-\frac{\omega_z}{2}\right)\cdot\sin\left((\omega_d-\omega_z)t\right)\right]=\ddot{y}(t)+\frac{\omega_s}{Q_s}\cdot\dot{y}(t)+\omega_s^2\cdot y(t) \qquad \text{---- 2.14}$$

A Fourier transform is applied to the above equation to solve the sense displacement, which is decomposed in to two components as;

$$y(\omega_d+\omega_z)=\frac{\Omega_z\cdot x_D\left[\left(\omega_d+\frac{\omega_z}{2}\right)\cdot\sin((\omega_d+\omega_z)t)\right]}{\left[\omega_s^2-(\omega_d+\omega_z)^2\right]+j(\omega_d+\omega_z)\cdot\frac{\omega_s}{Q_s}} \qquad \text{---- 2.15}$$

$$y(\omega_d-\omega_z)=\frac{\Omega_z\cdot x_D\left[\left(\omega_d-\frac{\omega_z}{2}\right)\cdot\sin((\omega_d-\omega_z)t)\right]}{\left[\omega_s^2-(\omega_d-\omega_z)^2\right]+j(\omega_d-\omega_z)\cdot\frac{\omega_s}{Q_s}} \qquad \text{---- 2.16}$$

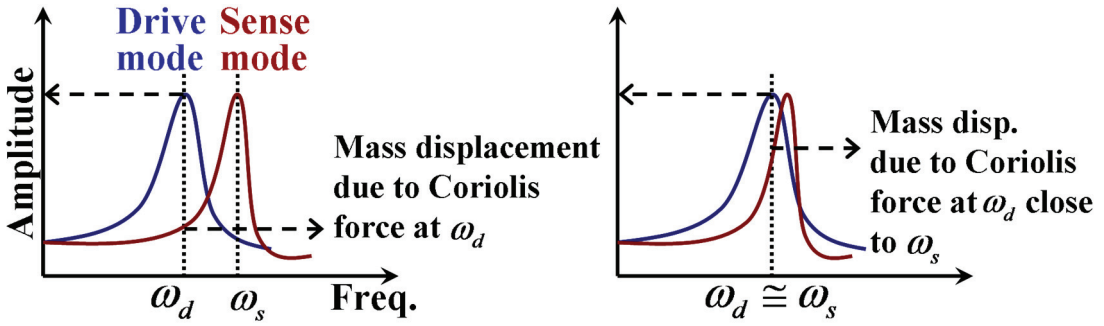

(a) (b)

Figure 2.3 Frequency responses along drive-axis and sense-axis (a) non-matched mode operation (b) matched-mode operation.

At $\omega_d=\omega_s$ (matched-mode operation) and assuming constant angular rate, $\omega_z=0$, the sense displacement becomes,

$$y(\omega_d = \omega_s) = \frac{2\Omega_z \cdot x \cdot Q_y}{j\omega_d} \qquad \text{---- 2.17}$$

By operating in matched-mode condition, the sense displacement amplitude is amplified by a Q-factor along sense-axis. Therefore, sensitivity of a gyroscope increases by placing the drive- and sense-modes close to each other. However, the matched-mode operation decreases the band-width of the gyroscope.

2.3 Performance parameters

The specifications and test procedures for rate gyroscopes are outlined in *IEEE Standard Specification Format Guide and Test Procedure for Coriolis Vibratory Gyros* [81]. The following are the important specifications that are used to determine the performance of a vibratory gyroscope.

Resolution: is the minimum rotation rate that can be distinguished from the noise floor of the system. It is expressed in ^{o}/sec/$\sqrt{Hz}$. The overall resolution of a gyroscope, the total noise equivalent rotation (TNEΩ), is determined by two uncorrelated components: Mechanical noise equivalent rotation rate (MNEΩ) and Electronic noise equivalent rotation rate (ENEΩ) [86]. The total resolvable rotation rate is expressed as:

$$\Omega_{min}(\text{Total}) = \sqrt{\Omega_{min}(\text{Brownian})^2 + \Omega_{min}(\text{Electronic})^2} \qquad \text{---- 2.18}$$

Brownian motion of air molecules causes displacement of the structure that result into noise. The electronic noise floor is dependent upon the noise of the interface circuitry. The noise floor of a gyroscope is often expressed in terms of angle random walk (ARW), which is typically expressed in degrees per square root of hour (deg/$\sqrt{hr}$) [15]. The ARW is evaluated from the Allan variance curve, in which the zero-rate-output is sampled for a certain time period, as a '–(1/2)' slope point on the curve.

Bias stability: All of the rate sensors provide a non-zero output in the absence of a rotation input, called gyroscope rate bias or zero-rate output (ZRO). The stability of this bias in a particular time period is important for many applications, since the bias point is the only reference for the gyroscope's output signal. It is expressed in deg/sec or deg/hr. Bias stability is evaluated from the minimum point on the Allan variance curve. Bias usually drifts in time due to number of sources such as fabrication process variations, post-process variations, packaging and ambient temperature.

Measurement range: The maximum input rate over which the full performance will be provided. It is expressed in ± deg/sec for positive and negative angular rate inputs.

Scale-factor and Linearity error: The ratio of a change in the output to a change in the input intended to be measured. It is expressed in mV/°/sec. The scale-factor of the gyroscope is evaluated by the slope of the least-squares best-fit-straight-line drawn through the plot of the gyroscope output vs. applied input rate within the measurement range. Linearity error is the deviation of the output from a least-squares linear fit of the input-output data. It is expressed as a percentage of (%) full scale range.

Bandwidth: The range of frequency of the angular rate input that the gyroscope can detect. It can also be considered as the frequency of the input rate for which the gyroscope output drops to $1/\sqrt{2}$ of the specified scale-factor value. It is expressed in Hertz (Hz).

2.4 Acceleration sensitivity

The ratio of change in gyroscope output against the applied acceleration (1-g=9.8 m/s^2, gravitational acceleration) along the sense-axis is termed as acceleration sensitivity (acceleration output). It is generally expressed as deg/s/g. The reliability of vibratory gyroscopes operation in safety system applications depends on the robustness to external accelerations. Here, we discuss the acceleration sensitivity of various types of non-degenerate-mode vibratory gyroscopes.

2.4.1 Acceleration sensitivity of decoupled gyroscopes

Previously, we discussed the operation principle of single resonator vibratory gyroscope in the Chapter 1, section 1.1. That type of gyroscope is an example of coupled vibratory gyroscope wherein a resonator is used as both drive and sense resonator. The main disadvantage of those gyroscopes is that it results into Quadrature error. In the fabricated gyroscopes, the actual drive-axis is not perfectly aligned with the designed drive-axis. The mismatch causes that drive-mode oscillations are coupled along the sense-axis that increases zero-rate-output (ZRO) [70] [78]. There are mainly two reasons for quadrature error. The fabrication error results in capacitance mismatch at drive electrodes, which causes the net electrostatic force direction, deviated from the actual drive-axis. The other reason is that the non-uniformity in the cross section of the suspension beams which results into cross-axis stiffness from drive-axis to sense-axis. To suppress the quadrature error in a gyroscope, drive mode and sense modes have to be decoupled by designing the independent suspension springs for both driving and sensing [83-94]. These types of

gyroscopes are termed as decoupled gyroscopes. The operation of decoupled gyroscopes is described below.

Decoupled gyroscopes are designed with independent suspension beams with the two separate masses or resonators [83-94]; one resonator is used for driving, named as drive resonator, and the other resonator is used for sensing, named as sensing resonator. The z-axis decoupled gyroscope is shown in Fig. 2.4. The driving resonator is having 1-DOF (along y-axis only) and sensing resonator is having 2-DOF (along x- and y-axes). The drive resonator is continuously oscillated by drive electrodes at drive-mode frequency, ω_d along y-axis (drive-axis). The sense resonator, which is attached to drive resonator is also in continuous oscillation along with the drive resonator. The drive and sense modal frequencies are given as;

$$\omega_d = \frac{k_d}{(m_d + m_s)} \qquad \text{---- 2.19}$$

$$\omega_s = \frac{k_s}{m_s} \qquad \text{---- 2.20}$$

where m_d and m_s are drive and sense resonator masses, respectively. The k_d and k_s are drive and sense resonators suspension stiffnesses, respectively. Under rotation, Ω, around z-axis, Coriolis force is induced on both the drive and sense resonators. Since, the drive resonator is having only 1-DOF, it is rigid to move along the sense-axis. The Coriolis force is measured on the sense resonator. The Coriolis induced displacement at $\omega_d = \omega_s$ becomes;

$$x(\omega_d = \omega_s) = \frac{2\Omega \cdot y_d \cdot Q_s}{j\omega_s} \qquad \text{---- 2.21}$$

where y_d is drive displacement and Q_s is Q-factor along the sense-axis. The displacement of the sensing resonator results into differential capacitance change which is added by differential amplifier and finally the demodulation system produces rate output at operation frequency, ω_d.

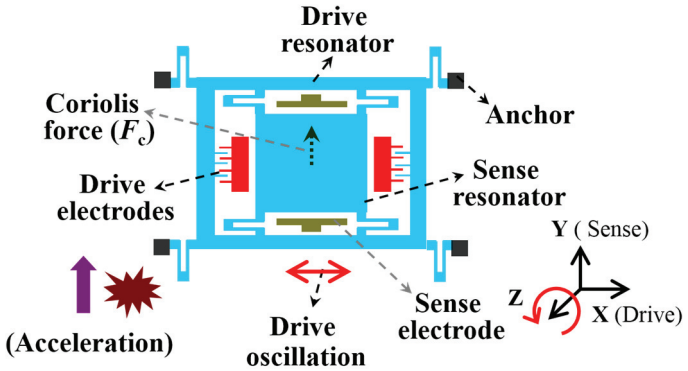

Figure 2.4 A z-axis decoupled gyroscope.

If an external acceleration which consists of wide frequency spectrum including the frequency at the operation frequency is applied along the sense-axis, the displacement of sense resonator at driving frequency cannot be distinguished from Coriolis induced displacement by demodulation system, since demodulation system recovers the signal, which is at the operation frequency. Therefore, the decoupled gyroscope indeed produces the acceleration output. To suppress the acceleration output, a common design technique is the use of tuning-fork architectures, which allows the sensor to reject common mode inputs while preserving the sensing signal.

2.4.2 Acceleration sensitivity of tuning fork gyroscope (TFG)

A decoupled TFG [71] [73] structure is shown in Fig. 2.5(a). Two individual gyro structures, shown in Fig. 2.4, are coupled with a spring and have at least four-degrees-of-freedom (4-DOF). The sense electrodes are connected in differential manner as shown in Fig. 2.5 (b). The left gyroscope's sense resonator electrode (1) and right gyroscope's sense resonator electrode (4) are connected to differential amplifier via trans-impedance amplifier and the remaining two electrodes (2) and (3) are connected together to another input terminal of differential amplifier via trans-impedance amplifier. During the Coriolis sensing, 1 and 4 electrodes set are having increasing capacitance and the remaining 2 and 3 electrodes set are having decreasing capacitance or vice versa.

The sense resonators moving along the sense axis (x-axis) show two resonance modes called as the sense in-phase (ω_{in}) and anti-phase (ω_{anti}) modes as shown in Fig. 2.6. At ω_{in}, the sense resonators move with the same phase, and at ω_{anti}, they move with a 180° phase difference between each other. Drive resonators moving along drive axis (y-axis) also show drive in-phase and anti-phase modes. The drive anti-phase frequency (ω_{d_anti}) is kept near the sense anti-phase frequency (ω_{anti}) to improve the rate resolution.

During operation, drive resonators are oscillated along the drive axis at the drive anti-phase frequency, ω_{d_anti}, (operation frequency) with a 180° phase difference to each other. When an angular rate input is applied around the z-axis, Coriolis force (F_c) is induced on the two sense resonators along the sense-axis in the opposite direction (same as sense anti-phase mode) as shown in Fig. 2.5(a). The resultant capacitance change of each resonator is added by differential amplifier as shown in Fig. 2.5(b). The summation of sense electrodes (1) and (4) is $2(C_0+\Delta C)$ and electrodes (2) and (3) is $2(C_0-\Delta C)$. Then the differential amplifier output becomes $4(\Delta C)$. The detailed explanation on how the capacitance change is affected for Coriolis sensing and acceleration is given below.

Coriolis Sensing:

By considering the initial gap of 'y_0', the static capacitance between resonator and fixed sense electrode becomes;

$$C_0 = \frac{\varepsilon_0 A_0}{y_0} \qquad \text{---- 2.22}$$

The capacitance of sense electrodes (1), (2), (3), (4) becomes;

$$C_1 = \frac{\varepsilon_0 A_0}{y_0 - y_1};\quad C_2 = \frac{\varepsilon_0 A_0}{y_0 + y_1};\quad C_3 = \frac{\varepsilon_0 A_0}{y_0 + y_1};\quad C_4 = \frac{\varepsilon_0 A_0}{y_0 - y_1} \qquad \text{---- 2.23}$$

where y_1 is the Coriolis induced displacement on sensing resonators. The capacitance change at sense electrode (1) is

$$\Delta C_1 = \frac{\varepsilon_0 A_0}{y_0} - \frac{\varepsilon_0 A_0}{y_0 - y_1}$$

$$= \frac{\varepsilon_0 A_0}{y_0^2 + y_0 y_1} y_1$$

$$= \frac{\varepsilon_0 A_0}{y_0^2} y_1 \quad \text{(assuming } y_1 << y_0\text{);} \qquad \text{---- 2.24}$$

The capacitance at sense electrodes (1), (2), (3), (4) can be written as;

$$C_1 = C_0 + \Delta C_1 \sin(\omega_d t);\quad C_2 = C_0 - \Delta C_1 \sin(\omega_d t);\quad C_3 = C_0 - \Delta C_1 \sin(\omega_d t);\quad C_4 = C_0 + \Delta C_1 \sin(\omega_d t);$$

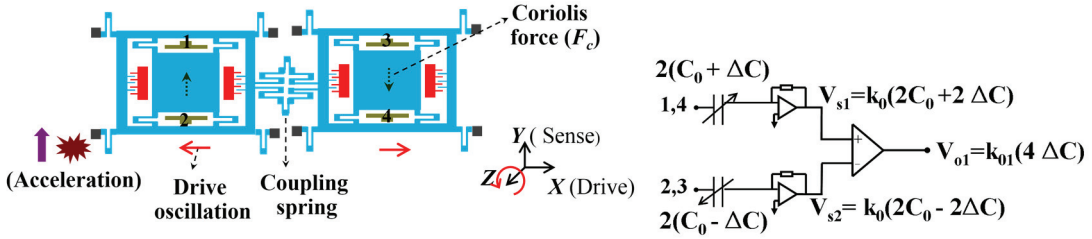

(a) (b)

Figure 2.5 Two individual decoupled gyroscopes are couple with a spring to form tuning-fork structure (a) operation principle of a TFG (b) sense electrodes configuration.

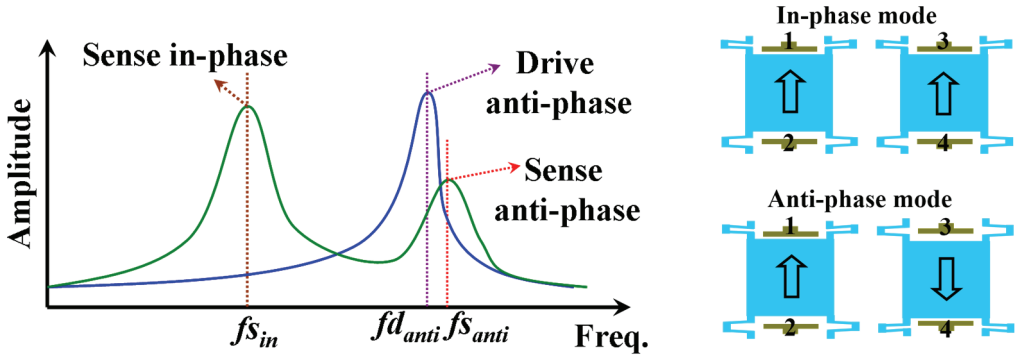

(a) (b)

Figure 2.6 (a) Frequency response of drive and sense resonators along drive- and sense-axis (b) sense resonators modes movement.

The total capacitance at the input terminal of trans-impedance amplifier becomes;

$C_1 + C_4 = 2(C_0 + \Delta C_1 \sin(\omega_d \, t))$; $C_2 + C_3 = 2(C_0 - \Delta C_1 \sin(\omega_d \, t))$;

The output of trans-impedance amplifier 1 and 2 becomes;

$V_{s1}=k_0(2C_0+\Delta C_1)$; $V_{s2}=k_0(2C_0-\Delta C_1)$;

where k_0 is the gain of the amplifier. The differential amplifier output becomes

$V_{o1}=k_{01}(4\Delta C_1)$;

where k_{o1} is the gain of the differential amplifier.

For an applied acceleration along the sense-axis, in an ideal perfectly symmetric TFG, two sense resonators move with the same displacement and phase (as in-phase mode), and the capacitance change from acceleration is cancelled as a common mode signal by the differential amplifier. It means the summation of sense electrodes (1) and (4) capacitance change becomes $2C_0$ and similarly with the rest of the sense electrodes (2) and (3) also. The both input terminals of differential amplifier has same signal (common-mode signal), then net output (V_{o1}) of the differential amplifier is zero. The explanation on how the capacitances varies against acceleration in Ideal TFG are given below.

Ideal TFG:

The capacitance of sense electrodes (1), (2), (3), (4) becomes;

$$C_1 = \frac{\varepsilon_0 A_0}{y_0 - y_2}; \quad C_2 = \frac{\varepsilon_0 A_0}{y_0 + y_2}; \quad C_3 = \frac{\varepsilon_0 A_0}{y_0 - y_2}; \quad C_4 = \frac{\varepsilon_0 A_0}{y_0 + y_2}; \qquad \text{---- 2.25}$$

where y_2 is the shock displacement of sensing resonators. The capacitance change at sense electrode (1) is

$$\Delta C_2 = \frac{\varepsilon_0 A_0}{y_0^2} y_2 \quad \text{(assuming } y_2 < y_0\text{);} \qquad \text{---- 2.26}$$

The capacitance at sense electrodes (1), (2), (3), (4) can be written as;

$C_1 = C_0 + \Delta C_2 \sin(\omega_d \, t)$; $C_2 = C_0 - \Delta C_2 \sin(\omega_d \, t)$; $C_3 = C_0 + \Delta C_2 \sin(\omega_d \, t)$; $C_4 = C_0 - \Delta C_2 \sin(\omega_d \, t)$;

The total capacitance at the input terminal of trans-impedance amplifier becomes;

$C_1 + C_4 = 2(C_0)$; $C_2 + C_3 = 2(C_0)$;

The output of trans-impedance amplifier 1 and 2 becomes;

$V_{s1}=k_0(2C_0)$; $V_{s2}=k_0(2C_0)$;

The differential amplifier output becomes $V_{o1}=0$;

However, the fabricated TFGs still produce an acceleration output. The causes for this have been attributed to fabrication errors resulting in mismatch in stiffness, which result into acceleration output. The explanation on how the capacitances change in the unbalanced sense resonators is given below.

Fabricated TFG:

In the fabricated TFG, assume the sensing resonators are unbalanced in mass or/and stiffness. This results into two different displacement amplitudes y_3 and y_4. The capacitance of sensing electrodes can be written as;

$$C_1 = \frac{\varepsilon_0 A_0}{y_0 - y_3};\quad C_2 = \frac{\varepsilon_0 A_0}{y_0 + y_3};\quad C_3 = \frac{\varepsilon_0 A_0}{y_0 - y_4};\quad C_4 = \frac{\varepsilon_0 A_0}{y_0 + y_4} \qquad \text{---- 2.27}$$

The capacitance change at sense electrode (1) is

$$\Delta C_3 = \frac{\varepsilon_0 A_0}{y_0^2} y_3 \quad \text{(assuming } y_3 < y_0\text{);} \qquad \text{---- 2.28}$$

$$\Delta C_4 = \frac{\varepsilon_0 A_0}{y_0^2} y_4 \quad \text{(assuming } y_4 < y_0\text{);} \qquad \text{---- 2.29}$$

The capacitance at sense electrodes (1), (2), (3), (4) can be written as;

$C_1 = C_0 + \Delta C_3 \sin(\omega_d t);\quad C_2 = C_0 - \Delta C_3 \sin(\omega_d t);\quad C_3 = C_0 + \Delta C_4 \sin(\omega_d t);\quad C_4 = C_0 - \Delta C_4 \sin(\omega_d t);$

The total capacitance at the input terminal of trans-impedance amplifier becomes;

$C_1+C_4=2C_0+\Delta C_3-\Delta C_4$; $C_2+C_3=2C_0-\Delta C_3+\Delta C_4$;

The differential amplifier output becomes $V_{o1}=k_{01}(2\Delta C_3-\Delta C_4)$. Although the mass and/or stiffness unbalance seems to result into acceleration output owing to different displacement amplitudes, there is no clear understanding on the mechanism of source of acceleration sensitivity and ways to suppress it.

2.5 Source of acceleration sensitivity in fabricated TFGs

In the coupled drive and sense resonator gyroscopes, which has only one mass or resonator for driving and sensing, the fabrication error causes unwanted vibrations in a resonator having two resonant modes reminds us of the quadrature vibration in gyroscopes. The quadrature vibration is a sensing mode vibration generated without any angular rate input that results into ZRO. Similar to the quadrature vibration, we thought that there is a vibration coupling from sense in-phase mode to sense anti-phase mode against applied in-phase acceleration along sense-axis. If an externally applied shock has wide frequency spectrum, which also include the operation frequency (in mode matched condition operation frequency is equal to sense anti-phase frequency), then, the sense resonators are vibrated in both in- and anti-phase modes as shown in Fig. 2.7. The sense resonators vibration in anti-phase mode against an applied acceleration cannot be distinguished from the Coriolis sensing motion. Therefore, the source of acceleration sensitivity arises from the excitation of sense anti-phase mode due to stiffness unbalance.

2.6 Proposed acceleration sensitivity suppression method (frequency decoupling)

The quadrature vibration can be suppressed by separating the drive and sense modes. Akin to the quadrature output, we thought that the acceleration output can be reduced by decoupling the in-phase and anti-phase mode of sense-axis modes, which is explained in Fig. 2.7. By separating the two modes far away (that is, large decoupling), the anti-phase vibration amplitude decreases as shown in Fig. 2.7 (b) compared to Fig. 2.7 (a). The frequency separation method is termed as “frequency decoupling method”, which is “sense in-phase mode should be separated as far as possible from the sense anti-phase mode”. The maximum separation is limited by unwanted modes appearing between the in- and anti-phase modes. In this method, the sense anti-phase frequency is kept constant and the in-phase is varied. The main advantage of the decoupling method is that it does not change the rate sensitivity of TFG, by keeping the sense anti-phase mode frequency constant and operating the TFG at sense anti-phase frequency. The other merit is a simple designing that results in no increase in the device space compared to traditional methods such as inserting mechanical low-pass filters and rubber damping.

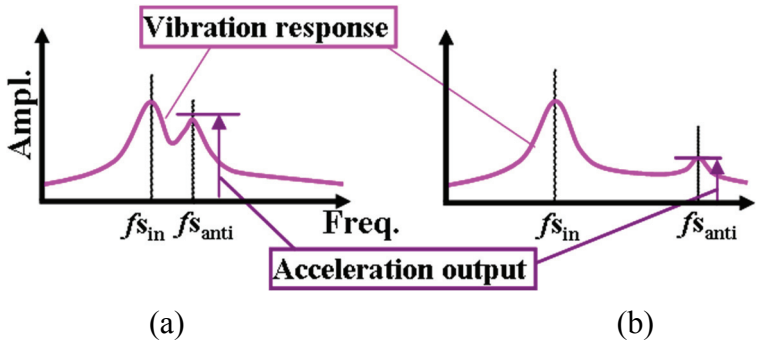

Figure 2.7 Decoupling of the two sense resonance frequencies (a) frequencies separated largely (b) frequencies separated closely.

Chapter 3
Theoretical and numerical analysis of acceleration sensitivity of TFG

3.1 Overview

In this chapter, the source of acceleration sensitivity and proposed frequency decoupling method was investigated through theoretical and numerical analysis on a spring-coupled translational x-axis TFG. In the theoretical analysis, the differential displacement of the two sense resonators is derived from its motion equations, since in the sensing circuit, the displacement is differentiated and demodulated at operation frequency and results into gyroscope output after low-pass-filter. The theoretical analysis is going to verify that large decoupling ratio design results into lower acceleration sensitivity and angular rate sensitivity does not change by using frequency decoupling method. In the numerical analysis the equations of sense resonators motion and sensing circuit is modelled using Matlab/Simulink. The analysis starts with input acceleration of a half sine shock. The amplitude and duration of the shock signal are 100 g (= 980 m/s^2) and 3 ms, respectively. A Fourier analysis is carried out on the sense resonator displacement signal. To verify the frequency decoupling method, we considered TFG with three DR designs of 0.09, 0.13 and 0.29.

3.2 Theoretical analysis of acceleration sensitivity in TFG

The theoretical analysis is carried out on x-axis TFG as shown in Fig. 3.1. Two simple decoupled gyroscopes are coupled with a coupling spring. During the operation, two drive resonators are sinusoidally oscillated in anti-phase direction along the y-axis at a frequency usually termed as operation frequency, ω_d. By applying the rotation input around the x-axis, the Coriolis force at the operation frequency is induced on the two sense resonators in opposite direction along the z-axis (out-of-plane). In the sensing circuit, the differential capacitance change (i.e. increase in capacitance at one sense resonator and decrease in capacitance in the remaining electrode) at the sense electrodes is added by the differential amplifier and demodulated at the operation frequency and produces the rate output.

The x-axis TFG in Fig. 1 was analyzed as a lumped parameter model. For the inertia force $F_L(t)$ and $F_R(t)$ on the left and right sense resonators, respectively, the equations of motion

of them along the sense-axis (z-axis) are

$$m_{s,\mathrm{L}}\ddot{z}_{\mathrm{L}} + c_{s,\mathrm{L}}\dot{z}_{L} + (k_{s,\mathrm{L}} + k_{\mathrm{c}})z_{\mathrm{L}} - k_{\mathrm{c}}z_{R} = F_{\mathrm{L}}(t)$$
$$m_{s,\mathrm{R}}\ddot{z}_{R} + c_{s,\mathrm{R}}\dot{z}_{\mathrm{R}} + (k_{s,\mathrm{R}} + k_{\mathrm{c}})z_{\mathrm{R}} - k_{\mathrm{c}}z_{\mathrm{L}} = F_{\mathrm{R}}(t) \qquad \text{---- 3.1}$$

In the above equations m_s, c_s and k_s are the mass, damping and stiffness of the sense resonators, in which the suffix L and R represent left and right gyroscopes and 's' represent sense resonator. k_c is the coupling spring stiffness. From here onwards, the subscript 's' is omitted.

In the theoretical analysis, we have not considered the drive structures, since the effect of drive resonators motion on acceleration sensitivity is negligible as reported in ref. [97]. The vibrating system of the coupled sense resonators has two fundamental resonant modes, the in-phase and anti-phase frequencies. If the two sense resonators is designed as same and the actual stiffness have small difference ($(k_L\text{-}k_R) \ll 4k_c$), the resonant frequencies are written as,

$$\omega_{\mathrm{in}} = \sqrt{\frac{k_{\mathrm{L}} + k_{\mathrm{R}}}{2m}} \qquad \text{---- 3.2}$$
$$\omega_{\mathrm{anti}} = \sqrt{\frac{k_{\mathrm{L}} + k_{\mathrm{R}} + 4k_{\mathrm{c}}}{2m}} \qquad \text{---- 3.3}$$

In theoretical analysis, we assumed that the mass and damping are same in two resonators and only the stiffness is differed ($m_{\mathrm{L}}=m_{\mathrm{R}}\equiv m$ and $c_{\mathrm{L}}=c_{\mathrm{R}}\equiv c$). Eqs. 3.1 are written in Laplace domain as,

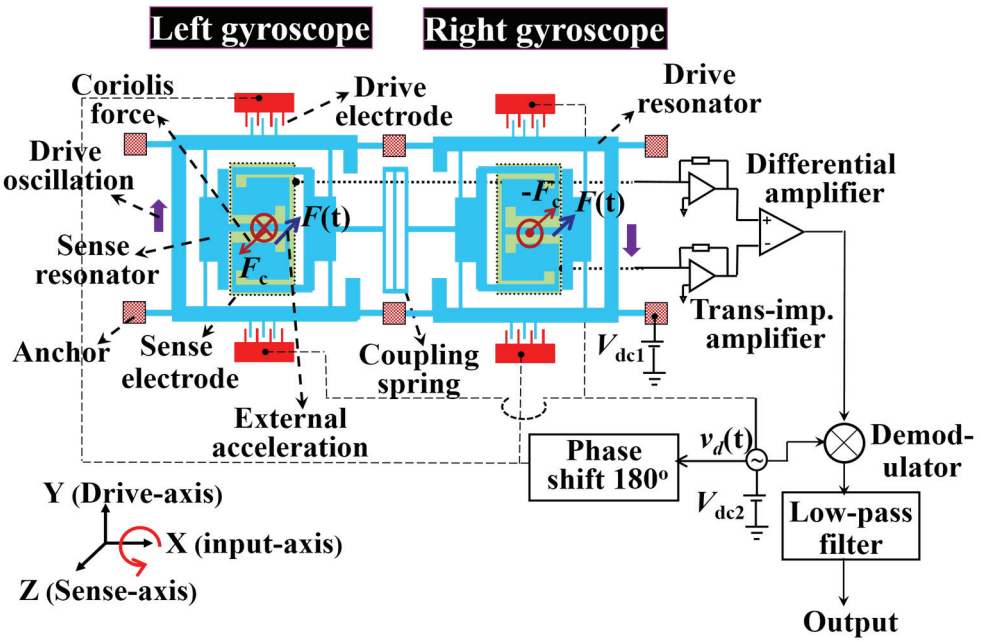

Figure 3.1 Modelled x-axis translational motion TFG.

$$(s^2m+sc+k_{\mathrm{L}}+k_{\mathrm{c}})z_{\mathrm{L}}(s)-k_{\mathrm{c}}z_{\mathrm{R}}(s)=F_{\mathrm{L}}(s) \qquad \text{---- 3.4}$$

$$(s^2m+sc+k_{\mathrm{R}}+k_{\mathrm{c}})z_{\mathrm{R}}(s)-k_{\mathrm{c}}z_{\mathrm{L}}(s)=F_{\mathrm{R}}(s) \qquad \text{---- 3.5}$$

The out-of-plane (z) displacement of each resonator is obtained from the equations. From the Eq. 3.5, $z_{\mathrm{R}}(s)$ can be written as,

$$z_{\mathrm{R}}(s)=\frac{k_{\mathrm{c}}z_{\mathrm{L}}(s)+F_{\mathrm{R}}(s)}{\left(s^2m+sc+k_{\mathrm{R}}+k_{\mathrm{c}}\right)} \qquad \text{---- 3.6}$$

The left resonator $z_{\mathrm{L}}(s)$ is described by substituting the Eq. 3.6 in the Eq. 3.4 as,

$$z_{\mathrm{L}}(s)=\frac{F_{\mathrm{L}}(s)\left(s^2m+sc+k_{\mathrm{R}}+k_{\mathrm{c}}\right)+k_{\mathrm{c}}F_{\mathrm{R}}(s)}{\left[\left(s^2m+sc+k_{\mathrm{L}}+k_{\mathrm{c}}\right)\left(s^2m+sc+k_{\mathrm{R}}+k_{\mathrm{c}}\right)-k_{\mathrm{c}}^2\right]} \qquad \text{---- 3.7}$$

Similarly $z_{\mathrm{R}}(s)$ can be written as,

$$z_{\mathrm{R}}(s)=\frac{F_{\mathrm{R}}(s)\left(s^2m+sc+k_{\mathrm{L}}+k_{\mathrm{c}}\right)+k_{\mathrm{c}}F_{\mathrm{L}}(s)}{\left[\left(s^2m+sc+k_{\mathrm{L}}+k_{\mathrm{c}}\right)\left(s^2m+sc+k_{\mathrm{R}}+k_{\mathrm{c}}\right)-k_{\mathrm{c}}^2\right]} \qquad \text{---- 3.8}$$

The output of a TFG can be discussed with the vibrating amplitude of the differential displacement between the two resonators (z_{L}-z_{R}) at the operating frequency (ω_{d}), since the output of differential amplifier is the difference between the capacitance changes of two displacements. The differential displacement z_{diff} against an acceleration $a(t)$ along the sense-axis is as follows by considering the identical inertia force $F(t) = ma(t)$ applied to each mass,

$$z_{\mathrm{diff}}(s)=\frac{F(s)\left(k_{\mathrm{L}}-k_{\mathrm{R}}\right)}{\left[\left(s^2m+sc+k_{\mathrm{L}}+k_{\mathrm{c}}\right)\left(s^2m+sc+k_{\mathrm{R}}+k_{\mathrm{c}}\right)-k_{\mathrm{c}}^2\right]} \qquad \text{---- 3.9}$$

The amplitude (magnitude) of the differential displacement at a frequency ω is,

$$\left|z_{\mathrm{diff}}\right|=\left|\frac{F\left(k_{\mathrm{L}}-k_{\mathrm{R}}\right)}{\left\{\omega^4m^2-\left(\frac{m\omega^2}{Q_s}\right)^2-\omega^2m\left(k_{\mathrm{L}}+k_{\mathrm{R}}+2k_{\mathrm{c}}\right)+\left(k_{\mathrm{L}}\times k_{\mathrm{R}}\right)+k_{\mathrm{c}}\left(k_{\mathrm{L}}+k_{\mathrm{R}}\right)\right\}+j\frac{m\omega^2}{Q_s}\left\{-2\omega^2m+k_{\mathrm{L}}+k_{\mathrm{R}}+2k_{\mathrm{c}}\right\}}\right|$$

---- 3.10

where $c=m\omega/Q_{\mathrm{s}}$ and Q_{s} is the quality factor along the sense-axis (constant). When a TFG is operated at the sense anti-phase mode ($\omega_{\mathrm{d}} = \omega_{\mathrm{anti}}$) and for the high quality factor ($1/Q_{\mathrm{s}} \ll 1$), the real part of the denominator in Eq. 3.10 is omitted. The vibrating amplitude at ω_{anti} is,

$$\left|z_{\text{diff}}\right| = \frac{F(k_{\text{L}} - k_{\text{R}})Q_s}{\omega_{\text{anti}}^2 m^2 \left\{-2\omega_{\text{anti}}^2 + \left(\frac{k_{\text{L}} + k_{\text{R}}}{2m}\right) + \left(\frac{k_{\text{L}} + k_{\text{R}} + 4k_{\text{c}}}{2m}\right)\right\}} \quad \text{---- 3.11}$$

By using Eqs. 3.2 and 3.3, Eq. 3.10 is written as,

$$\left|z_{\text{diff}}\right| = \frac{F(k_{\text{L}} - k_{\text{R}})Q_s}{\omega_{\text{anti}}^2 m^2 \left\{-2\omega_{\text{anti}}^2 + \omega_{\text{in}}^2 + \omega_{\text{anti}}^2\right\}}$$

$$= \frac{F(k_{\text{L}} - k_{\text{R}})Q_s}{\omega_{\text{anti}}^2 m^2 \left(\omega_{\text{in}} + \omega_{\text{anti}}\right)\left(\omega_{\text{in}} - \omega_{\text{anti}}\right)}$$

$$z_{\text{a,diff}} = \frac{F\left(\Delta k\right)Q_s}{\omega_{\text{anti}}^3 m^2 \left(\omega_{\text{in}} + \omega_{\text{anti}}\right)\left(DR\right)} \quad \text{---- 3.12}$$

where $\Delta k = k_{\text{L}} - k_{\text{R}}$ i.e. the stiffness difference between the left and right sense resonator and decoupling ratio, DR is defined as

$$DR = \frac{\left(\omega_{\text{anti}} - \omega_{\text{in}}\right)}{\omega_{\text{anti}}} \quad \text{---- 3.13}$$

A large *DR* value implies large separation between two-sensing resonant modes; in-phase (ω_{in}) and anti-phase (ω_{anti}). Eq. 3.12 indicates that the acceleration output is proportional to Δk and inverse of *DR* at the same operating frequency. The Eq. 3.12 proves that by keeping the anti-phase frequency constant and larger *DR* result into smaller acceleration output. The frequency decoupling method is verified through theoretical analysis.

To verify that angular rate sensitivity does not change by keeping the anti-phase frequency constant, The differential displacement against a constant angular rate Ω is obtained by considering the differential Coriolis force $F_{\text{L}}(t) = -F_{\text{R}}(t) = 2m\omega_{\text{d}}\Omega y_0 \sin(\omega_{\text{d}} t)$,

$$z_{\Omega,\text{diff}} = \frac{2F_{\text{L}}\left\{-\omega_{\text{anti}}^2 + \left(\frac{k_{\text{L}} + k_{\text{R}}}{2m}\right)\right\}Q_s}{\omega_{\text{anti}}^2 m^2 \left\{-2\omega_{\text{anti}}^2 + \left(\frac{k_{\text{L}} + k_{\text{R}}}{2m}\right) + \left(\frac{k_{\text{L}} + k_{\text{R}} + 4k_{\text{c}}}{2m}\right)\right\}} \quad \text{---- 3.14}$$

$$z_{\Omega,\text{diff}} = \frac{4\Omega y_0 Q_s}{\omega_{\text{anti}}} \quad \text{---- 3.15}$$

From the derived Eqs. 3.12 and 3.15, a relation obtained that for the constant ω_{anti}, the angular rate sensitivity does not change and the larger *DR* design shows a smaller acceleration sensitivity.

3.3 Numerical analysis of acceleration sensitivity in TFG

The sense resonators described with Eq. 3.1 and detecting circuits are modelled with Matlab and Simulink as shown in Fig. 3.2. In the modelling, the rotation input signal and shock input signals are applied to the sense resonators. The left and right sense resonators displacement signals are converted into capacitance change and differentiated. After that, the signal is converted into voltage by multiplying with the gain. The differential signal is then demodulated with reference signal whose frequency is at sense anti-phase frequency and low-pass filtered. The parameters to model the TFG are shown in Table 3.1. The three different designs in the decoupling of the sense resonators are examined; *DR* = 0.09, 0.13 and 0.29. The anti-phase frequency was fixed about 16.5 kHz and the in-phase frequency was varied (fin is at 15.0 kHz, 14.4 kHz and 11.8 kHz). The TFG was operated in the mode matched condition ($\omega_d = \omega_{anti}$). The designed angular rate sensitivity is 2 μV/deg/hr. The tiny difference in the two identically designed sense resonators to imitate the fabrication error in a TFG, is introduced by increasing the beam width of the right resonator by 15 nm, considering the chip-level fabrication non-uniformity in microfabrication. The calculated stiffness unbalances are 0.305, 0.278 and 0.243 N/m for *DR* of 0.09, 0.13 and 0.29, respectively.

The analysis starts with input acceleration of a half sine shock. The amplitude and duration of the shock signal are 100-g (= 980 m/s^2) and 3 ms, respectively. Fig. 3.3(a) shows the simulated displacement of the left resonator at the moment of the shock. After the shock, the displacement oscillation decreases with a decaying envelop, which is typical response of an underdamped system after a shock input, which is shown in the inset of the Fig. 3.3(a). The signal is mainly of the in-phase vibration but the signal contains the anti-phase mode, as shown by the frequency spectrum in Fig. 3.3(b). It is noted that the demodulation system in the sensing circuit recovers only the signal at driving frequency. The sense anti-phase mode appears on the output. Therefore, we proved that the source of acceleration sensitivity arises from the sense anti-phase mode excitation due to stiffness unbalance. The gyroscope outputs of three different decoupling ratios are shown in Fig. 3.4. The outputs show that the TFG with large *DR* has smaller acceleration output. The calculated acceleration sensitivity for three DR designs 0.09, 0.13 and 0.29 are 7.71, 4.53 and 1.72 deg/hr/g, respectively. It is noted that the angular rate sensitivities are same in all three *DR* designs as shown by applying the 1 deg/hr at 0.3 s in the same simulation. Numerical analysis also verified the decoupling method.

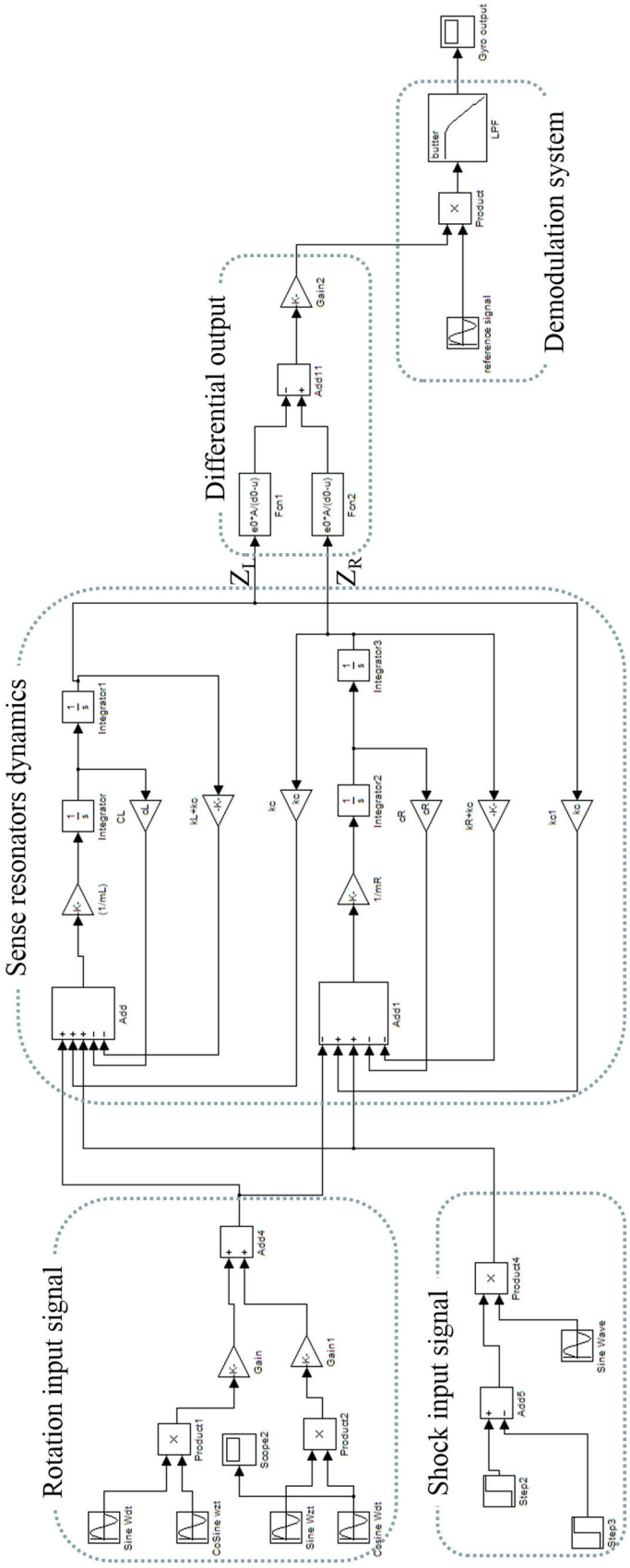

Figure 3.2 Simulink model of fully operating TFG.

Table 3.1 Parameters for numerical analysis

Decoupling ratio *DR*	0.09	0.13	0.29
Sense resonator mass m_s,μg	3.3268		
Damping coefficient $c_{s,}$,μN-s/m	1.0		
Quality factor, Q_s	345		
Resonator Stiffness (left) (k_L) N/m	29.6	27.0	18.0
Coupling stiffness (k_c) N/m	3.08	4.38	8.88
Driving amplitude, y_0	10.0		
Sense electrode gap, μm	3.0		
Sense electrode area μm^2	60900		
Sense electrode sensitivity aF/nm	59.91		

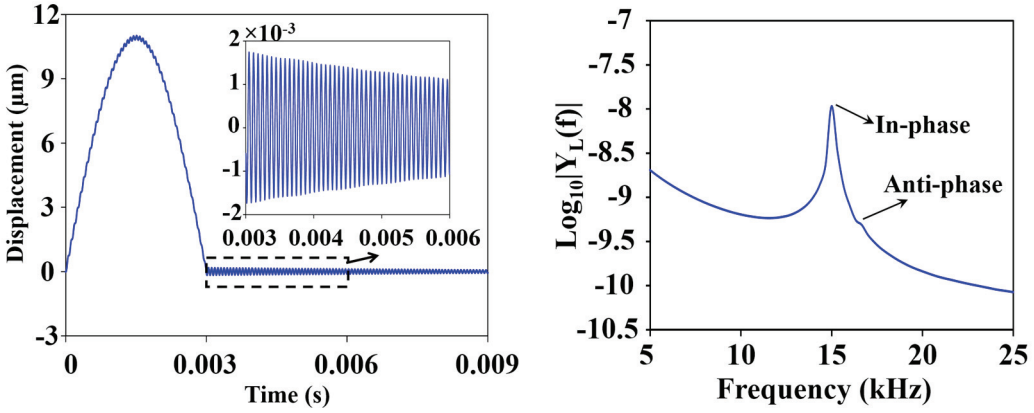

(a) (b)

Figure 3.3 Response of TFG against shock (DR=0.09, no rotation input) (a) displacement of left sensing resonator against a half-sine wave with 100-g amplitude and 3 ms duration (b) frequency spectrum of first 3 ms duration shows both in-phase and anti-phase peaks.

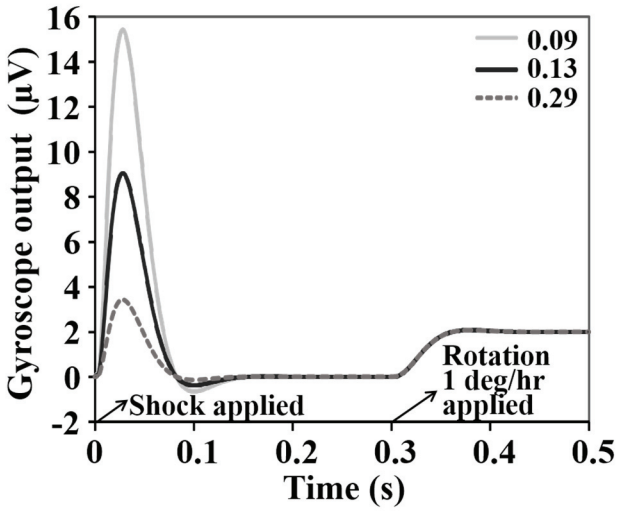

Figure 3.4 Gyroscope output of three decoupling ratio designs. Shock is applied at 0 s and a constant angular rate is applied at 0.3 s.

3.4 Summary

The theoretical and numerical analysis is performed on the x-axis TFG. In the theoretical analysis, the TFG is considered as lumped parameter model. From the equations of sense resonators motion, the differential displacement of two sense resonators is derived. The differential displacement (gyroscope output) against acceleration is proportional to stiffness unbalance and inverse to decoupling ratio and cubic of anti-phase frequency. The theoretical equations confirmed that large decoupling ratio design of TFG results into lower acceleration sensitivity and the angular rate sensitivity does not change by keeping the anti-phase frequency constant in the frequency decoupling method. In the numerical analysis, fully operational gyro (TFG) model is simulated by considering fabrication error. The amplitude and time duration of applied half sine-wave shock signal are 100 g and 3 ms, respectively. The sense resonators are vibrated in anti-phase mode against shock. The sense anti-phase vibration appears on the gyro output as acceleration output. The three *DR* designs of TFGs showed that the TFG with large *DR* had smaller acceleration output. We verified the frequency decoupling method also in numerical analysis. The numerical analysis also showed that the angular rate sensitivities are same in all three DR designs.

Chapter 4
Verification of frequency decoupling method in in-plane resonators

4.1 Overview

In this chapter, frequency responses of in-plane coupled resonators were investigated to verify the source of acceleration sensitivity and frequency decoupling method through FEA simulations and measurements. Two types of symmetric in-plane coupled resonators were designed with different coupling schemes; a frame-coupled and a spring-coupled. Two coupling methods were selected to evaluate the effect of coupling method on the acceleration output. To imitate the fabrication errors in a TFG, one of the two resonators in a coupled resonator was unbalanced in stiffness for example by 1% and 5% stiffness in FEA simulations. A frequency sweep signal with 1-g amplitude is applied to both symmetric and unbalanced resonators. The symmetric coupled resonators were fabricated on SOI wafer of 20 μm thick layer. An acceleration signal with frequency sweep was applied on the in-plane coupled resonators by using a vibration shaker.

4.2 Design of in-plane coupled resonators

To verify the source of acceleration sensitivity and frequency decoupling method in the sense resonators of TFG, two types of in-plane coupled resonators were designed. The in-plane coupled resonator represents the two sense resonators of a z-axis TFG. Two resonators are paired with two types of coupling methods based on published TFGs [98] [99] as shown in Figs. 4.1 and 4.2. In the TFG, shown in Fig. 4.1, two gyroscopes were coupled with a frame, whereas in the TFG, shown in Fig. 4.2, two gyroscopes were coupled with a spring.

4.2.1 Frame-coupled type

Two resonators are coupled with a frame, which is same as the TFG shown in Fig. 4.1. The frame-coupled resonator, named as type A, is shown in Fig. 4.3(a). Each resonator is suspended by four in-plane translational beams. The frame is anchored by using six U-shaped in-plane translational beams. Each resonator is divided into two sections with comb-type parallel plate capacitive electrodes; one is increasing type and the other decreasing type.

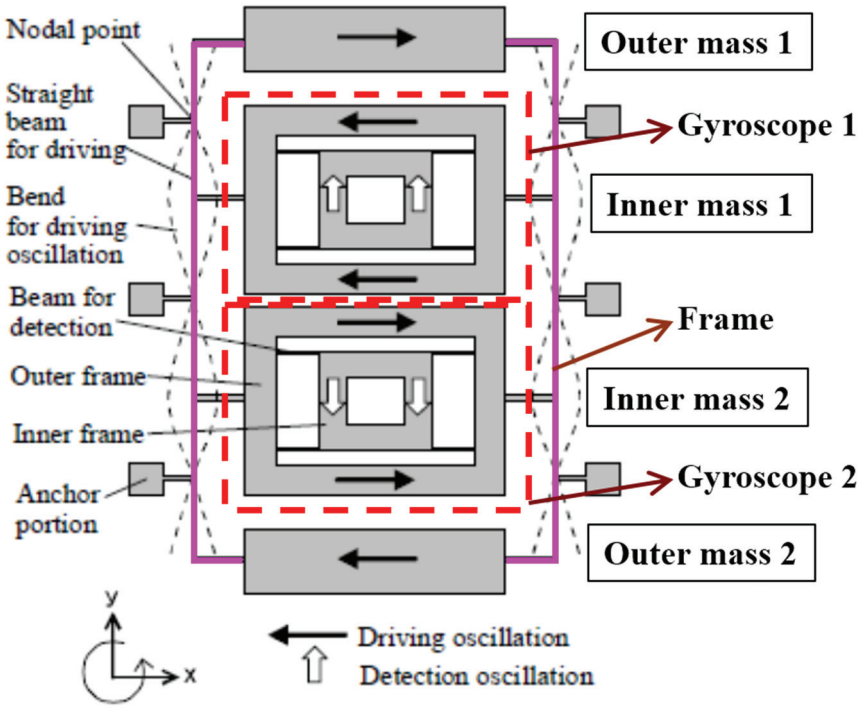

Figure 4.1 A TFG in which two gyroscopes are coupled with a frame [98].

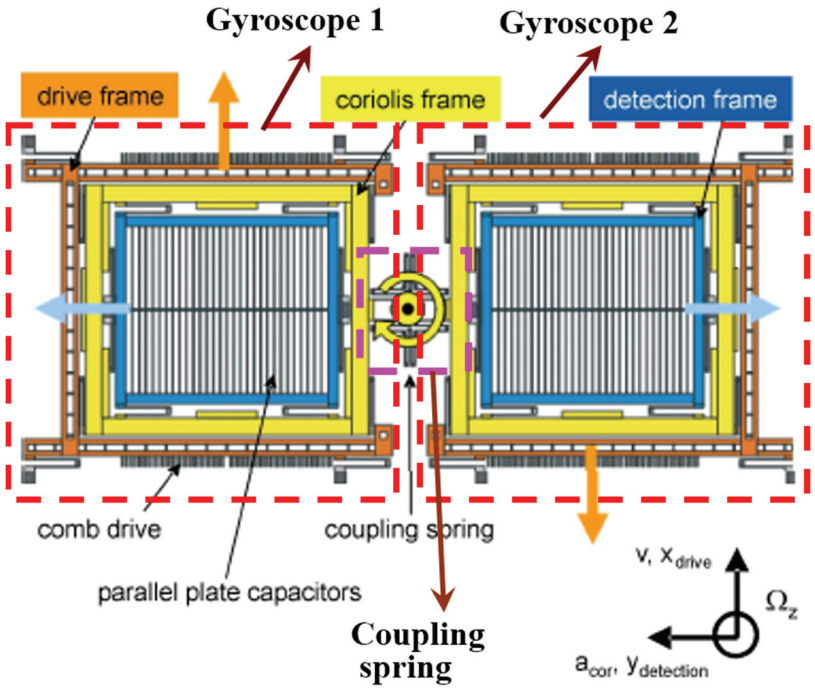

Figure 4.2 A TFG in which two gyroscopes are coupled with a spring [99].

4.2.2 Spring-coupled type

Two resonators are coupled with a spring, which is same as shown in Fig. 4.2. The spring-coupled resonator, named as type B, is shown in Fig. 4.3(b). Each resonator is suspended with four double folded springs. The coupling spring is a meander spring. Each resonator consists of increasing and decreasing capacitive electrodes, same as frame-coupled type. Both designs have in-phase (ω_{in}) and anti-phase (ω_{anti}) modal frequencies as shown in Figs 4.4 and 4.5. In the type-A design, at anti-phase modal frequency, the coupling frame does not move as shown Fig. 4.4(b). In the type-B designs, at in-phase frequency the coupling spring does not contract or expand as shown in Fig. 4.5(a).

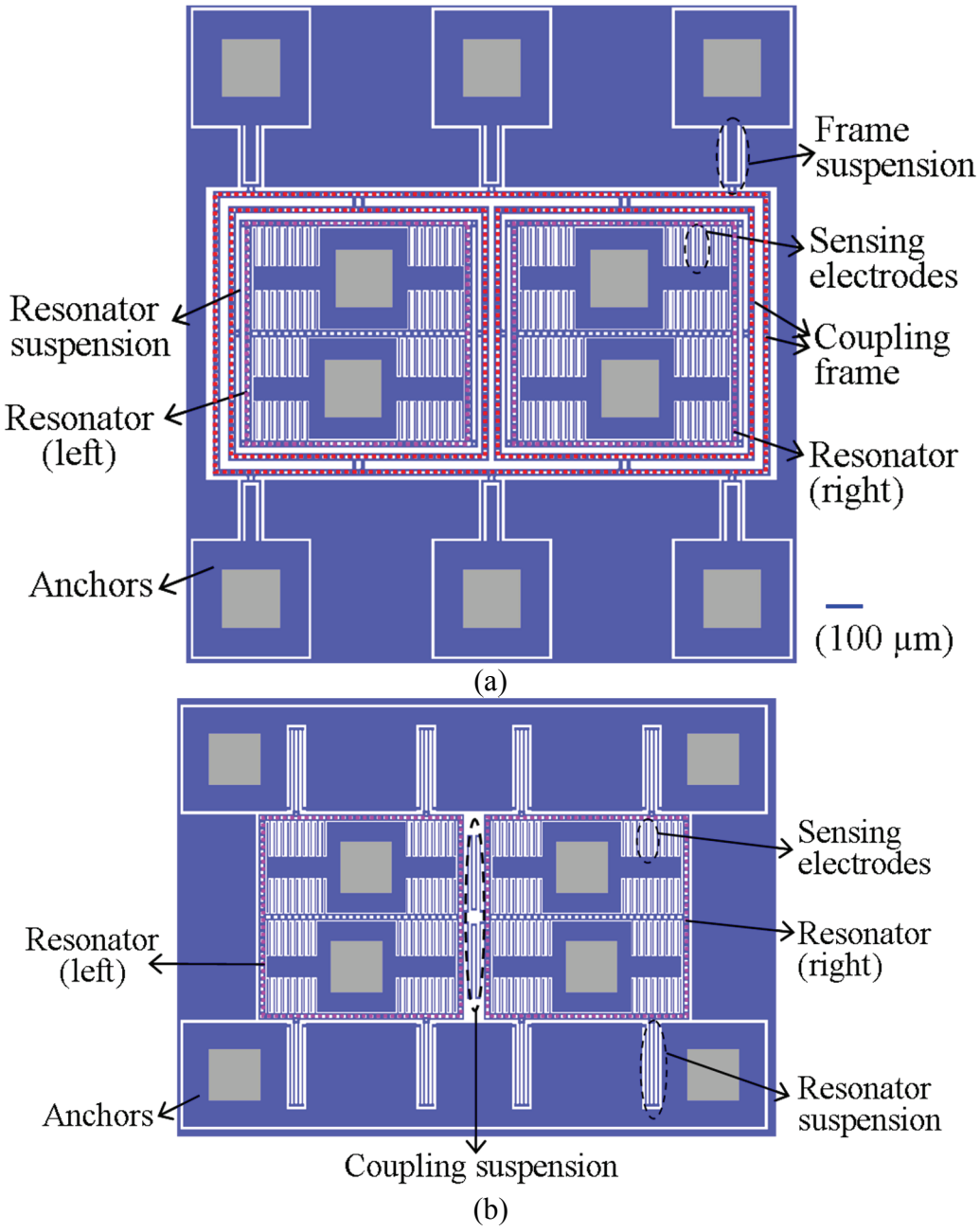

Figure 4.3 Complete layout of coupled resonators (a) type A (b) type B.

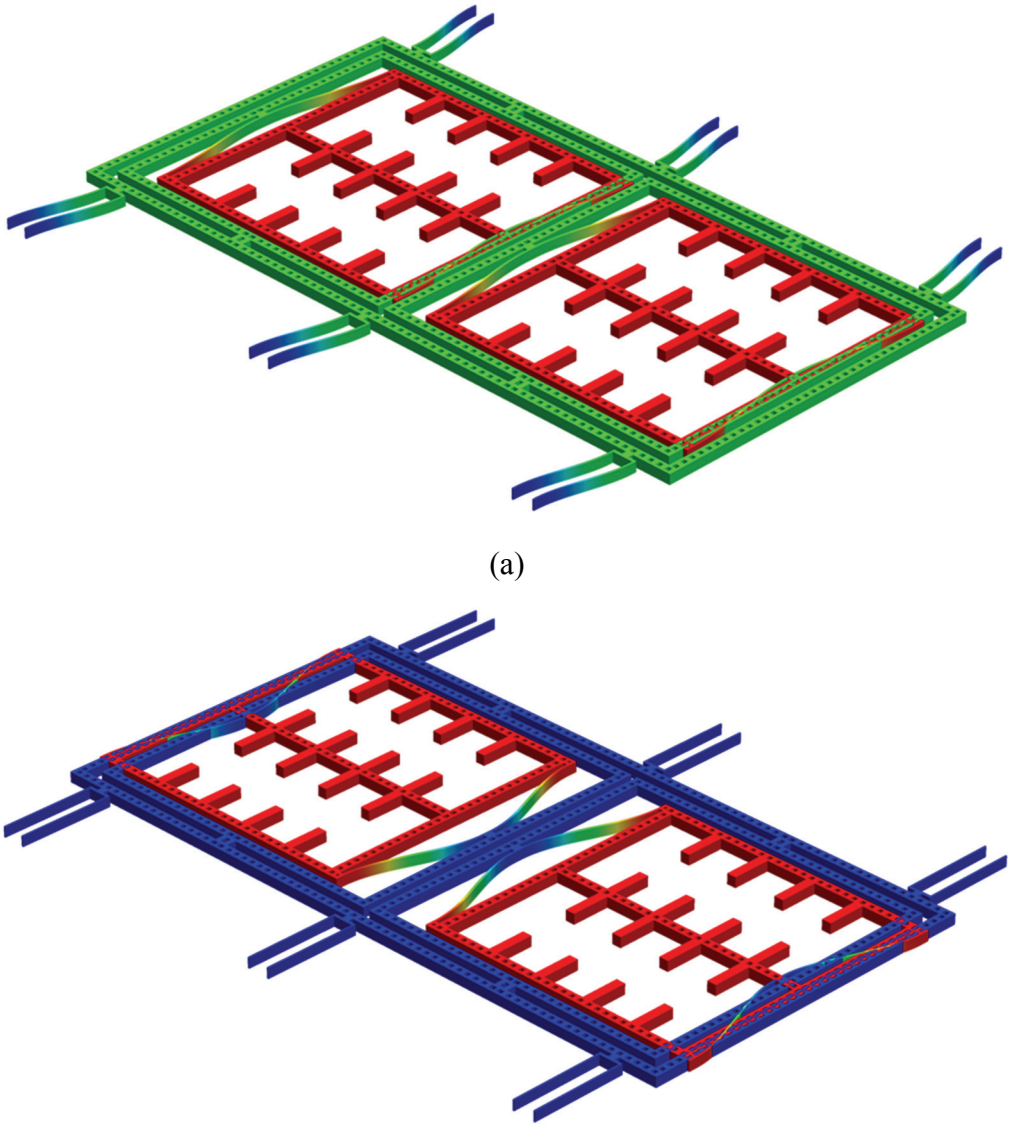

(a)

(b)

Figure 4.4 Resonant frequency modes of frame-coupled resonators (type A) (a) in-phase mode (b) anti-phase mode.

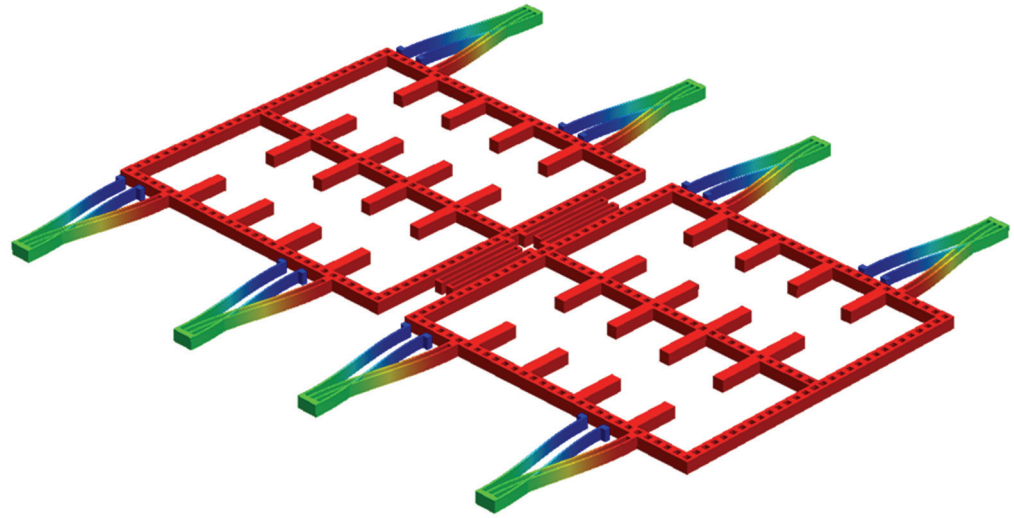

(a)

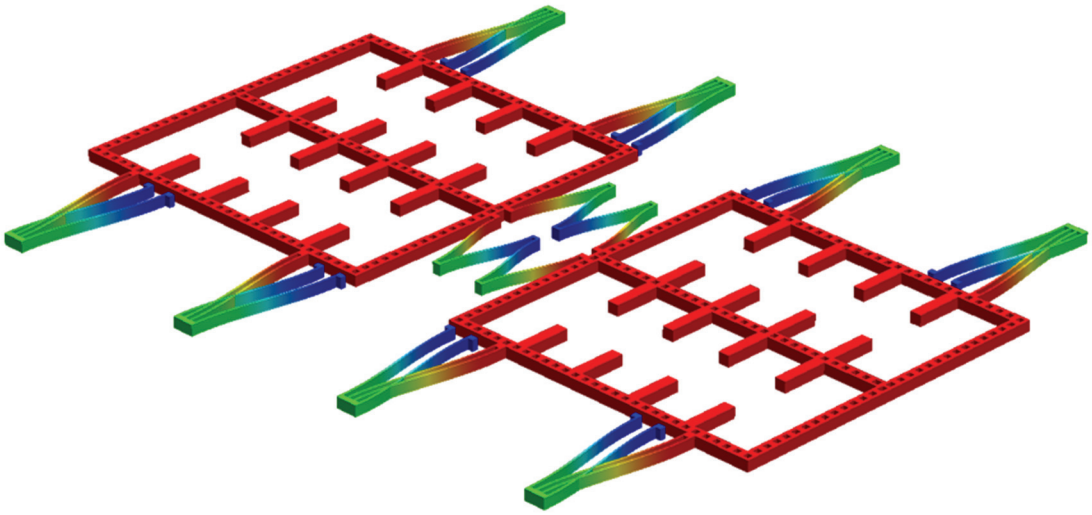

(b)

Figure 4.5 Resonant frequency modes of spring-coupled resonators (type B) (a) in-phase mode (b) anti-phase mode.

4.3 Design parameters

To compare the both designs performance against acceleration, we designed the resonators' equivalent mass to apply the same amount of force. We fixed the anti-phase frequency at 16.5 kHz and chose different in-phase frequencies to verify the frequency decoupling method. The in-phase frequency separation from the anti-phase frequency is termed as the decoupling ratio (*DR*), which is given by:

$$DR = \left(\frac{\omega_{\text{anti}} - \omega_{\text{in}}}{\omega_{\text{anti}}} \right) \qquad \text{---- 4.1}$$

The large decoupling ratio implies that in- and anti-phase frequencies are largely decoupled (separated).

The frame-coupled design (type-A) and spring-coupled design (type-B) are modelled as lumped mass-spring-damper system to calculate the in- and anti-phase frequencies as shown in Fig. 4.6. The equations of motion for frame-coupled designs are

$$\begin{aligned} m_f\ddot{x}_1 + k_f x_1 + k_r(x_1 - x_2) + k_r(x_1 - x_3) &= 0 \\ m_r\ddot{x}_2 + k_r(x_2 - x_1) &= 0 \\ m_r\ddot{x}_3 + k_r(x_3 - x_1) &= 0 \end{aligned} \quad \text{---- 4.2}$$

The solution of the above equations is given in the Appendix A. The in- and anti-phase frequencies of frame-coupled design are

$$fs_{in} = \frac{1}{2\pi}\sqrt{\frac{\left\{m_f k_r + m_r\left(k_f + 2k_r\right)\right\} - \sqrt{\left\{m_f k_r + m_r\left(k_f + 2k_r\right)\right\}^2 - 4m_r m_f k_r k_f}}{2m_r m_f}} \quad \text{---- 4.3}$$

$$fs_{anti} = \frac{1}{2\pi}\sqrt{\frac{k_r}{m_r}} \quad \text{---- 4.4}$$

where m_r and m_f are the mass weight of resonator and frame, respectively. k_r and k_f are the stiffness of the resonator and frame suspension, respectively.

The equations of motion for spring-coupled designs are

$$\begin{aligned} m_r\ddot{x}_1 + k_r x_1 + k_c(x_1 - x_2) &= 0 \\ m_r\ddot{x}_2 + k_r x_2 + k_c(x_2 - x_1) &= 0 \end{aligned} \quad \text{---- 4.5}$$

The in- and anti-phase frequencies of spring-coupled resonator are;

$$fs_{in} = \frac{1}{2\pi}\sqrt{\frac{k_r}{m_r}} \quad \text{---- 4.6}$$

$$fs_{anti} = \frac{1}{2\pi}\sqrt{\frac{k_r + 2k_c}{m_r}} \quad \text{---- 4.7}$$

where k_c is the stiffness of coupling spring. We designed both type-A and type-B with

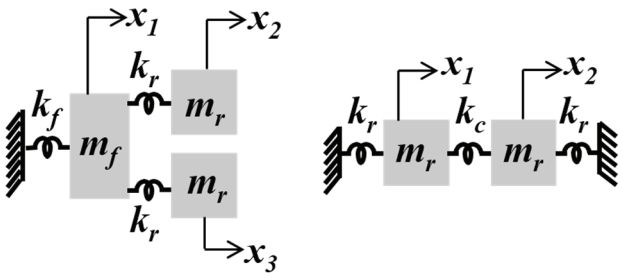

(a) (b)

Figure 4.6 Lumped mass-spring models of (a) frame-coupled (b) spring-coupled design.

three *DR*s of 0.09, 0.13, and 0.29. The decoupling ratio was varied in both designs by changing the stiffness of the suspension springs as described here. The designed spring models for type-A and type-B designs are shown in Fig. 4.7. In the type-A design, the stiffness of the anchored spring k_f and of the resonator suspension spring k_r are given by [78]:

$$k_f = 12Et\left(\frac{w_f}{l_f}\right)^3 \qquad \text{---- 4.8}$$

$$k_r = 4Et\left(\frac{w_r}{l_r}\right)^3 \qquad \text{---- 4.9}$$

where E is young's modulus (150 GPa) and t, w, and l are the thickness, width, and length of the spring beam. *DR* is varied by changing the stiffness of the anchored spring. It causes ω_{in} shift but the anti-phase frequency does not change as shown in Table 4.1

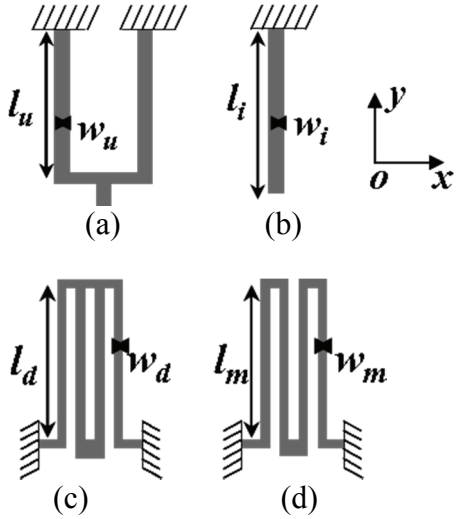

Figure 4.7 Designed spring models of (a) anchored spring and (b) suspension spring of type-A, and (c) suspension spring and (d) coupling spring of type-B.

Table 4.1 Stiffnesses of springs in type-A and type-B designs.

In-phase frequency	Type A suspension spring stiffness		Type B suspension spring stiffness	
(kHz)	k_r (N/m)	k_f (N/m)	k_r (N/m)	k_c (N/m)
0.09	39	442	30.1	5.2
0.13	39	288	28.1	6.6
0.29	39	121	19.1	19

In the type-B design, the stiffness of the anchored k_r and coupling k_c springs are given by:

$$k_r = 4Et\left(\frac{w_r}{l_r}\right)^3 \qquad \text{---- 4.10}$$

$$k_c = Et\left(\frac{w_c}{l_c}\right)^3 \qquad \text{---- 4.11}$$

The derivation of the stiffnesses of suspension beams are given in Appendix B. In the type-B, the stiffness of both the anchored and coupling springs were modified to keep the anti-phase frequency at about 16.5 kHz and to shift the in-phase frequency as shown in Table 4.1. In the type-A design, the dimensions excluding the anchors were 1450×1150 μm^2, and in type-B, 1300×1200 μm^2. In both designs, the unit resonator mass dimensions were fixed to 600×600 μm^2 and thickness t was 20 μm. The resonator mass-weight size is 33.268×10^{-10} kg and the frame-weight size is 70.189×10^{-10} kg. Etch hole size is kept as 10×10 μm^2 to make the designs suitable for the actual fabrication. Each resonator had parallel plate capacitors divided into two sections with increasing and decreasing types of electrode pattern and a total of 36 electrodes were used in each section with 3 μm gap. Base capacitance and the displacement sensitivity were 200 fF and 66 af/nm.

4.4 Fabrication process

The designed coupled resonators were fabricated on a silicon-on-insulator (SOI) wafer with the device layer of 20 μm thick. We fabricated the *DR* designs of 0.13 and 0.29 in which the anti-phase frequency was set at 16.5 kHz. In the designs with *DR* of 0.09, the anti-phase frequency was set at 12.0 kHz since the undesired modes exist near the anti-phase frequency of 16.5 kHz. The fabrication process is shown in Fig. 4.8. At first, aluminum metallization on the SOI wafer was done for bond pads. After that, the device structures were patterned using deep-reactive-ion- etching (DRIE). The buried oxide layer was etched with HF vapor to release the movable structures. The SEM images of the two designs are shown in Fig. 4.9. The chips were mounted on custom made ceramic packages and wire bonded for electrical contacts. The packages are sealed in vacuum at a pressure of 100 Pa.

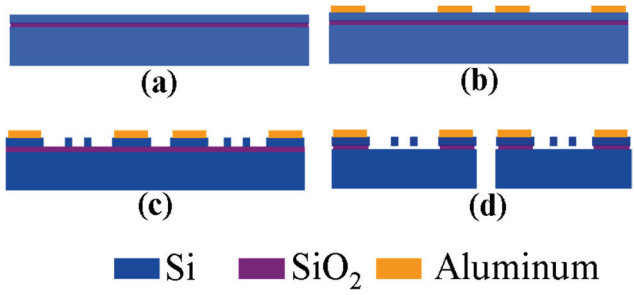

Figure 4.8 SOI fabrication process: (a) a bare SOI wafer of 20 μm thick, (b) aluminium metallization (c) structural Si layer etching by DRIE (d) releasing and dicing of the devices.

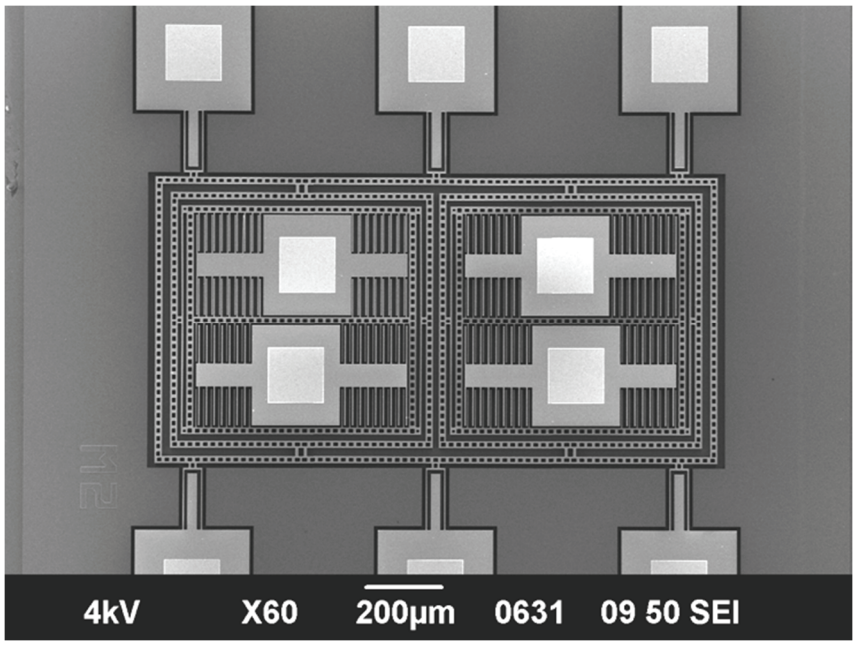

(a)

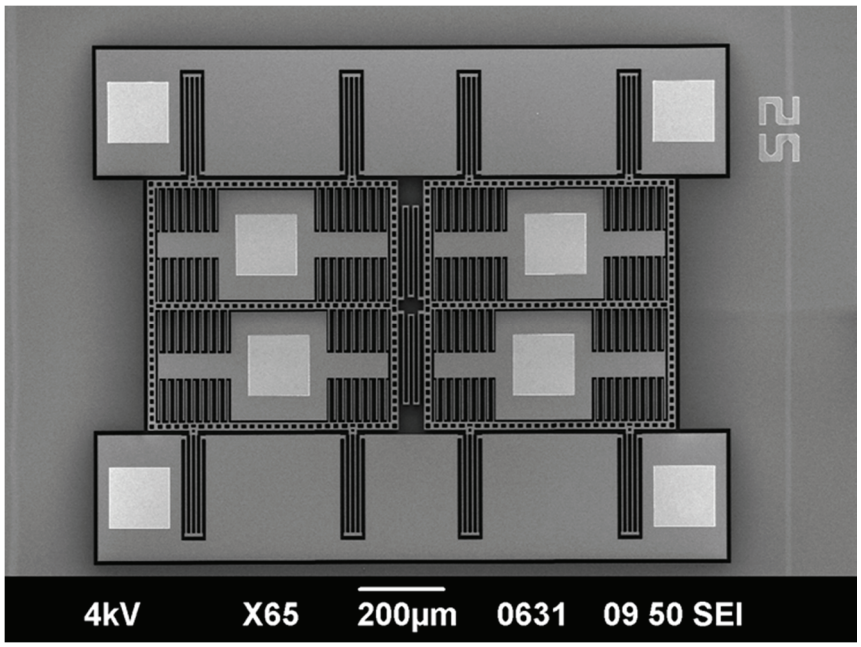

(b)

Figure 4.9 SEM images of (a) type A (frame-coupled) and (b) type B (spring-coupled).

4.5 Measurement setups

The packaged coupled resonators were soldered on a printed-circuit-board (PCB) for connecting to an off-chip detecting circuit, whose capacitance sensitivity is 3.77 mV/fF. The detecting circuit consists of two C-V (charge to voltage) amplifiers and a differential amplifier. The differential output was connected to a lock-in-amplifier (LIA) and the output was recorded by a memory hi-coder.

4.5.1 Electrical frequency sweep test setup

In the electrical measurement setup shown in Fig. 4.10, one of the resonators of a coupled resonator was actuated by electrostatic force and the other resonator response was detected. The movable structure was biased at 3.1 V. For oscillation, a dc bias voltage of 8 V was applied on both sets of the fixed electrodes, and an ac voltage of 0.2 V with a frequency sweep range from 10-20 kHz was applied on the other set of the fixed electrodes of the actuating resonator. For the sensing, two sets of the fixed electrodes of the other resonator were biased to the ground and connected to the detecting circuit. From the measured frequency response of the resonator, both the in- and anti-phase modes were evaluated and the Q-factors were calculated from the half power bandwidth.

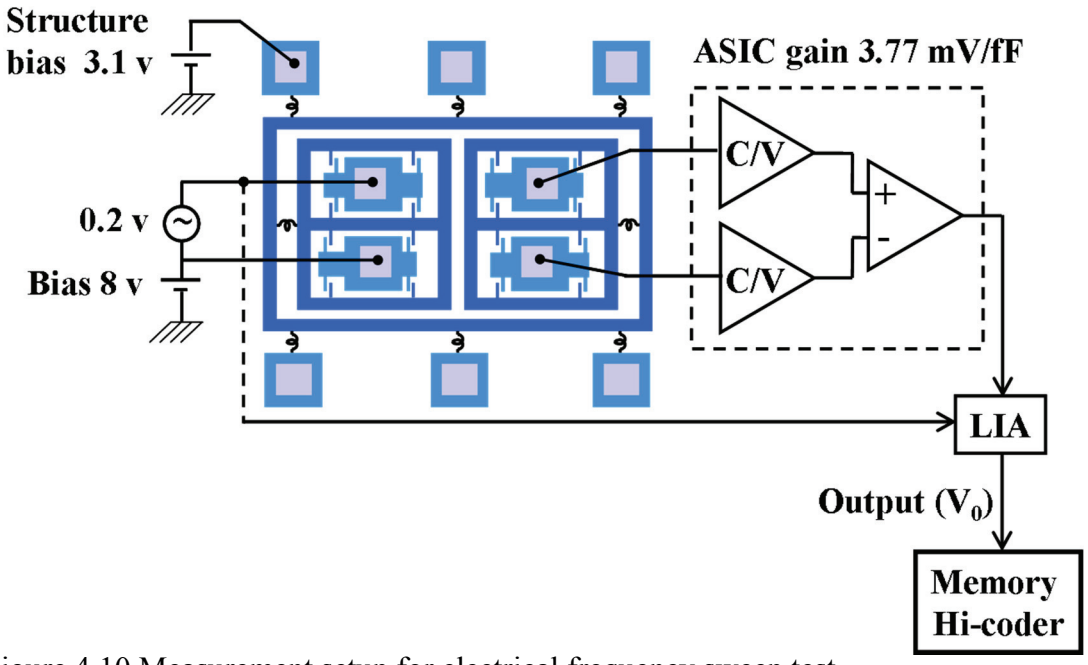

Figure 4.10 Measurement setup for electrical frequency sweep test.

4.5.2 Mechanical frequency sweep test setup

We used a vibration shaker to apply acceleration with frequency sweep. The evaluation setup is shown in Fig. 4.11. The PCB was fixed to an aluminium block by using an adhesive, which was attached to centre of the shaker, such that the sensing- axis was aligned to the vibration axis of the shaker. A sinusoidal excitation with 1-g (= 9.8 m/s^2) amplitude and a frequency sweep range from 9 to 19 kHz was applied. A reference accelerometer was placed on the aluminium block to monitor the acceleration. The fixed electrodes of the two resonators were connected to the off-chip detecting circuit such that if two resonators vibrate in the anti-phase mode, the capacitance changes are added as shown in the insets of Fig.4.11.

4.6 FEA harmonic simulations

Finite element analysis (FEA) harmonic simulations were carried out on the coupled resonators using Coventorware software [100]. The applied conditions were 1-g acceleration with a frequency sweep of 10-18 kHz and a Q-factor of 320. In the simulations, we introduced fabrication error by changing the stiffness of one resonator, since ideally fabricated coupled resonators do not display anti-phase mode excitation as shown in Fig. 4.12. The unbalance of 1 % or 5 % stiffness was created through increasing the stiffness of one of the resonators by increasing the width of the suspension beams. In the simulations, the parallel plate electrodes were replaced with the equivalent electrodes mass for reducing calculation time of simulations.

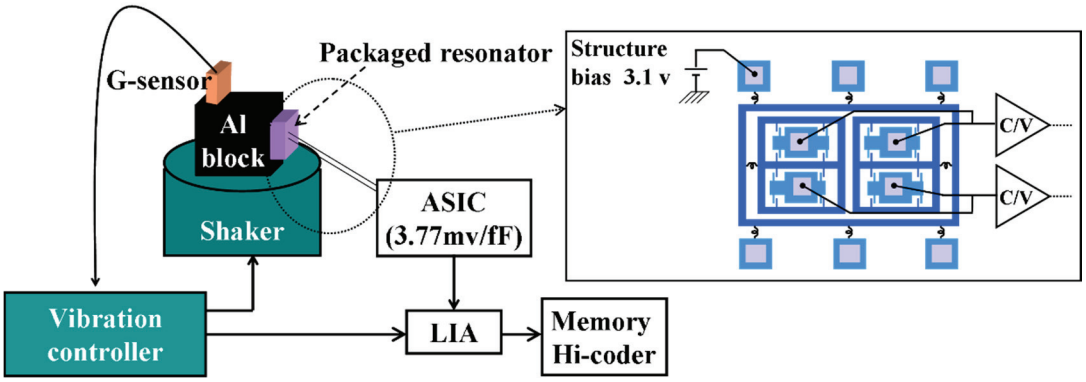

Figure 4.11 Measurement setup for mechanical frequency sweep test.

4.6.1 Results

The frequency responses of the 5 % unbalanced type-A design with *DR*=0.09 and *DR*=0.29 are shown in Fig. 4.13. The displacement magnitude and phase response of the two resonators showed that at nearly the designed anti-phase frequency (ω_{anti}), they are excited in the anti-phase mode. The FEA simulations were carried out on other *DR* coupled resonators with 1 % and 5 % stiffness unbalance to check the in-phase frequency influence on the anti-phase amplitude (frequency decoupling method).

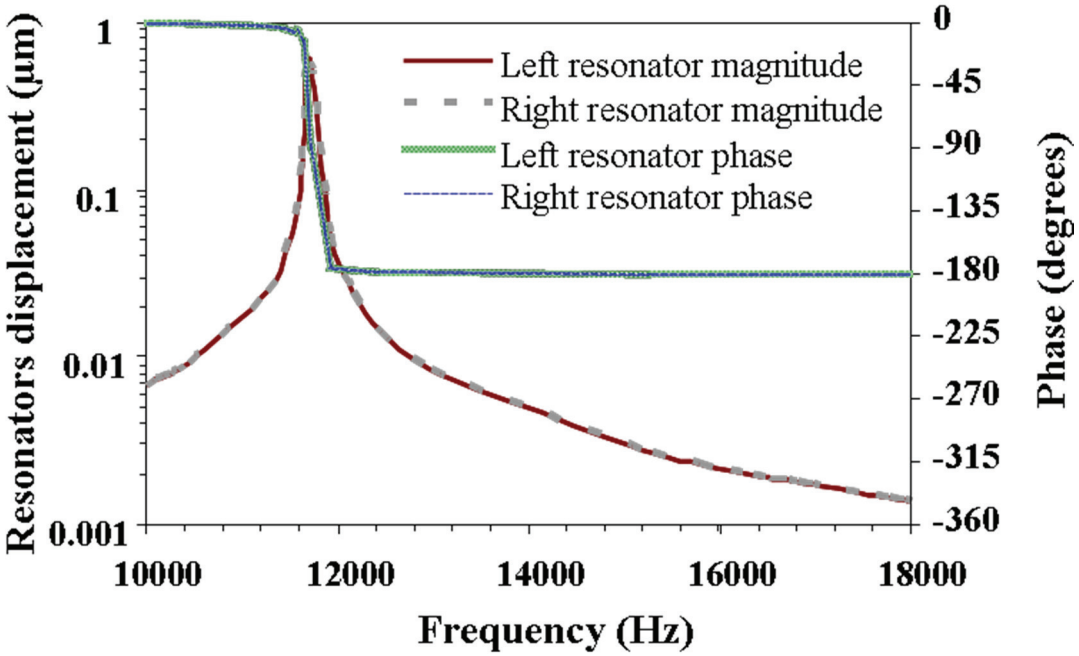

Figure 4.12 Frequency response of the ideal (symmetric) coupled resonators of type A.

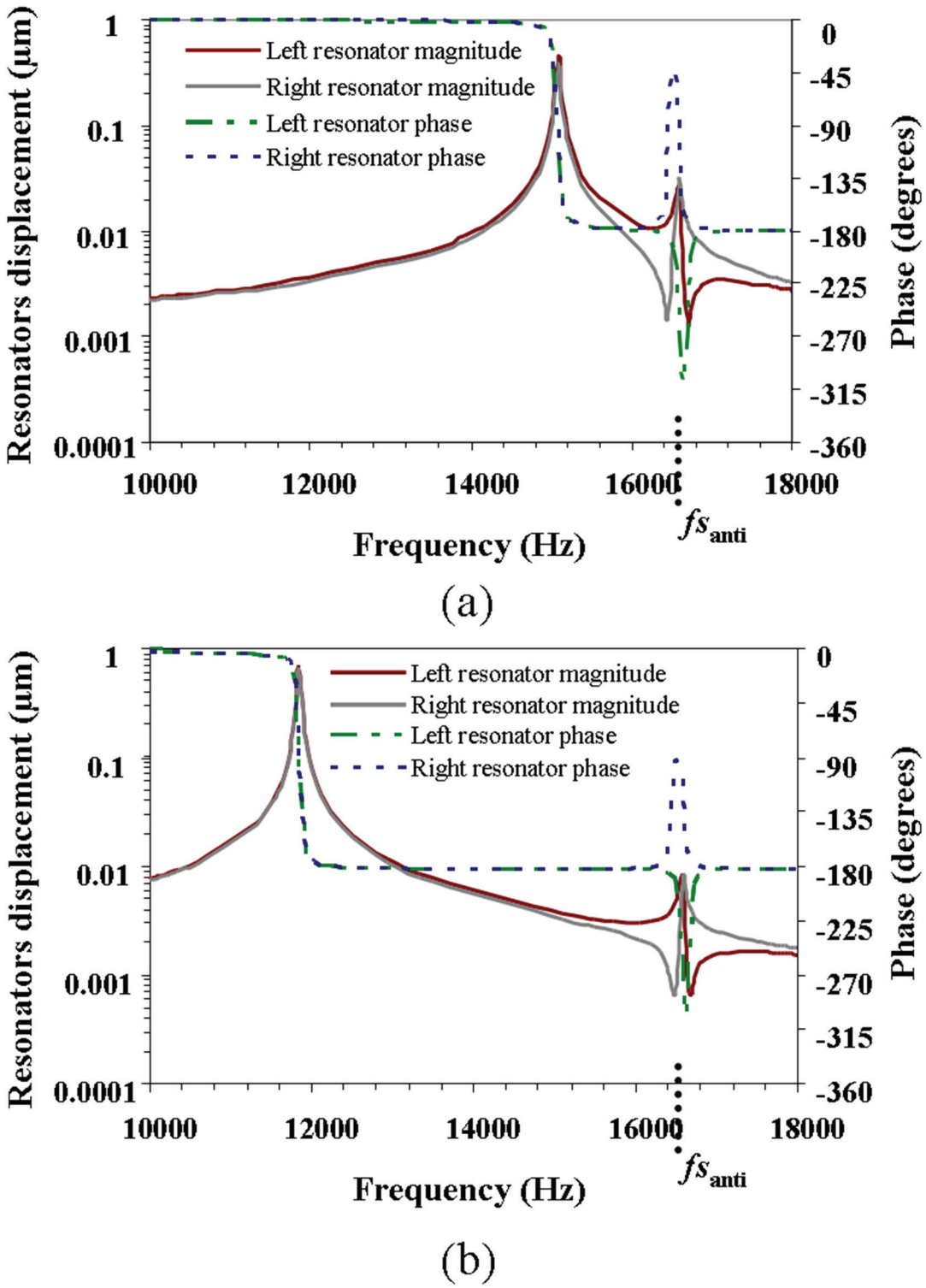

Figure 4.13 Frequency response of 5 % stiffness unbalanced type A coupled resonators with (a) $DR = 0.09$ and (b) $DR = 0.29$.

The anti-phase displacement amplitudes of two resonators are added differentially and converted in terms of capacitance change. The output capacitances were plotted against the different decoupling ratios at the anti-phase frequency, as shown in Fig. 4.14. The results showed that as the decoupling ratio increases the output capacitance decreases. In the case of type-A, at 5 % stiffness unbalance, the output capacitance decreased from 7.72 fF to 2.16 fF and at 1 % stiffness unbalance, the capacitance decreased from 1.62 fF to 0.45 fF. In the case of type-B, at 5 % stiffness unbalance, the output capacitance decreased from 7.4 fF to 2.0 fF and at 1 % stiffness unbalance, the capacitance decreased from 1.6 fF to 0.4 fF. The output capacitance was converted into the equivalent acceleration sensitivity of the example TFG described in the Chapter 3. The Coriolis induced differential displacement x_{diff} is (from Eq. 3.15)

$$x_{\text{diff}}(\omega_{\text{d}} = \omega_{\text{s}}) = \frac{4\Omega \cdot y_0 \cdot Q_{\text{s}}}{\omega_{\text{s}}} \qquad \text{---- 4.12}$$

where ω_{s} is the sense anti-phase frequency and ω_{d} is the operation frequency. Some of the TFG operating parameters were assumed in calculating x_{diff} such as the driving amplitude (y_0) of 10 µm and the operation frequency was the same as the sense anti-phase frequency (matched-mode condition) of 16.5 kHz. The calculated rate sensitivity of the TFG was 1.132 fF/deg/s. From Eq. 3.12, the rate sensitivity value is same for all decoupling ratio TFGs. The FEA simulation results of anti-phase displacements were normalized against the rate sensitivity and plotted as the acceleration output in Fig. 4.14. The results showed that for a 1 % stiffness unbalance the acceleration sensitivity decreased from 5.65 to 1.43 deg/s/g.

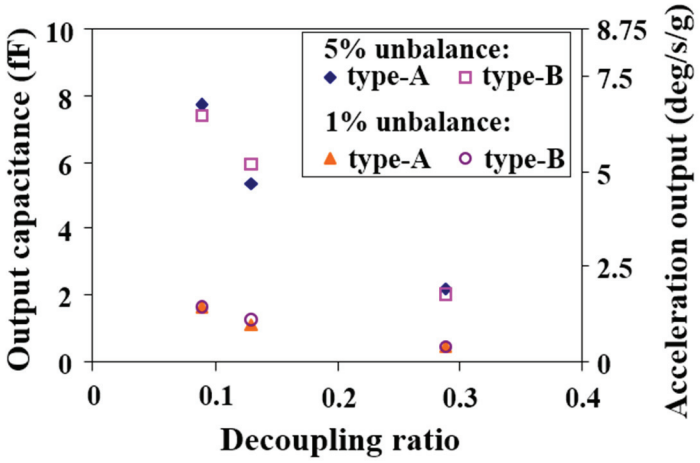

Figure 4.14 Capacitance change and equivalent angular rate change against 1-g acceleration as a function of decoupling ratio.

4.7 Measurement results

4.7.1 Electrical oscillation

The electrical frequency sweep results are plotted in Fig. 4.15. There are two resonance peaks appearing near the designed in- and anti-phase frequencies in all the designs. The measured in- and anti-phase frequencies and their Q-factors are listed in Table 4.2. There is a difference between designed and measured frequency values at in- and anti-phase vibration modes. In the designs with DR of 0.29, the in-phase frequency was set at 11.81 kHz. However, the measured frequency was at 10.53 kHz in the type A. This difference is caused by the narrower beam width and smaller mass-weight from the designed value after fabrication. The Q-factors in both types are nearly the same. For a fair comparison between the two types of coupled resonators, Q-factors should be the same since Q-factor amplifies the vibration output. The electrical frequency sweep results reveal that there is barely any frequency decoupling effect on anti-phase vibration output.

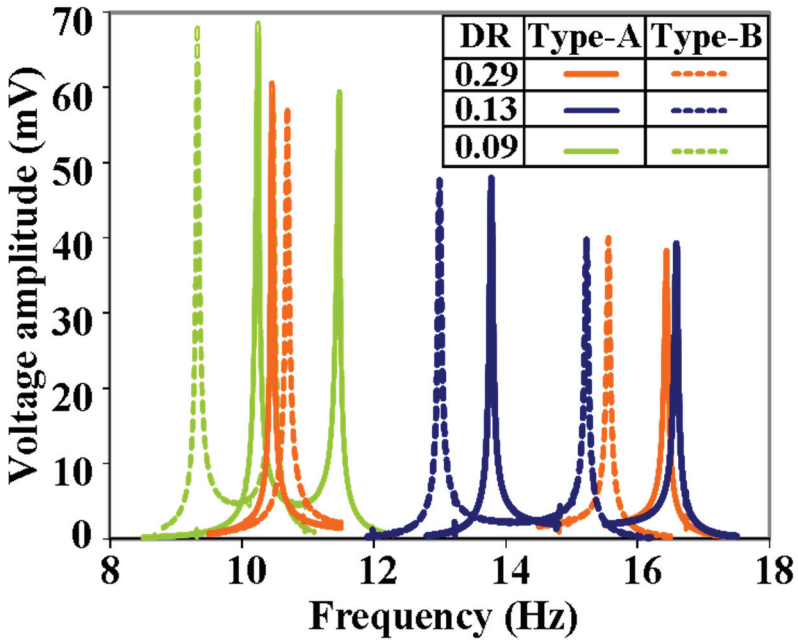

Figure 4.15 Electrical frequency sweep results of type A and type B.

Table 4.2 Deigned frequency and measured frequency of type-A and type-B designs.

Designs	DR	Designed frequency (kHz)		Measured frequency response (kHz)			
				In-phase		Anti-phase	
		f_{in}	f_{anti}	f_{in}	Q_{in}	f_{anti}	Q_{anti}
A	0.29	11.81	16.46	10.53 -10.74	287 -307	16.49 -16.62	317 -342
	0.13	14.34	16.46	13.67 -13.70	292 -320	16.61 -16.64	315 -338
	0.09	10.85	11.94	10.24 -10.26	228 -249	11.47 -11.49	234 -244
B	0.29	11.75	16.54	10.42 -10.64	233 -245	15.45 -15.57	331 -338
	0.13	14.26	16.45	12.83 -13.03	279 -283	15.03 -15.26	311 -338
	0.09	10.82	11.95	9.32 -9.37	213 -246	10.46 -10.53	218 -256

4.7.2 Mechanical oscillation

The mechanical frequency sweep results of type A and type B designs are plotted in Figs. 4.16 and 4.17, respectively. The measured frequencies of two resonance peaks are almost equal to those measured in the electrical oscillation measurements.

The amplitude at the anti-phase mode is plotted against the measured decoupling ratio (*DR*) as shown in Fig. 4.18. The *DR* value was calculated using the measured in- and anti-phase frequencies. The Fig. 4.18 shows that the anti-phase vibration output of each design is distributed between the chips, since the unbalance in stiffness and mass-weight caused by fabrication error varied from one chip to another. In the both types, the anti-phase vibration output decreases with the increase in *DR* value.

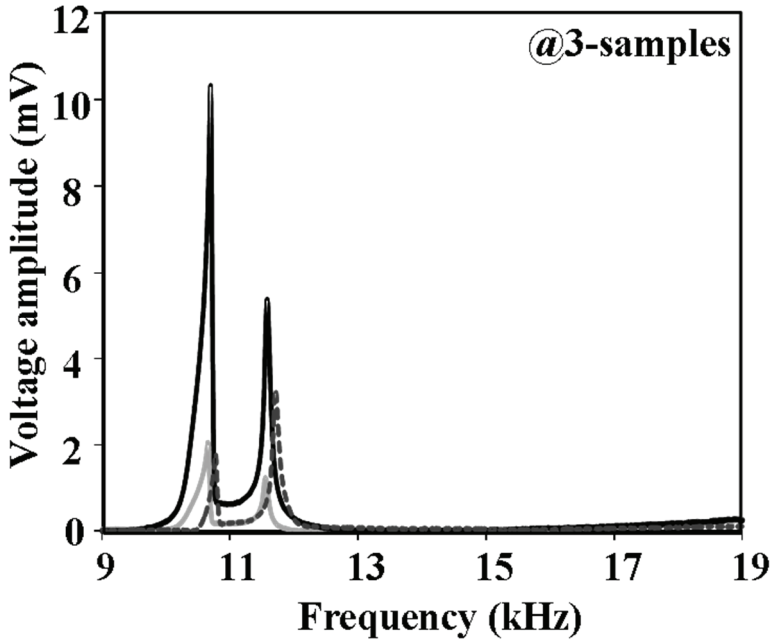

(a)

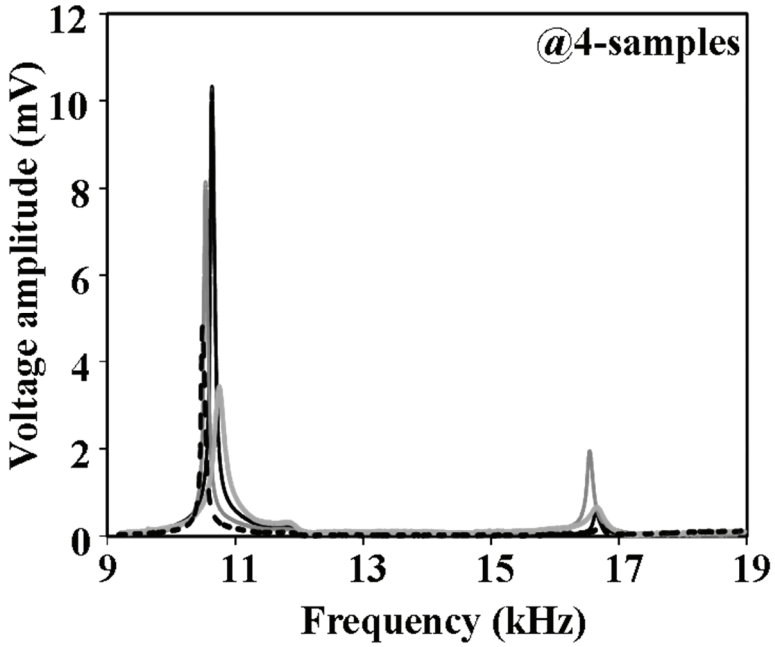

(b)

Figure 4.16 Mechanical frequency responses of type A (frame-coupled) resonators (a) *DR* =0.09 (b) *DR*=0.29.

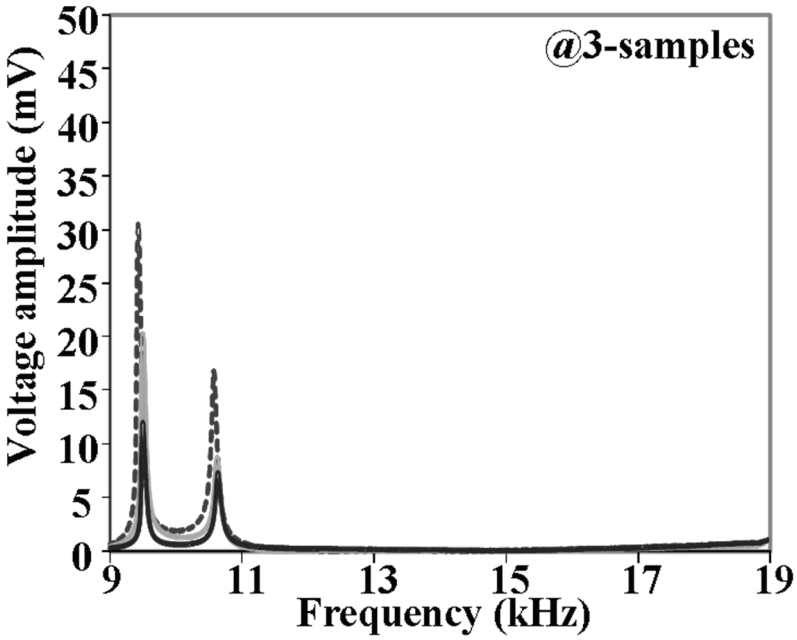

(a)

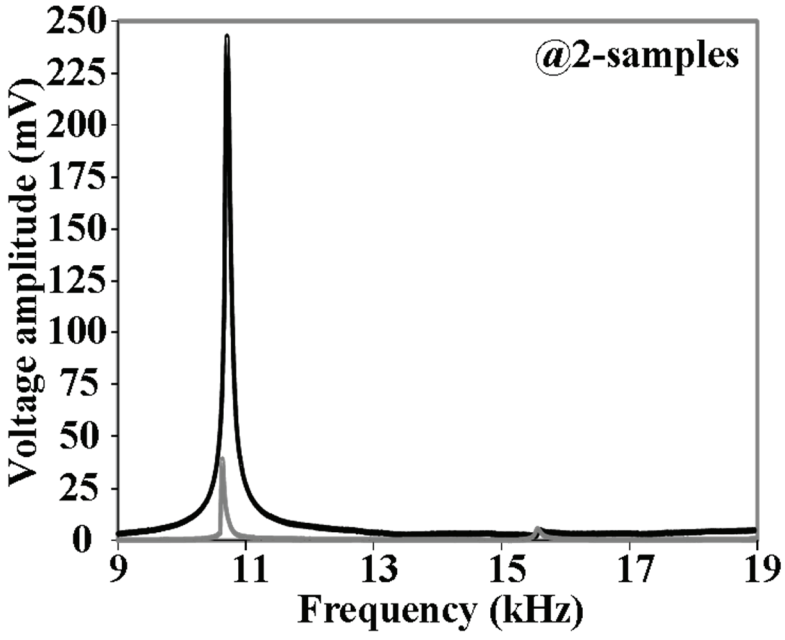

(b)

Figure 4.17 Mechanical frequency responses of type B (spring-coupled) resonators (a) *DR* = 0.09 (b) *DR*= 0.29.

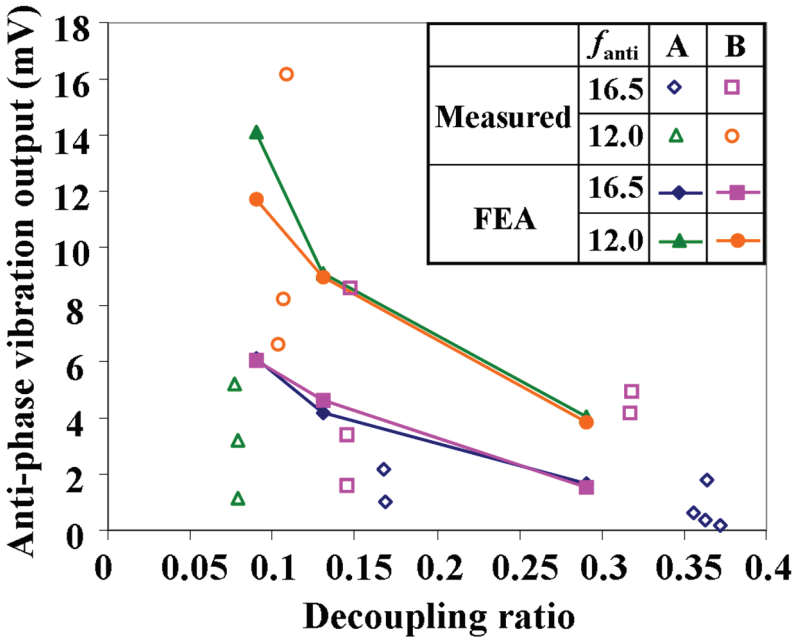

Figure 4.18 Anti-phase vibration output against measured decoupling ratio.

4.8 Discussion

From the Figs 4.13 (FEA), and 4.16 and 4.17 (measurements), we observed that the both the in-phase anti-phase modes were appeared on the frequency response. The anti-phase motion against acceleration is same as Coriolis sensing motion due to rotation input. This anti-phase mode excitation appears on the gyroscope output as an acceleration output, because the demodulation system in the sensing circuit recovers the signal whose frequency is at sense anti-phase frequency in the matched-mode operation of gyroscopes. We verified that the stiffness unbalance causes excitation of anti-phase mode, which will result into acceleration output in a TFG.

The simulation and experimental results in Figs. 4.14 and 4.18 showed that a large decoupling ratio design resulted smaller anti-phase vibration output. The proposed frequency decoupling method, which is “sense in-phase mode should be separated as far as possible from the sense anti-phase mode”, was verified through FEA simulations and experiments.

The measurement results showed that the anti-phase vibration output of type-A designs (frame-coupled) is smaller than the type-B designs (spring-coupled). However, there are discrepancies in the measured frequencies and decoupling ratio. The theoretical Eq. 3.12 showed that the differential anti-phase amplitude is proportional to stiffness unbalance and inverse to *DR* and cubic of anti-phase frequency. So, we have considered three possible causes of the difference in anti-phase vibration output: the anti-phase frequency,

the decoupling ratio and stiffness unbalancing between two unit resonators. First, the measured anti-phase frequencies of type B designs are smaller than type A designs and second in measured the decoupling ratio, type B is smaller than type A that might be caused higher anti-phase vibration output of type B designs. Third, we consider the effect of the stiffness unbalance between two unit resonators caused by fabrication error. Since the two types of coupled resonators have different vibration system structure, the effect of fabrication errors on the stiffness unbalance might be different. Therefore, we assume a fabrication error value between two resonators of a coupled resonator, i.e., the width of suspension springs of one resonator decrease by the value. To assume the value, the measured results were compared with the simulated outputs in Fig. 4.18. The outputs of type-B with *DR* of 0.09 are equivalent in the fabrication error range of 6 nm to 15 nm by comparing with the simulation result, in which a 10 nm fabrication error was introduced. We considered the fabrication error as 15 nm and calculated the stiffness unbalance Δk, ($=k-k_{15\text{nm}}$) between two unit resonators.

The stiffness values were calculated using the reported stiffness equations of two types of design in section 4.3. The obtained unbalances for the fabricated designs are given in Table 4.3.

The type A designs have larger stiffness unbalance than the type B designs. This arises from the different spring dimensions i.e., type B designs have a spring width of 3.0 μm whereas type A designs have a width of 3.2 μm to 4 μm. Since the in-plane stiffness is proportional to cubic of width, the type A designs have large stiffness unbalance. The theoretically derived differential displacement Eq. 3.12 which is given here.

$$z_{\text{a,diff}} = \frac{F(\Delta k)Q_s}{\omega_{\text{anti}}^3 m^2 (\omega_{\text{in}} + \omega_{\text{anti}})(DR)} \qquad \text{---- 4.13}$$

The above equation is used to normalize the measured results with the designed values. For that the Eq. 4.13 is modified as,

$$z_{\text{normalized}} = z_{\text{measured}} \frac{DR_{\text{measured.}}}{DR_{\text{design}}} \frac{(f_{\text{anti}}^3)_{\text{measured}}}{(f_{\text{anti}}^3)_{\text{designed}}} \frac{(f_{\text{in}} + f_{\text{anti}})_{\text{measured}}}{(f_{\text{in}} + f_{\text{anti}})_{\text{designed}}} \frac{(\Delta k_{15\text{nm}})_{\text{spring-coupled.}}}{\Delta k_{15\text{nm}}}$$

---- 4.14

In the normalization process, we considered the type-B (spring-coupled) designs of 16.5 kHz anti-phase frequency as reference for normalizing with the stiffness unbalances. All the results of type A and type B designs were normalized with the anti-phase frequency of 16.5 kHz designed decoupling ratio and calculated stiffness unbalances. In

the *DR* of 0.09 designs, anti-phase frequency was designed as 12.1 kHz, whereas in other *DR* designs it was 16.5 kHz. As we know from theoretical analysis that the angular rate sensitivity is same if the anti-phase frequency is kept constant and given the same Q-factor. Also, the differential displacement give in Eq. 4.13 is proportional to Q-factor. In the measurements, the Q-factor of 0.09 design is 235, which is smaller than compared to Q-factor of 320 in other designs. So, in normalizing the *DR* of 0.09 design to 16.5 kHz, we considered the Q-factor and multiplied the Eq. 4.14 with a factor =(Q-factor of 16.5 kHz/ Q-factor of 12.1 kHz). The calculated stiffness unbalances in *DR* of 0.09 designs with ω_{anti} of 12.1 kHz given in Table 4.3 are smaller than the simulated designs with ω_{anti} of 16.5 kHz are 0.438 N/m (type A) and 0.44 N/m (type B). Since, the differential amplitude is proportional to stiffness unbalance (from Eq. 4.13), in normalizing the *DR* of 0.09 design with stiffness unbalance, the Eq. 4.14 is multiplied with a factor of =(Δk of 16.5 kHz/ Δk of 12.1 kHz). The normalized results are plotted in Fig. 4.19, which reveals that the outputs of type A (frame-coupled) and type B (spring-coupled) designs are generally same. After normalization, the anti-phase outputs are still distributed in the same design. In the normalization, we assumed a constant dimension difference which is ideal. However, in the actual microfabrication, the scatterings in the chip-level non-uniformity is inevitable. The Δk values would be the average errors among the chips, therefore the smaller *DR* resonator has larger distributions. The normalization of measured results indicates that to suppress the acceleration sensitivity in TFGs, sense resonators have to be designed with large decoupling ratio.

4.9 Electrical measurement setup for verifying the decoupling method

The electrical measurement results in Fig. 4.10 show hardly any dependence of decoupling ratio on the anti-phase vibration amplitude. Such unprecedented findings may be caused by the excitation method, where only one resonator was excited whereas in the mechanical excitation, two resonators were simultaneously excited. To ascertain the effect of decoupling by the electrical excitation, the resonators have to be excited simultaneously by electrostatic force to mimic the in-phase acceleration on two resonators

Table 4.3 Calculated stiffness unbalances for 15 nm fabrication error.

DR	Type A, Δk (N/m)	Type B Δk (N/m)
0.09	0.278	0.282
0.13	0.438	0.42
0.29	0.438	0.261

in mechanical excitation. Electrical measurement setup will be used for future evaluation of simultaneous excitation, wherein two resonators are excited by applying the same DC and AC voltage amplitudes to the two sets of fixed electrodes (which have the same electrode pattern in two resonators) while the remaining two sets of fixed electrodes are connected to the detecting circuit as shown in Fig. 4.20.

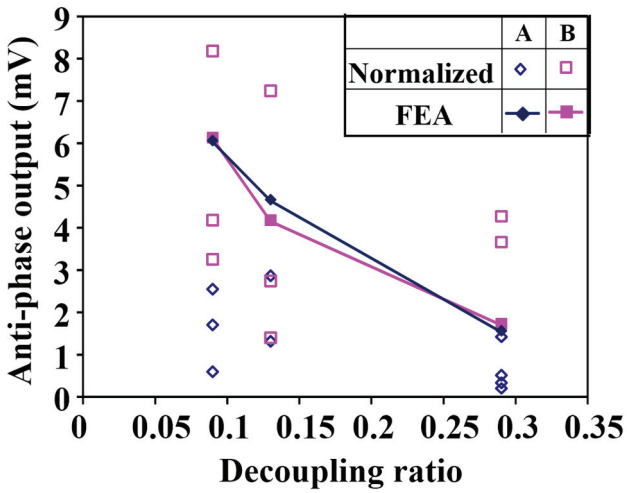

Figure 4.19 The normalized anti-phase vibration outputs of type A and type B.

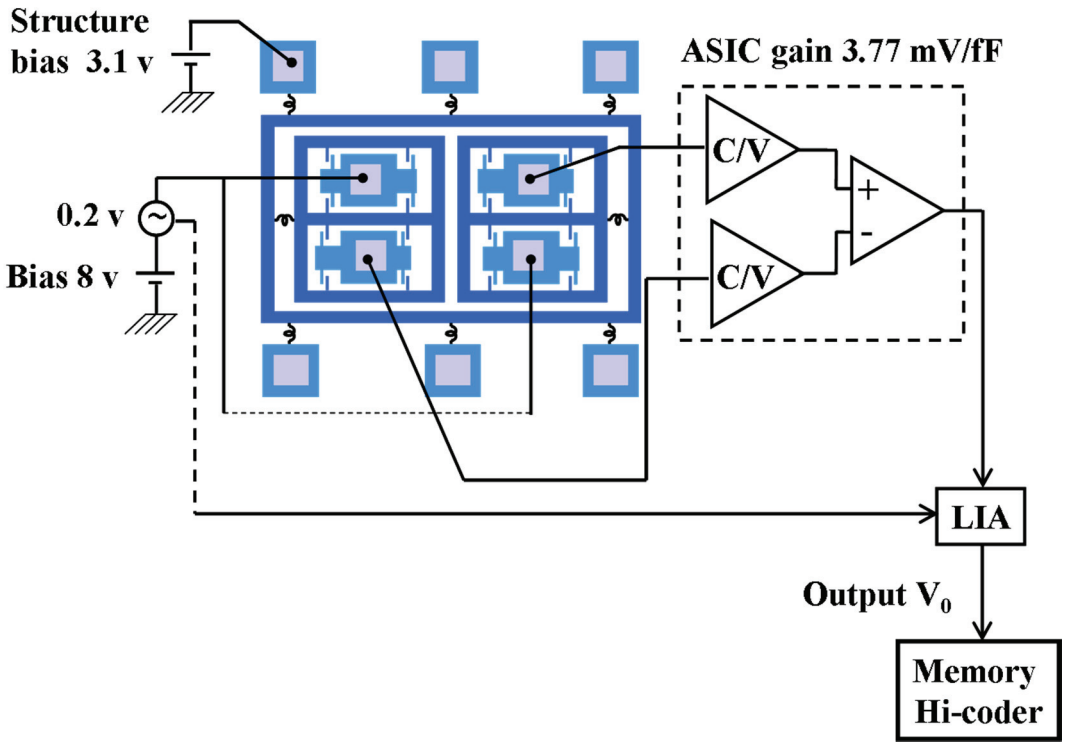

Figure 4.20 New electrical measurement setup for frequency decoupling method verification.

4.10 Summary

We designed in-plane coupled resonators to verify the source of acceleration output and frequency decoupling method through FEA simulations and experiments. The FEA harmonic simulations and mechanical oscillation results showed that the source of the acceleration output arises from the anti-phase mode excitation due to stiffness unbalance. The anti-phase motion will appear on the TFG output as acceleration output. The results also showed that the anti-phase output depends on the ratio of in- and anti-phase modal frequencies. The larger *DR* designs had smaller anti-phase output. We proved that large frequency decoupling of in- and anti-phase modal frequencies results in decreased anti-phase displacement amplitude or acceleration output (sensitivity). The FEA simulations and experiment confirms that the frequency decoupling method can be applied to design in-plane sensing axis anti-shock TFGs. The in-plane results after normalization showed any difference on anti-phase outputs in two types of coupling schemes.

Chapter 5
Verification of frequency decoupling method in out-of-plane resonators

5.1 Overview

In this chapter, frequency decoupling method was investigated to apply the method for out-of-plane sensing axis TFGs. We have designed four types of the paired resonators: two of them are frame-coupled while the other two are spring-coupled. In each coupled type, one adopted a translational resonator while the other adopted a torsional resonator. Three different *DR* designs (*DR*=0.09, 0.13 and 0.29) in each type, were fabricated using SOG and SOI process and the anti-phase vibration amplitude against in-phase oscillation was measured.

5.2 Design of out-of-plane coupled resonators

5.2.1 Unit resonators

5.2.1.1. Translational motion type

A MEMS out-of-plane translational resonator is often designed by suspending a mass with bending beams, i.e. the stiffness of the suspension beams is smaller in the bending direction than the other directions, as shown in Fig. 5.1(a). Bending motion of a beam is shown Fig. 5.1(b). The bending stiffness is proportional to the width and cubic of the thickness as given in below equation;

$$k_z = 4Ew\left(\frac{t}{l}\right)^3 \qquad \text{---- 5.1}$$

To design the out-of-plane resonance frequency lower than other resonance frequencies such as in-plane translational frequency, the bending beam has to be designed by keeping the width larger than the thickness, because the in-plane bending stiffness of the same beam is proportional to the thickness and cubic of the width.

The in-plane stiffness of a beam is given as;

$$k_y = 4Et\left(\frac{w}{l}\right)^3 \qquad \text{---- 5.2}$$

Since the thickness of the structural layer is 20 μm in our designs, it is difficult to tune the stiffness of bending beams to set the out-of-plane resonance frequency lower than the

in-plane translational frequency. Therefore, torsional beams were used to suspend a mass for setting the translational motion, as shown in Fig. 5.2(a).

The unit resonator has four anchor points, connected to four torsion beams J2, suspending two torsion frames. The torsion frames have arms, which behave as rigid mass, connected to four torsion beams J1. Since torsion beams J1 and J2 twist in different direction and the twisting angle is designed to be same, two masses at the centre move in linear motion. The motion is shown in the schematic diagram with the arrow marks. The unit resonator was 332 µm in width and 622 µm in length. The mass-weight is 33.2 µg. Since the translational resonator has complicated spring structures, it is difficult to calculate the stiffness analytically due to its complicated structure. At first, the stiffness was estimated roughly using theoretical stiffness of the beams and then, FEA simulation was used to calculate as follows. In the FEA, a z-axis acceleration of 9.8 m/s^2 was applied. The stiffness was calculated by dividing the reaction force at the anchors of the unit resonator with the mass displacement.

5.2.1.2. Torsional motion type

The mass is oscillated in rotational motion around the torsion beam axis. The mass is suspended by a pair of torsional beams K1as shown in Fig. 5.2(b). The beams are placed at one side of the mass. Compared to the translational type, the structure is much simpler, but the mass tilts, which is not good for motion detection linearity. The unit resonator was 264 µm in width and 430 µm in length and mass weight is the same as that of the translational resonator. The stiffness (k_Φ) of the supporting beam was calculated by using the formula for a simple torsion beam (for w << t), which is given by;

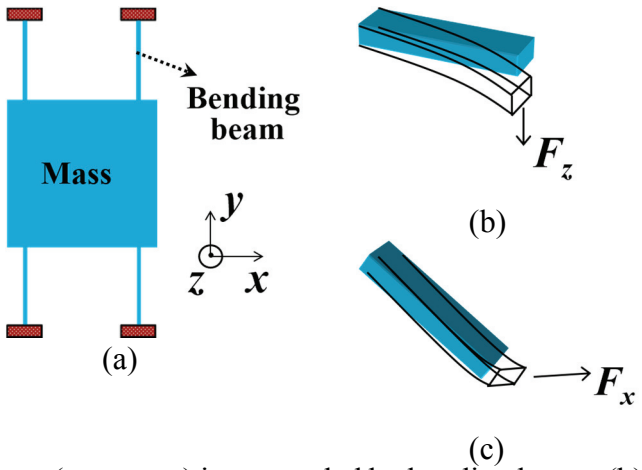

Figure 5.1 (a) A mass (resonator) is suspended by bending beams (b) out-of-plane motion and (c) in-plane (x-axis) motion of the bending beam.

$$k_\phi = \frac{1}{3l} G w^3 t \left(1 - 0.63\frac{w}{t}\right) \qquad \text{---- 5.3}$$

where t, w, and l are thickness, width, and length of the beam, respectively. *G* is the shear modulus.

5.2.2 Coupled resonators

5.2.2.1 Frame-coupled type

Two resonators are connected by a supporting frame to form a coupled resonator, as shown in Fig. 5.3. The frame is suspended by bending beams, which are anchored at the

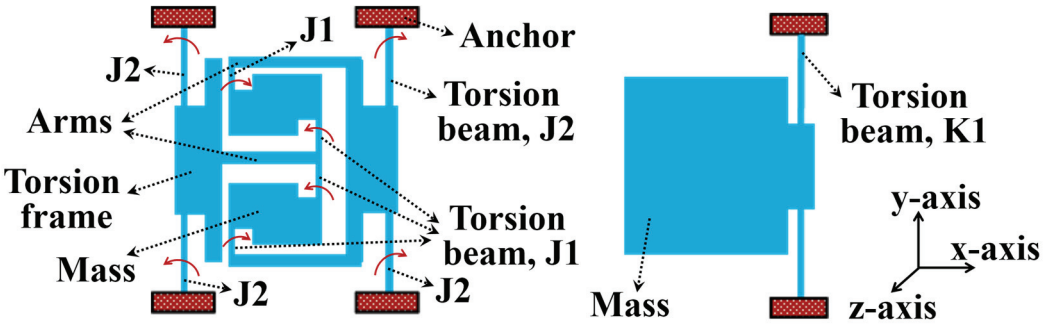

(a) (b)

Figure 5.2 Two types of out-of-plane vibrating unit resonators investigated in this work (a) translational resonator (b) torsional resonator.

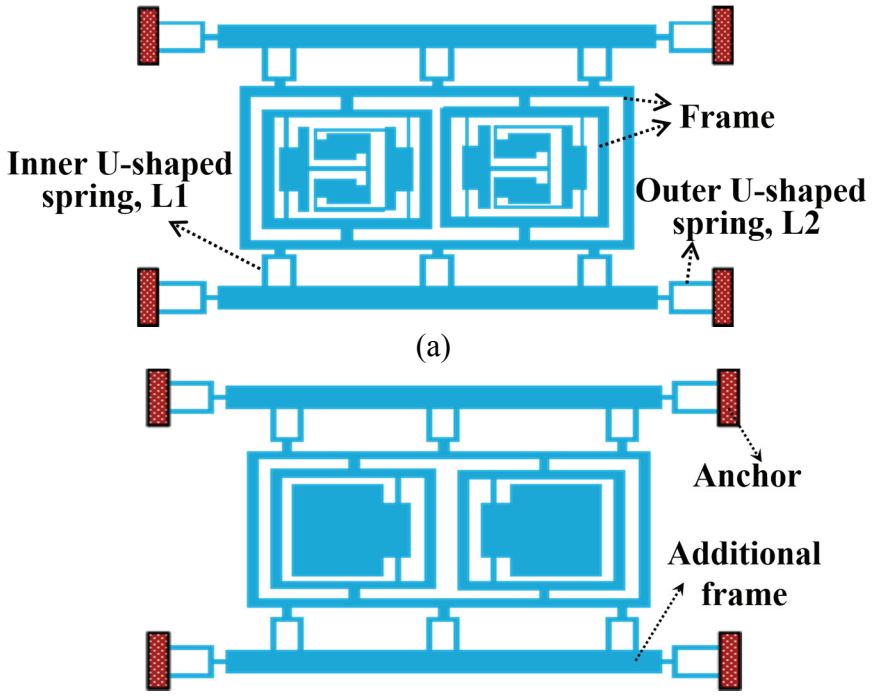

(a)

(b)

Figure 5.3 Schematics of frame-coupled resonators in which two unit resonators of same type are coupled (a) type A (translational motion resonators) (b) type B (torsional motion resonators).

substrate. The frame suspension consists of two U-shaped springs for anchoring connected to three U-shaped springs by a long beam. The frame-coupled translational motion and torsional motion designs are denoted as type A and type B, as shown in Figs. 5.3(a) and (b), respectively. The mode shapes of in- and anti-phase modes of frame-coupled designs are shown in Fig. 5.4. It is apparent that in frame-coupled designs, frame does not vibrate in anti-phase mode as shown in Figs. 5.4(b) and (d).

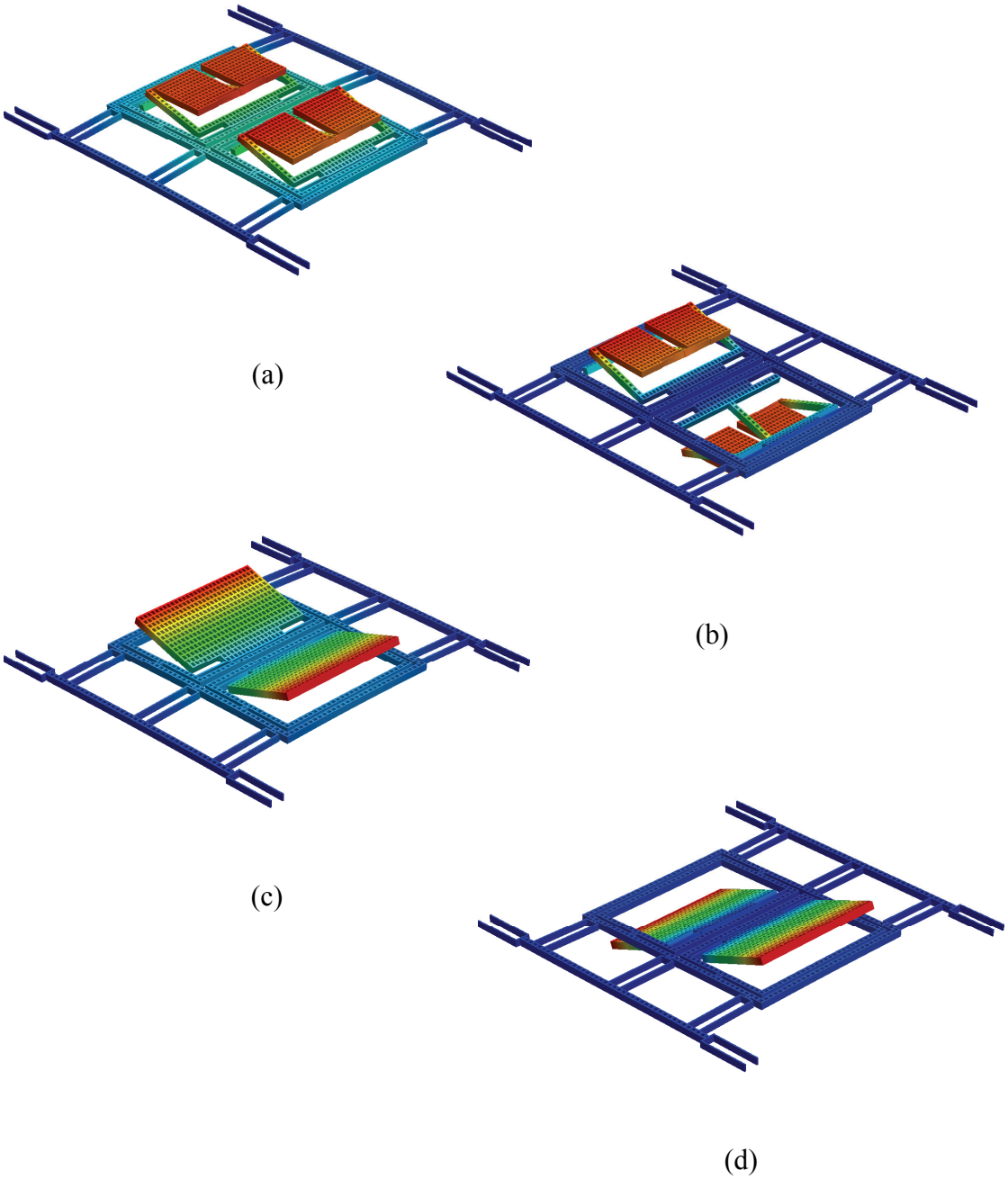

Figure 5.4 Resonant frequency modes of frame-coupled resonators (a) (c) in-phase mode, and (b) (d) anti-phase mode.

5.2.2.2 Spring-coupled type

Two translational motion resonators or two torsional motion resonators are coupled with a spring, denoted as type C and type D design, respectively. In both type C and type D designs, different types of coupling spring are used for easy design of resonant frequencies, as shown in Fig. 5.5. The mode shapes of in- and anti-phase frequencies of spring-coupled designs are shown in Fig. 5.6. In the type-C, the coupling spring consists of an I-shaped bar and torsional beams which are connected to each resonator with a beam. The function of the I-shaped bar is to set a tilt motion in the anti-phase mode, since the two beams move in opposite directions, as shown in Fig. 5.6(b). In the type-D, the coupling spring comprises torsional beams, which are connected to resonators and linked with a beam at the middle. In the anti-phase mode, the connecting beam functions as a lever cantered at the middle, as shown in Fig. 5.6(d).

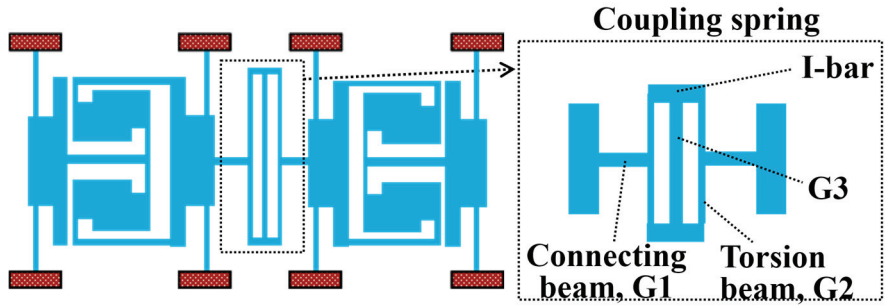

(a)

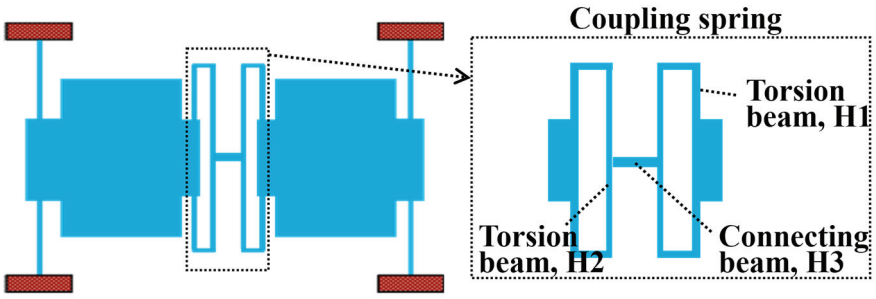

(b)

Figure 5.5 Schematics of spring-coupled resonators in which two unit resonators of same type are coupled (a) type C (translational motion resonators) (b) type D (torsional motion resonators).

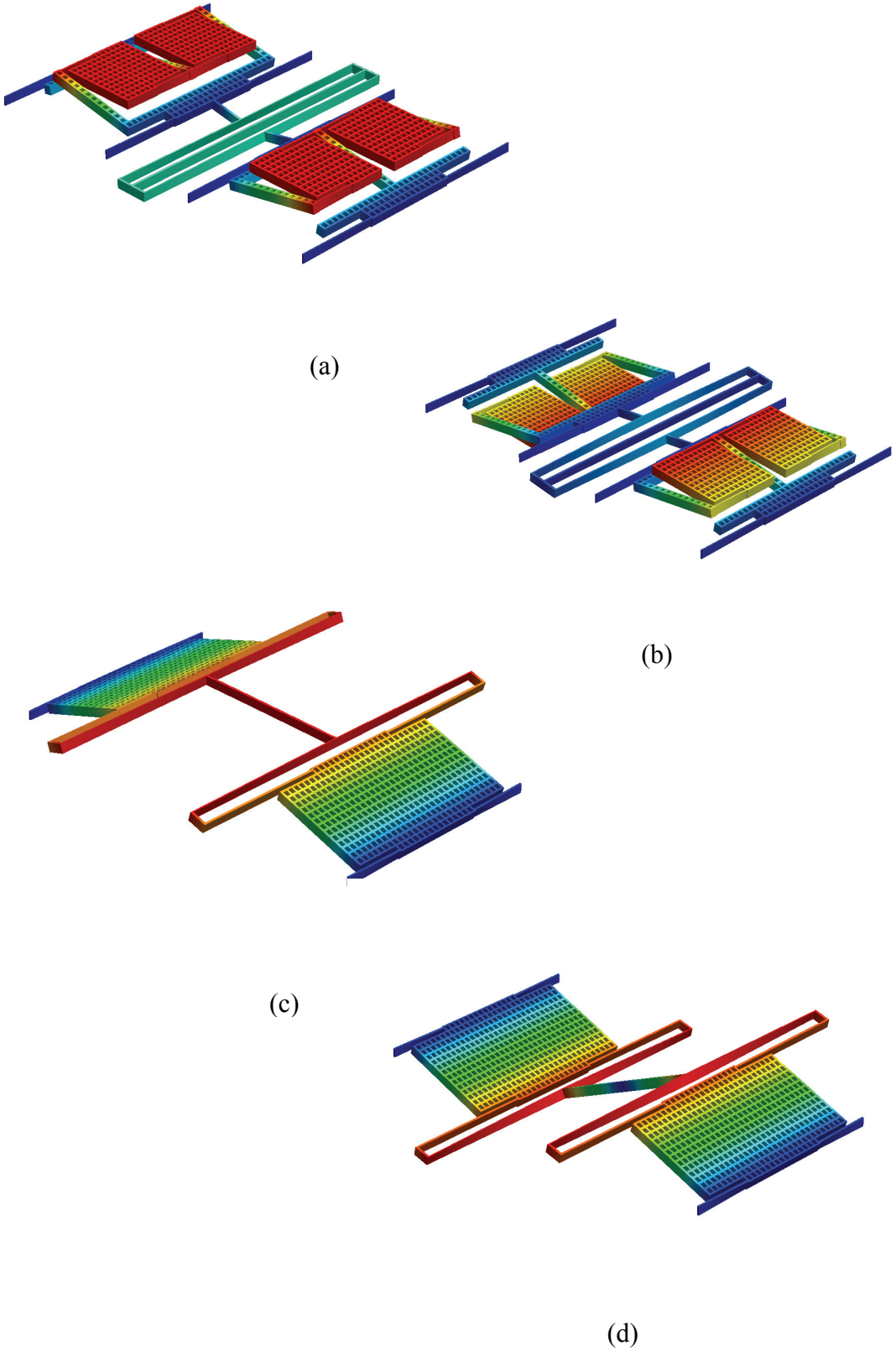

Figure 5.6 Resonant frequency modes of spring-coupled resonators (a) (c) in-phase mode, and (b) (d) anti-phase mode.

5.2.3 Design parameters

The decoupling ratios were set at 0.09, 0.13 and 0.29. To do so, the anti-phase frequency was fixed at 16.5 kHz and the in-phase frequency was varied in all types of the coupled resonators. To vary the *DR* from 0.09 to 0.29, both the unit resonator and coupling (frame and spring) suspension stiffnesses were varied in each type. The unit resonator stiffness was varied by changing the width of the beams, whereas the coupling stiffness was varied by changing the length as given in Tables 5.1 and 5.2.

Table 5.1 The FEA simulated suspension springs widths (W) and lengths (L) of frame-coupled designs.

DR	Type-A (μm)								Type-B (μm)					
	J1		J2		L1		L2		K1		L1		L2	
	W	*L*	*W*	*L*	*W*	*L*	*W*	*L*	*W*	*L*	*W*	*L*	*W*	*L*
0.09			4.25			145		185	5.05			200		165
0.13	3.2	97	4.3	116	5	200	5	210	5.12	116	5	275	5	150
0.29			4.6			325		260	5.44			325		350

Table 5.2 The FEA simulated suspension springs widths (W) and lengths (L) of spring-coupled designs.

DR	Type-C (μm)										Type-D (μm)							
	J1		J2		G1		G2		G3		K1		H1		H2		H3	
	W	*L*	*W*	*L*	*W*	*L*	*W*	*L*	*W*	*L*	*W*	*L*	*W*	*L*	*W*	*L*	W	*L*
0.09	3.7		3.55			80					5.42				5			610
0.13	3.5	97	3.55	196	6	120	3	700	5	700	5.15	150	5	306	3	842	6	390
0.29	3.2		3.25			310					4.4				3			225

5.3 Silicon-on-Glass (SOG) fabrication process

The coupled resonators were fabricated using Silicon-on-Glass (SOG) process, as shown in Fig. 5.7.

SOG process:

Step 1 (Anodic bonding): A SOI wafer used in the device fabrication, consists of a bulk-Si layer, a buried-oxide (BOX) layer and a device layer with 400 µm, 1µm and 20 µm thicknesses, respectively. In the Anodic bonding process, the device layer of SOI wafer was placed on a Pyrex Glass, and a DC voltage of 800 V was applied with positive terminal on bulk-Si and negative terminal on the Glass. The bonding process was continued for 8 min. After that, un-bonded areas appeared at the interface because of trapped air. The bonding process was completed by applying the voltage on air trapped areas.

Step 2 (Wet etching): In this step, the bulk-Si and BOX layers were removed by wet etching process. At first, the bulk-Si layer was removed by 17.2 wt% of KOH solution. The solution was prepared by mixing 125 g KOH (dry) with a 500 ml DI water. In the KOH solution, the bonded wafer was put in it for about 5hrs and 30min at temperature of 75°C. After the complete etching of the bulk-Si layer, Box layer was removed by buffered hydrofluoric acid (BHF) solution for 10 min. BHF is a mixture of ammonium fluoride (NH_4F) and hydrofluoric acid (HF).

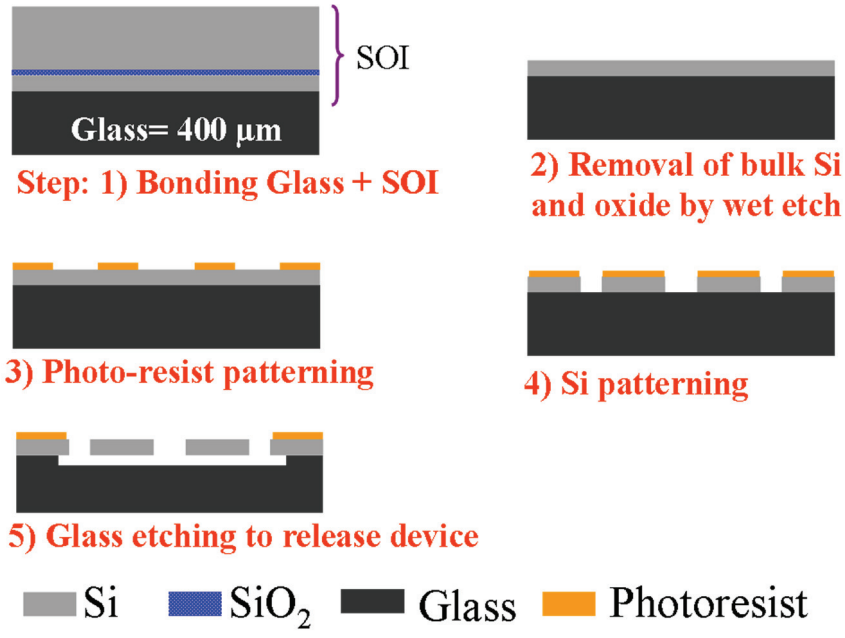

Figure 5.7 SOG fabrication process steps.

Step 3 (Resist patterning): In this step, at first HMDS was spin coated on the wafer. After that, a positive photo-resist was spin-coated on top of the HMDS. The purpose of HMDS is to have a good adhesion between the Si layer and photo-resist. The following spinning speed conditions were used.

HMDS: 500 rpm 5esc → 3000 rpm, 30 sec

Photo-resist: 500 rpm 5esc → 1500 rpm, 30 sec

The SOG wafer was put for pre-baking in the oven at 90ºC for 30 min. The wafer was exposed by UV-lithography for 5sec. And the exposed wafer is etched by NMDS solution for 2 min 30 sec to etch the exposed pattern. Then, the wafer was post-baked in the oven at 120ºC for 30 min for hardening the resist, which is acted as masking layer for the device layer etching.

Step 4 (Dry etching): For device patterning, the device layer was etched by using the Bosch process. Two gases were used; SF_6 for etching and CF_4 for forming passivation layer. Later, the photo-resist layer was removed by O_2 plasma.

Step 5 (Releasing the devices): The patterned SOG wafer was diced into chips by using diamond blade cutter and then released by etching the glass. The etch holes are useful to release the devices completely. During etching process, a concentrated HF (49%) solution was used to etch the glass and chips were dipped in the DI water for removing hazardous HF. To avoid the stiction, the devices were dried by putting in the hot ethyl-alcohol solution at 70ºC for 2 min. The devices were completely released and stiction-free.

5.4 Measurement setup and results

The measurement set-up is shown in Fig. 5.8. A stacked piezoelectric actuator is used to apply vertical mechanical oscillations on the coupled resonator. The actuator was fixed with an adhesive on a glass plate, which was placed on a printed-circuit-board (PCB) for support inside a vacuum chamber, as shown in the inset of Fig. 5.8. The ac excitation of 100 mV with 1 V dc bias was applied with a frequency sweep range from 0.003 kHz to 20 kHz. The vacuum inside the chamber was maintained at 20 Pa.

The two resonators motions were continuously scanned for measuring the frequency response using a scanning laser Doppler vibrometer (Polytec, MSA-500). In the translational resonators (type-A and -C), the displacement amplitude of the resonator at the anti-phase mode was calculated by averaging the displacements at 15 scanning points on the inner-mass, whereas in the torsional ones (type-B and -D), it was calculated by averaging the displacements of 5 scanning points at the edge of the mass.

The measured frequency responses of the frame-coupled designs (type-A and -B) are shown in Fig. 5.9. The anti-phase mode peak was appeared by in-phase oscillation which indicates that there are unbalancing in the coupled resonators. The peak anti-phase amplitude is plotted against the measured decoupling ratio in Fig. 5.10. The anti-phase amplitudes decreased with increasing *DR*. The measured resonance frequencies are given in Table 5.3. The frequencies were largely deviated from designed values and large deviations within the measurements. The large deviations in the frequencies might be the reason for the large deviations in the *DR*s. The large deviations of frequencies infer that the fabrication non-uniformity across the wafer is large, i.e., the dimensions of the suspension springs and resonator mass-weight were varied from the centre of the wafer to the edge of the wafer. The large non-uniformity in the dimensions would be caused by these following 3 reasons; (1) non-uniform exposure in lithography (2) over etching time of photo-resist by NMD (3) non-uniform etching of the side walls and notching effect during DRIE process.

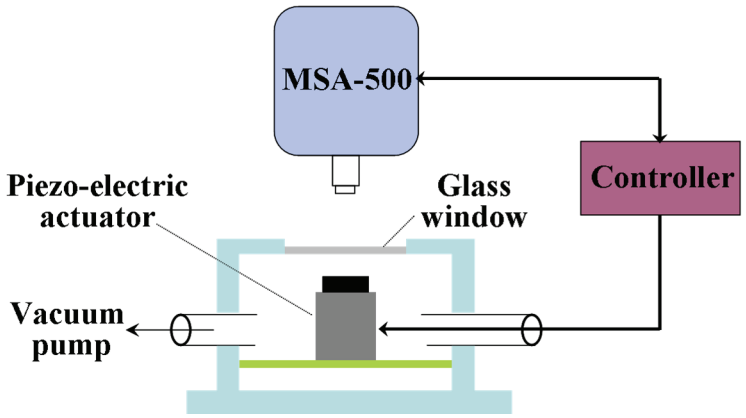

(a)

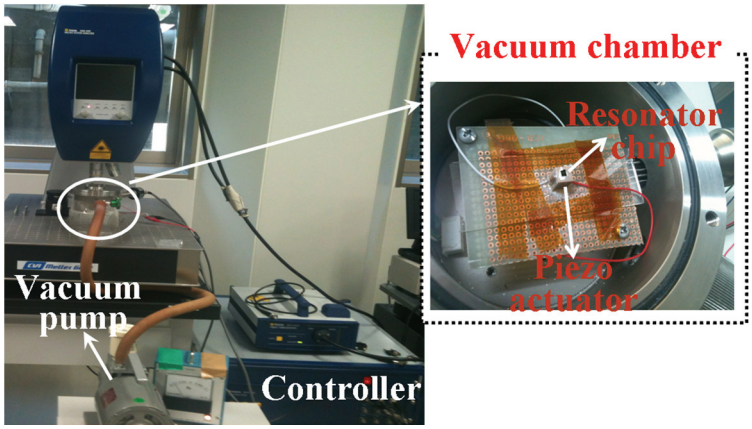

(b)

Figure 5.8 Experimental setup used for measuring the mechanical frequency response of out-of-plane resonators (a) schematic illustration (b) equipment setup.

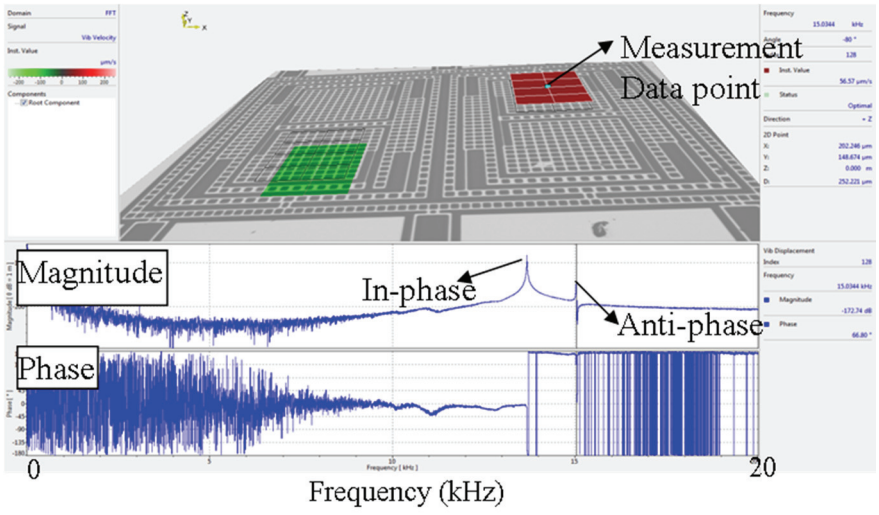

(a)

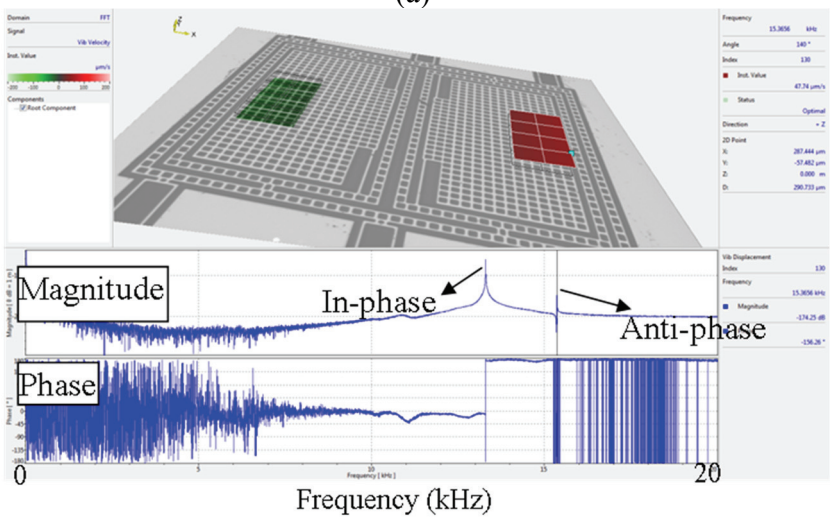

(b)

Figure 5.9 Frequency response of frame-coupled translational and torsional motion designs (a) type A (b) type B.

Table 5.3 Designed and measured frequencies of SOG chips.

		Designed *DR*	Designed freq.		Measured *DR*	Measured frequencies	
			f_{in}	f_{anti}		f_{in}	f_{anti}
Translational	A	0.09	15.1	16.5	0.06-0.09	12.54-13.85	13.58-15.25
		0.13	14.4	16.5	0.1-0.14	11.70-13.12	13.11-15.25
		0.29	11.8	16.5	0.24-0.27	10.43-11.16	13.85-15.72
	C	0.09	15.1	16.5	0.08-0.09	12.36-12.91	13.36-14.13
		0.13	14.4	16.5	0.12-0.14	11.36-12.97	13.02-14.90
		0.29	11.8	16.5	0.29	8.50	11.99
Torsional	B	0.09	15.1	16.5	0.07-0.08	13.40-14.01	14.66-15.05
		0.13	14.4	16.5	0.12-0.14	12.80-13.38	14.72-15.36
		0.29	11.8	16.5	0.27-0.29	10.86-11.22	14.91-15.77
	D	0.09	15.1	16.5	0.06-0.08	13.46-14.69	14.40-15.99
		0.13	14.4	16.5	0.09-0.11	12.80-13.70	14.16-15.35
		0.29	11.8	16.5	0.21-0.27	10.28-11.35	13.11-15.08

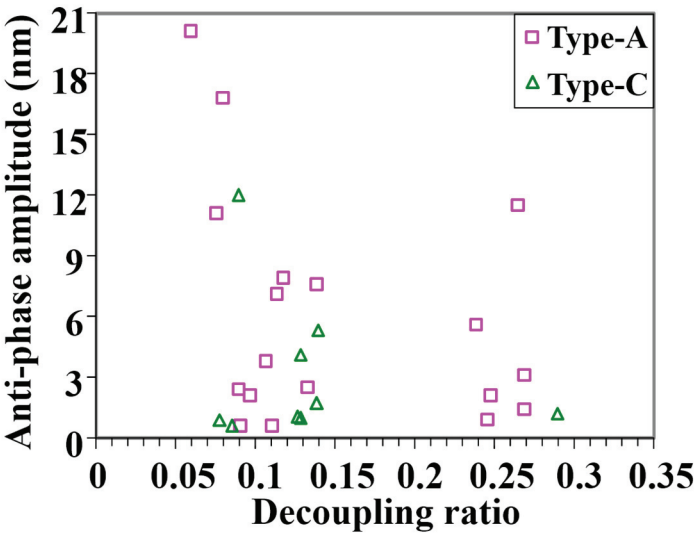

(a)

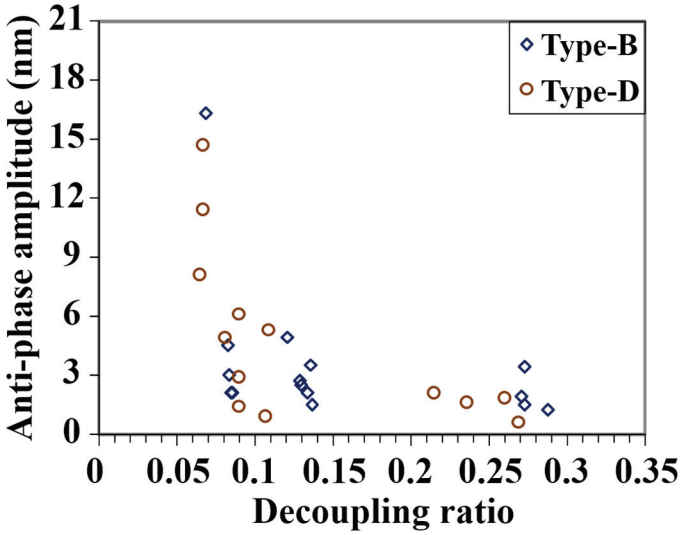

(b)

Figure 5.10 Anti-phase amplitudes of SOG chips against measured decoupling ratio (a) translational designs (b) torsional designs.

5.5 Discussion on SOG chips results

The measured frequency responses showed that the resonators vibrated in anti-phase mode against the applied in-phase oscillation. These results agree with the previous results on in-plane resonators (chapters 4), wherein the perfectly symmetrical coupled resonators did not vibrate in anti-phase mode in FEA simulations, and fabricated resonators were vibrated in anti-phase mode against the applied in-phase oscillation. As shown in Fig. 5.10, the larger *DR* resonators showed the smaller anti-phase amplitudes. It also agrees with the in-plane resonators result of FEA and measurements. We deduced that the acceleration sensitivity in out-of-plane resonators also arises from excitation of anti-phase mode due to the stiffness unbalance between two unit resonators. The frequency decoupling method, which is "sense in-phase mode frequency should be separated as far as possible from anti-phase frequency", would be also effective to suppress the anti-phase amplitude and acceleration output in *x*-axis TFGs.

It is difficult to compare the anti-phase amplitude between the frame- and spring-coupling designs for better coupling types, and between the translational motion and torsional motion designs for better motion types, since the measurements showed large frequency deviations, *DR* deviations and designs had different suspension spring dimensions. So, in order to have a fair comparison, the measured results are normalized to designed frequencies, *DR* and calculated stiffness unbalances with the Eq. 4.14.

$$z_{\text{normalized}} = z_{\text{measured}} \frac{DR_{\text{measured.}}}{DR_{\text{design}}} \frac{(f_{\text{anti}}^3)_{\text{measured}}}{(f_{\text{anti}}^3)_{\text{designed}}} \frac{(f_{\text{in}} + f_{\text{anti}})_{\text{measured}}}{(f_{\text{in}} + f_{\text{anti}})_{\text{designed}}} \frac{(\Delta k_{15\text{nm}})_{\text{spring-coupled.}}}{\Delta k_{15\text{nm}}} \quad \text{--5.4}$$

The stiffness unbalance (Δk) was calculated by assuming a constant dimension difference of 15 nm in resonator suspension beam width. The stiffness unbalance was calculated as described in Sections 5.2 for translational designs. In the FEA, a z-axis acceleration of 9.8 m/s^2 was applied. The stiffness was calculated by dividing the reaction force at the anchors of the unit resonator with the mass displacement. The Δk becomes stiffness difference between the resonator as designed and resonator with 15 nm decrease in suspension beam width. The Δk for torsional designs was calculated by using the Eq. 5.3, as given in the Table 5.4. The spring-coupled resonators had narrower beam than frame-coupled resonators when we are designing resonators with the same anti-phase resonant frequency. Since the torsional stiffness is proportional to cubic of width, the stiffness unbalance of the spring-coupled designs is smaller than that in frame-coupled designs for a same fabrication error. The measured results are normalized and plotted in the Fig. 5.11.

Table 5.4 Calculated stiffness unbalances for 15 nm fabrication error.

DR	Translational		Torsional	
	Type A Δk (N/m)	Type C Δk (N/m)	Type B Δk (nN-m)	Type D Δk (nN-m)
0.09	0.367	0.305	2.982	2.61
0.13	0.389	0.278	3.305	2.38
0.29	0.395	0.243	3.396	1.77

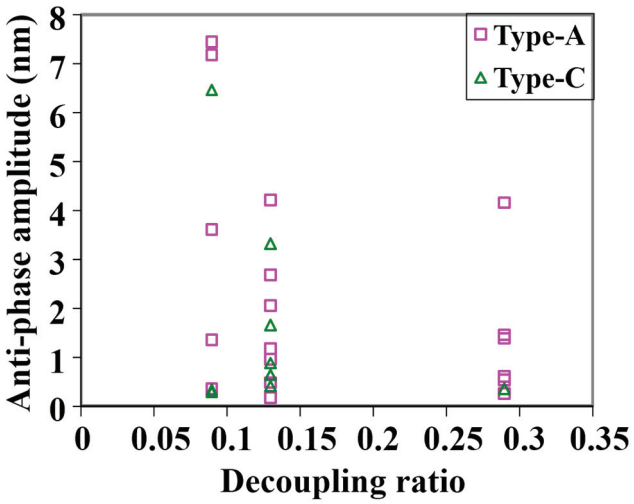

(a)

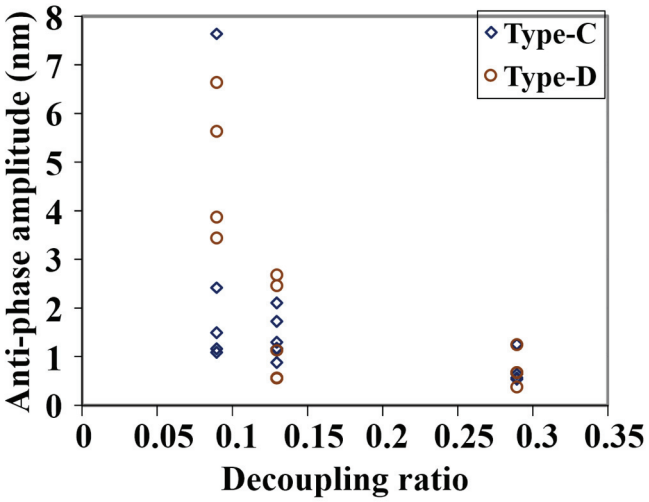

(b)

Figure 5.11 Normalized anti-phase amplitudes of (a) translation designs (b) torsional designs.

In the normalization with stiffness unbalance, spring-coupled designs are considered as reference. The normalized anti-phase amplitudes of the four types are generally same similar to in-plane coupled resonators in Chapter 4. After normalization, the anti-phase amplitude values are still distributed in the same design. In the normalization, we assumed a constant dimension difference which is ideal. However, in the actual microfabrication, the scatterings in the chip-level non-uniformity is unavoidable. The Δk values would be the average errors among the chips, therefore the smaller *DR* resonator has larger distributions.

After the normalization, there is no clear understanding on the effects of of motion and coupling on the anti-phase amplitude. The reason might be the frame-coupled and spring-coupled designs are not having same resonator facing direction and different location of resonator suspension beams as shown in Fig. 5.12. In the type-A, resonators are having same facing direction whereas in type-C, resonators are placed with opposite face directions. In the type-B, the resonator suspension beams location is opposite to the type-D designs. Therefore, these resonators have to be modified to have the same facing direction and resonator suspension spring location, and fabricated with better conditions to verify the effect of coupling type and motions type on acceleration output. We designed advanced coupled resonators (symmetric) and fabricated them with better conditions. To minimize the fabrication non-uniformity, the advanced coupled resonators were fabricated on SOI wafer by using projection mask lithography for uniformly exposing the photo-resist on the entire wafer and by controlling the silicon sidewalls with small scalloping with uniform cross-section and the notching effect in dry etching.

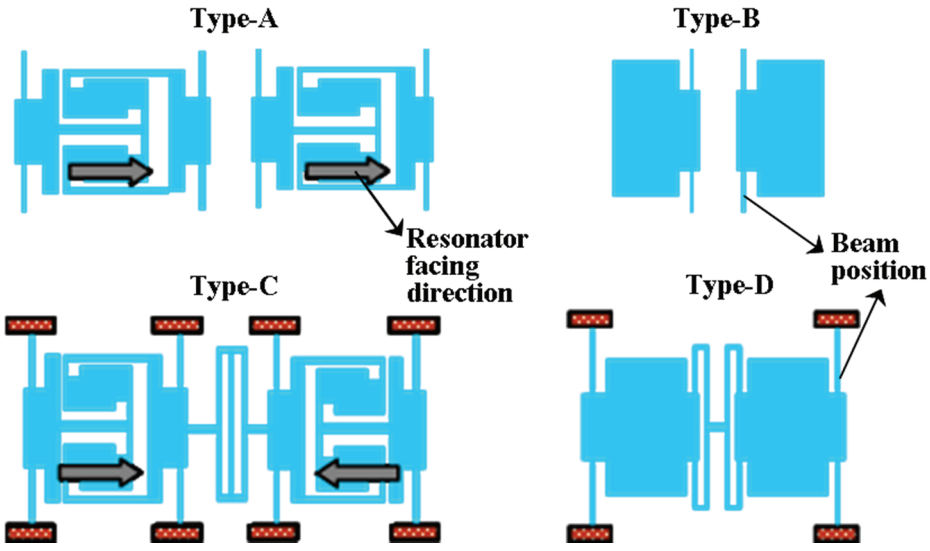

Figure 5.12 Previously designed coupled resonators facing direction and suspension beams location.

5.6 Design of advanced coupled resonators

The type-A design is modified with resonator facing direction, named as type-A1, shown in Fig. 5.13(a), and type-D design is modified with the suspension beam location, named as type-D1, shown in Fig. 5.13(b).

5.6.1 Design parameters

We selected the type-A1, type-B, type-C and type-D1 designs with three decoupling ratios of 0.09, 0.13 and 0.29. In all types, the anti-phase frequency was fixed at 16.5 kHz and the in-phase frequency was varied, same as SOG designs. In type-A1 designs, resonator and coupling suspension spring dimensions were kept same as the type-A design. But, to set the DR in the type-D1 designs, resonator suspension torsional beams width and coupling suspension torsional beams and middle beam lengths were varied, as given in Table 5.5. The mode shapes of type-A1 and -D1 designs are shown in Figs. 5.14 and 5.15, respectively. In type-D1, the function of the middle beam is same as type-D design. These designed coupled resonators were fabricated with the standard SOI fabrication process.

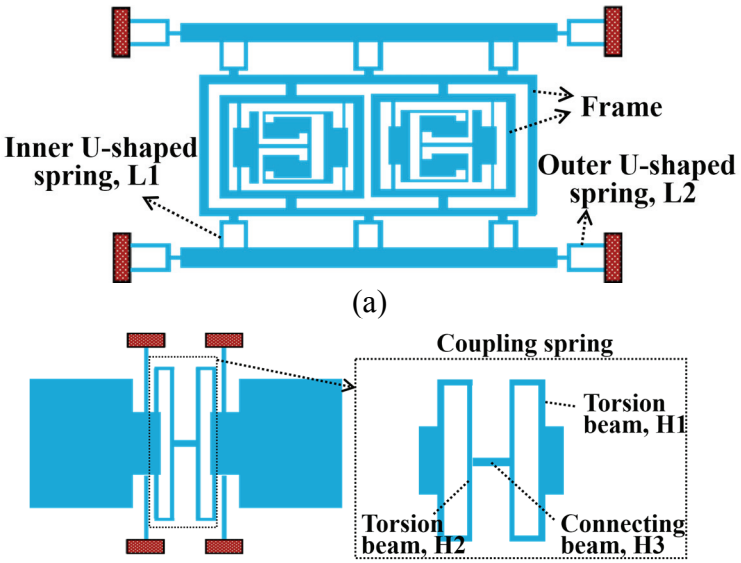

Figure 5.13 Schematics of coupled resonators with symmetric in resonator facing direction and spring location (a) type-A1 (b) type-D1.

Table 5.5 Suspension spring dimensions of type-D1.

DR	K1		H1		H2		H3	
	W	L	W	L	W	L	W	L
0.09	4.3			185		600		150
0.13	4.12	150	5	185	4	600	6	90
0.29	3.08			110		450		60

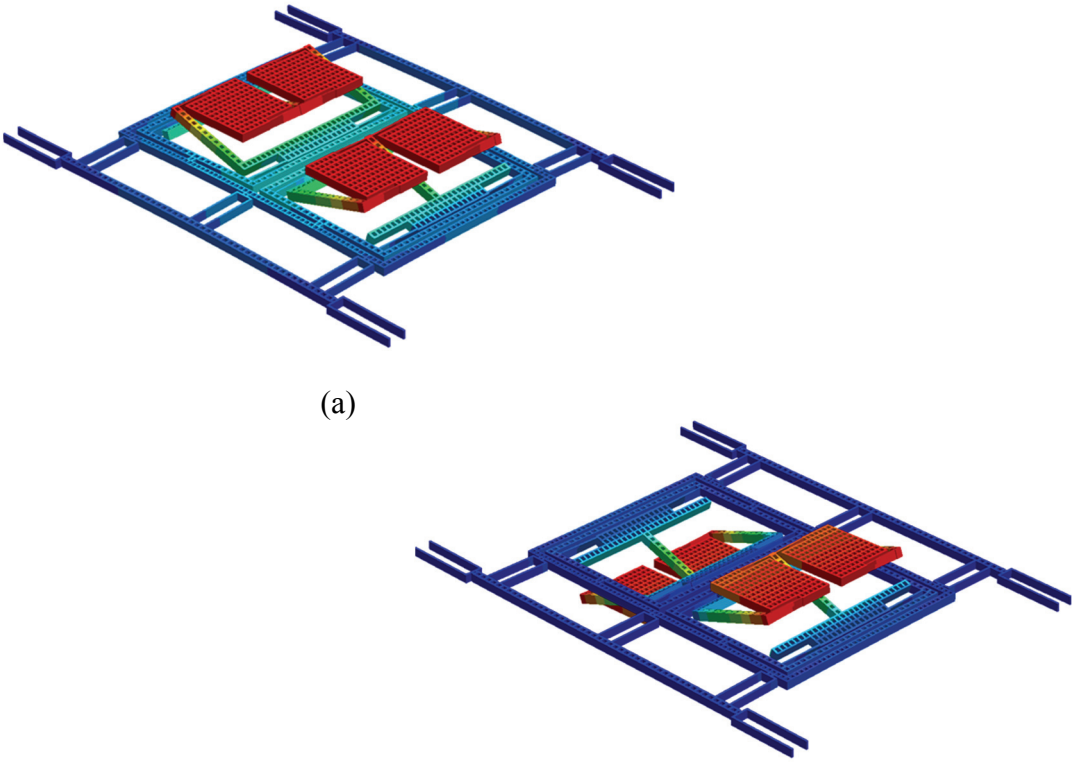

(a)

(b)

Figure 5.14 Resonant frequency modes of frame-coupled translational resonator (type A1) (a) in-phase mode (b) anti-phase mode.

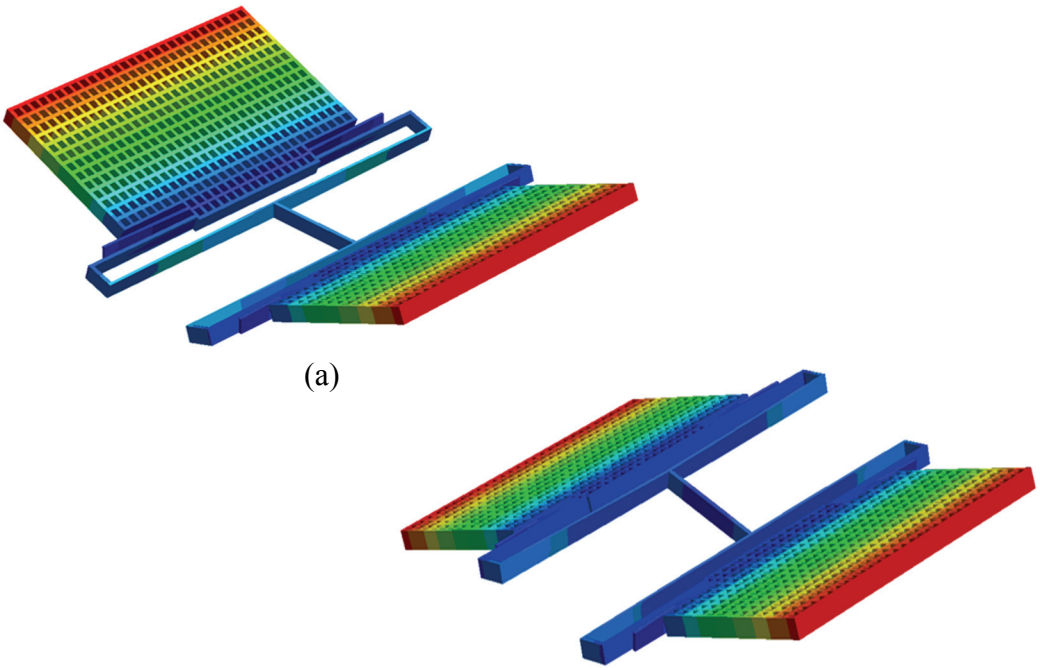

(a)

(b)

Figure 5.15 Resonant frequency mode of spring-coupled torsional resonator (type D1) (a) in-phase mode (b) anti-phase mode.

5.7 SOI fabrication process

The coupled resonators were fabricated on silicon-on-insulator (SOI) wafer of a 20 µm thickness in device layer. The fabrication process is shown in Fig. 5.16. The structures were patterned using DRIE. The patterned structures were released by hydrofluoric acid vapor phase etching and diced into chips using laser dicing.

SOI process:

Step 1 (Native oxide removal): The SOI wafer used in the fabrication consists of a device layer, a BOX layer, and a handle layer with thicknesses 20, 3 and 600 µm, respectively. At first the wafer was cleaned with the Piranha solution and then with the BHF to remove the native oxide on the device layer.

Step 2 (Resist application): Photo-resist was used for masking during etching device layer. At first, HMDS was spin-coated with same conditions same as in the case of SOG process. After that, THMR-iP 1800EP photo-resist (positive) was spin-coated. The thickness of the photo-resist was about 1µm. After applying the photo-resist, the wafer was pre-baked at 90 ºC for 30 min on the hot-plate.

Step 3 (Projection mask lithography): The wafer was exposed by using i-Line stepper machine. In this step, a reticle (a photo mask), which was designed with 5 times of the actual size of coupled resonators, is projected on the surface of the wafer. During the projection, the dimensions were reduced by one-fifth. The actual size of all designs is arranged in 10.4 × 10.5 mm^2 area. So, this much area is repeatedly exposed as step by step across the surface of the wafer, as shown in inset Fig. 5.16(b). The wafers were developed in TMAH 2.38% solution for creating a photo-resist mask. Then, the wafers were post-baked at 120ºC for 30 min on the hot-plate.

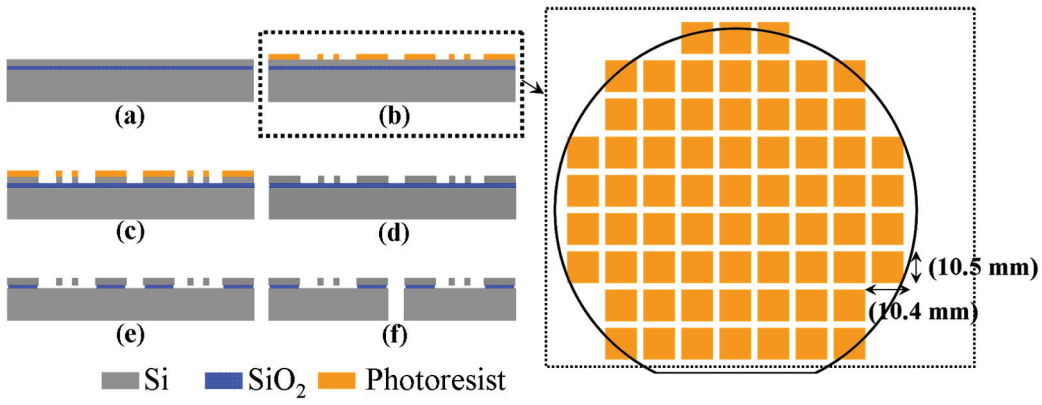

Figure 5.16 SOI fabrication process steps (a) a bare SOI wafer (b) lithography (c) structural Si layer etching (d) resist ashing (e) releasing of the devices (f) dicing.

Step 4 (Dry etching):

The resist-patterned wafers were etched using Bosch process (DRIE) as shown in Fig. 5.16(c). SF_6 gas and C_4F_8 gas were used for etching and for forming a passivation layer, respectively. In one cycle, at first the passivation layer is formed; secondly, the bottom passivation film is etched for 2 sec, and finally, the bottom silicon layer and side wall filled with passivation is etched. The process continues until the number of cycles set in the program. We continued the Bosch process for 17 µm depth. After that, to minimize the notch at the bottom of the device layer, we used pulsed etching with low frequency (400 kHz). The cross section of a dummy sample is shown in Fig. 5.17. The notch appeared at the bottom (interface of device layer and BOX layer) was small and scalloping effect at side wall was appeared small.

Bosch process: Bias=55w, 13.56 MHz

time= 2-3sec (ramp), count=50cycles

Pulse etching: Bias=80w, 400 kHz

time= 3sec, count=40cycles, duty cycle 25%

We finally used these conditions to etch the actual wafers. Since the above mentioned conditions for a sample piece, we used pulse etching for more time to reach the BOX layer in the actual wafer with 6-inch wafer. The pulse etching of two full wafers was increased by 5 cycles and 15 cycles, respectively. The photo-resist was ashed by using oxygen (O_2) dry etching.

Step 5 (Releasing):

The devices were released by etching the BOX layer with HF vapour for 2.5 hr. The devices were diced using laser dicing. The SEM images of fabricated type-A1,-B,-C,-D1 devices are shown in Fig. 5.18. The fabricated devices were completely released and the measured under cutting length at the anchor was 6.3 µm (42 nm/min). The undercut was happened because of over etching.

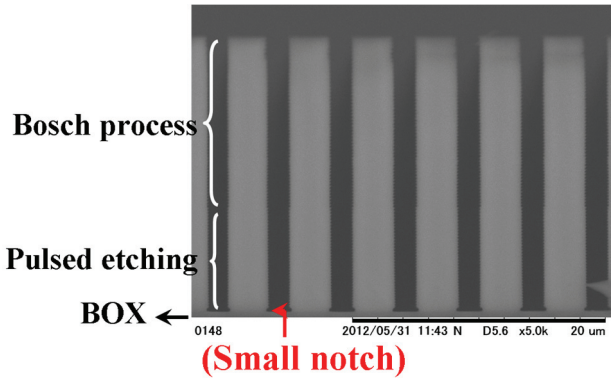

Figure 5.17 Cross-section of SOI sample with small notch.

At first we used an etch rate calculated for a simple oxide etching on the whole wafer 28 nm/min. We used this etch-rate to etch the BOX layer and completely release the devices for 4 μm (from the edge of etch hole). So, we continued the etching for longer time.

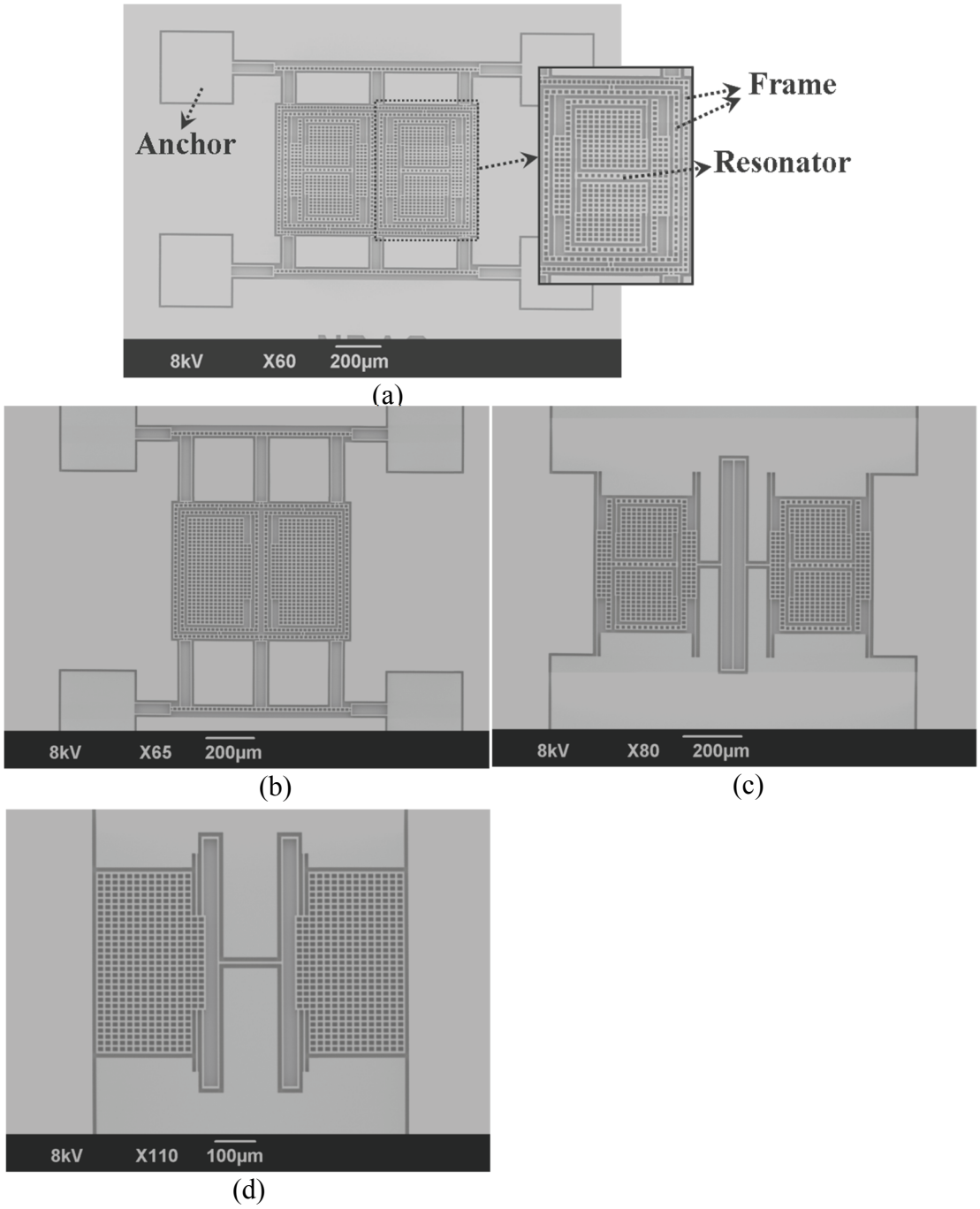

Figure 5.18 SEM images of fabricated SOI chips (a) type A1 (b) type B (c) type C (d) type D1.

5.8 Measurement results of SOI chips

We used the same measurement set-up, which is used for SOG chips evaluation. The measured frequency responses of the translational designs of frame-coupled (type-A1) and spring-coupled (type-C) with DR of 0.09 are shown in Figs. 5.19 and 5.20, respectively.

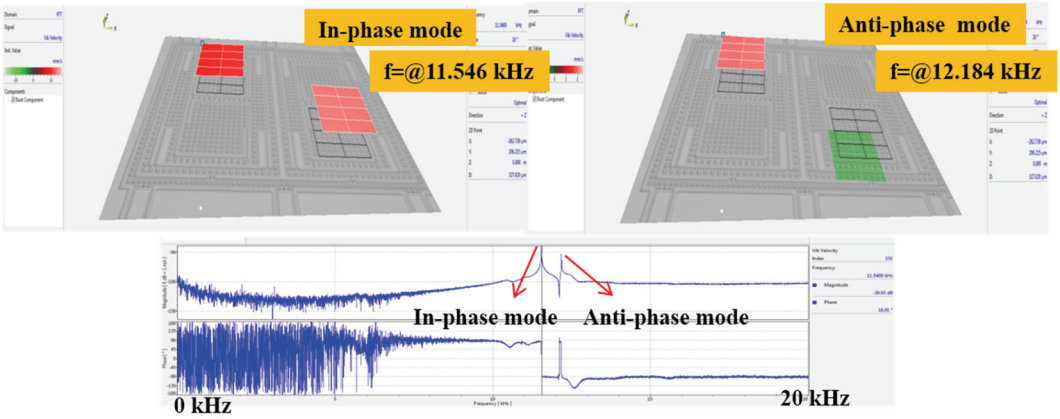

(a)

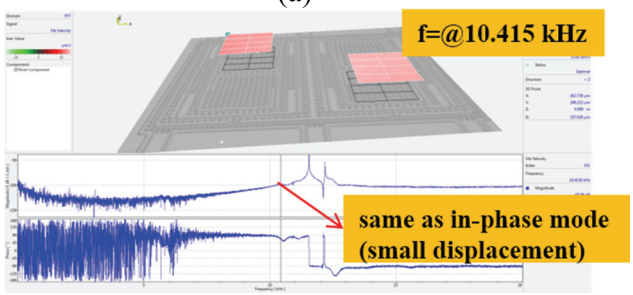

(b)

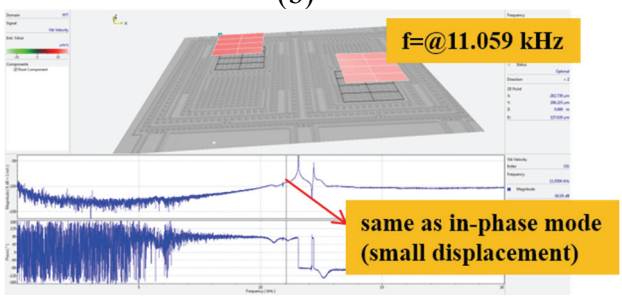

(c)

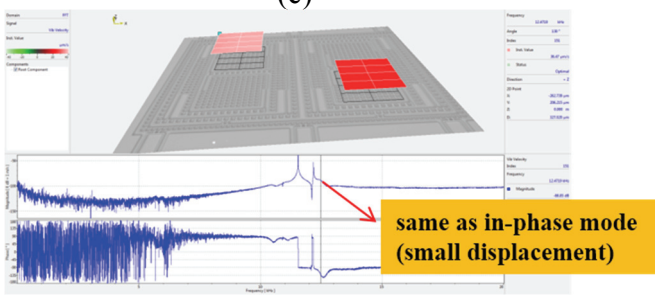

(d)

Figure 5.19 Frequency response of type-A1 design (a) in- and anti-phase modes (b) (c) (d) small in-phase modes.

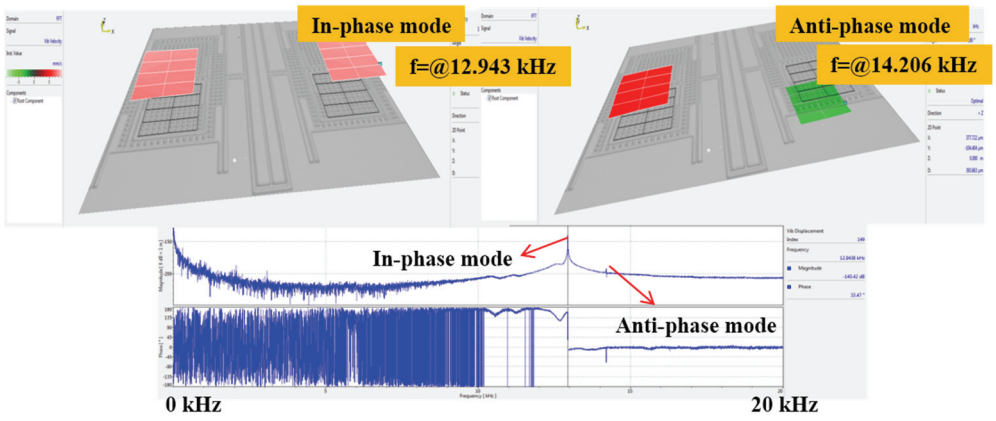

(a)

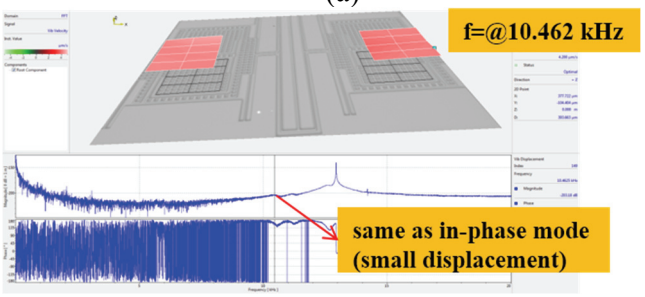

(b)

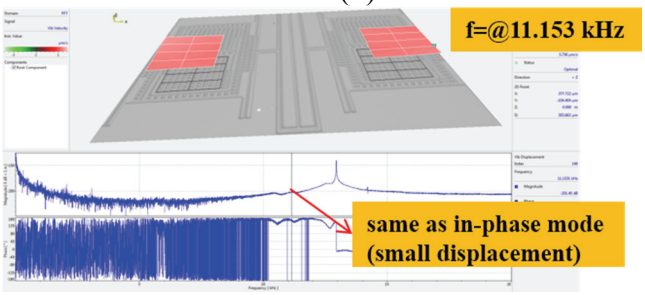

(c)

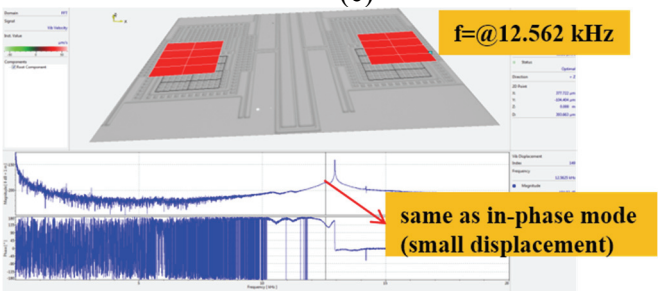

(d)

Figure 5.20 Frequency response of type-C design (a) in- and anti-phase modes (b) (c) (d) small in-phase modes.

In type-A1 and type-C designs frequency responses, there were two major resonance peaks. The motions at those frequencies are same as in-phase and anti-phase resonance modes. For example, in the type-A1 design, the in-phase and anti-phase resonance frequencies were at 11.546 and 12.184 kHz, respectively. Apart from the designed resonance frequencies, there was several small amplitude resonance peaks appeared on the frequency response. The motions at those resonance frequencies are same as in-phase motion. The small amplitude peaks were at 10.451, 11.059, and 12.471 kHz. In the case of type-C design frequency response, the in- and anti-phase resonance modes were at 12.943 and 14.206 kHz, respectively and small amplitude peaks (as in-phase motion) appeared at 10.462, 11.153 and 12.562 kHz. The small amplitude resonance frequencies are nearly the same in both designs. We analyzed the reasons for the unintended peaks.

At first, we thought that the PCB, which is used as support, may cause the small peaks i.e. the PCB resonance frequencies were probably appeared on the frequency response. To verify this, we used a metal plate as support for the piezo actuator as shown in Fig. 5.21. The newly evaluated frequency response is shown in Fig. 5.22. It is noted that the frequency response show no small amplitude peaks at those frequencies of previously evaluated with PCB as support. This result infers that PCB caused the small peaks on the main resonator frequency response. To eliminate the PCB effect on the anti-phase amplitude, we considered the chips which are having anti-phase frequencies higher than the ~12.6 kHz (maximum frequency of small peaks). The frequency range of small peaks and the main in-phase and anti-phase resonance modes of all types are plotted in Fig. 5.23. Few chips showed anti-phase resonance frequency smaller than small peaks frequency range. The in-phase and anti-phase frequencies of translational (type-A1 and -C) and torsional (type-B and -D1) designs are given in Tables 5.6 and 5.7, respectively.

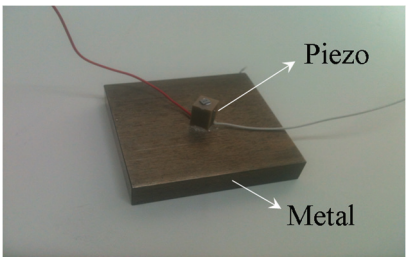

Figure 5.21 Piezo stacked on a metal block.

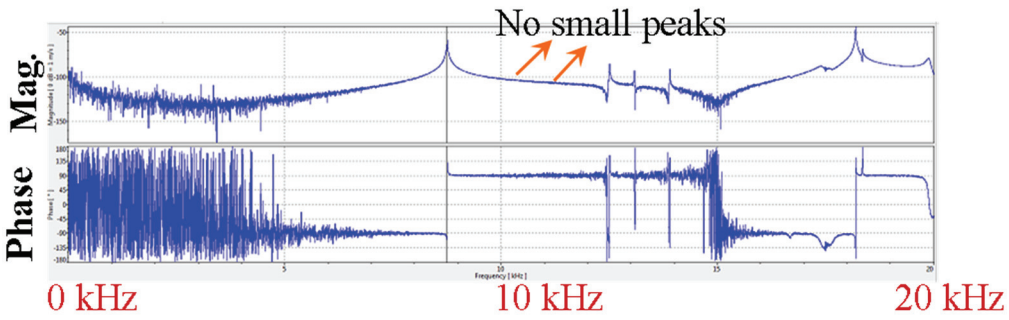

Figure 5.22 Measured frequency response by using piezo on metal block.

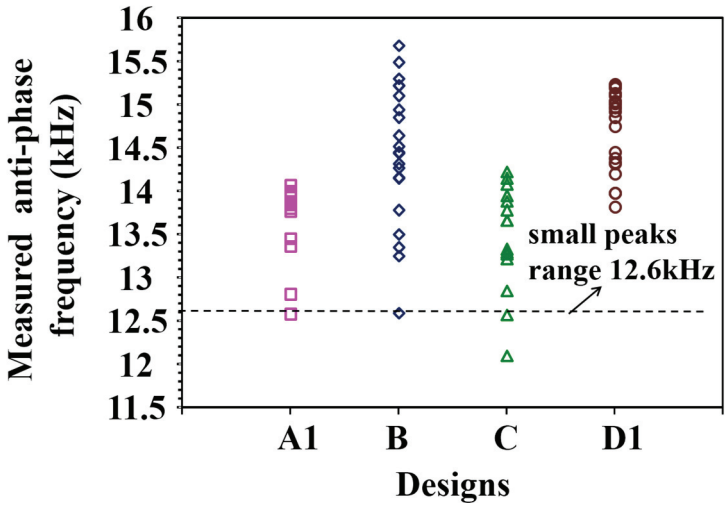

Figure 5.23 Frequency distributions of small in-phase peaks and in-phase and anti-phase resonance modes.

Table 5.6 Designed and measured frequencies of translational motion designs (type-A1 and type-C).

Designs	DR	Designed frequency (kHz)		Measured frequency response (kHz)		Measured DR
		fs_{in}	fs_{anti}	fs_{in}	fs_{anti}	
Type-A1	0.09	14.9	16.45	12.14-13.06	12.79-13.78	0.05
	0.13	14.42	16.60	12.43-12.66	13.85-14.05	0.10-0.11
	0.29	11.83	16.55	10.50-10.91	13.43-13.86	0.22-0.24
Type-C	0.09	15.05	16.53	12.62-12.94	13.86-14.20	0.09
	0.13	14.24	16.57	11.34-12.11	13.25-14.13	0.14
	0.29	11.79	16.48	9.02-9.62	12.83-13.64	0.29-0.3

Table 5.7 Designed and measured frequencies of torsional motion designs (type-B and type-D1).

Designs	DR	Designed Frequency (kHz)		Measured frequency response (kHz)		Measured DR
		fs_{in}	fs_{anti}	fs_{in}	fs_{anti}	
Type-B	0.09	15.05	16.53	12.42-14.06	13.23-15.2	0.058-0.09
	0.13	14.3	16.43	12.64-12.83	14.13-14.5	0.1-0.11
	0.29	11.91	16.68	11.21-11.58	14.62-15.66	0.233-0.26
Type-D1	0.09	15.03	16.58	12.45-13.77	13.8-15.21	0.09-0.097
	0.13	14.37	16.52	12.65-13.09	14.73-15.2	0.138-0.14
	0.29	11.85	16.56	10.04-10.24	14.83-15.02	0.32

The peak anti-phase amplitude is plotted against the measured decoupling ratio (*DR*) in Fig. 5.24. The anti-phase amplitudes of SOI fabricated chips are smaller than the SOG fabricated chips. It indicates that the fabrication error was improved in the SOI process. From the Fig. 5.24, the anti-phase amplitudes decreased with increase in *DR*. The SOI out-of-plane resonators also proved the frequency decoupling method. The frame-coupled resonators (type-A1 and -B) showed higher anti-phase amplitudes than the spring-coupled resonators. The type-A1 and -C of the translational resonators showed relatively higher anti-phase amplitudes compared to type-B and -D1 of the torsional resonators.

The measured resonant modes were deviated from the design, which causes the deviation of *DR*. The deviations in frequencies of SOI chips are smaller than the SOG fabricated chips. For example, the measured anti-phase mode f_{anti} in type-A of *DR*=0.13 ranged from 13.91 kHz to 14.05 kHz and that in type- C of same DR ranged from 13.25 kHz to 14.13 kHz, whereas the f_{anti} of all types were designed at 16.5 kHz. The translational motion resonators showed lower resonant frequencies than the torsional ones, but there were small difference between the coupling types.

The *DR* deviation which is the averaged difference of the measurement from the design is represented with arrows in the Fig. 5.24. The DR deviation is larger in frame-coupled resonators than the spring-coupled resonators.

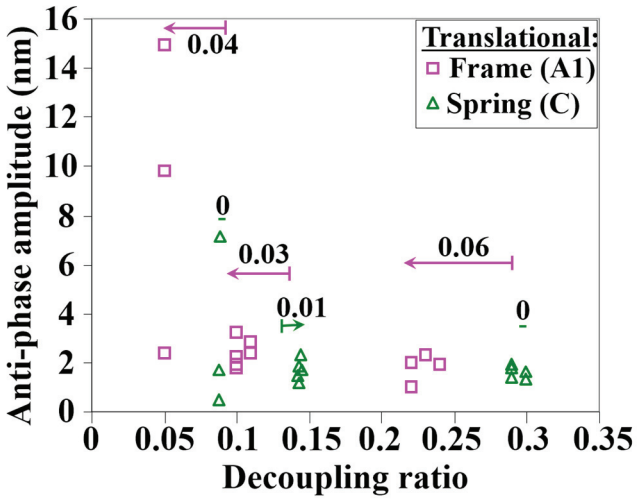

(a)

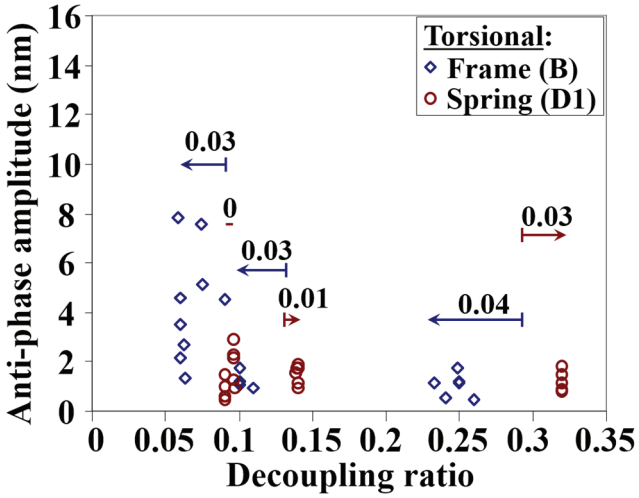

(b)

Figure 5.24 Anti-phase amplitudes against measured decoupling ratio in (a) translational motion (b) torsional motion designs.

5.9 Discussion on SOI chips results

5.9.1 Effect of design parameters

The measurement results in Fig. 5.24 showed that the anti-phase amplitude decreased by increasing the decoupling ratio. The measured results showed large frequency deviations and DR deviations. So, it is difficult to verify the effect of coupling types and motions types on anti-phase or acceleration output.

The distributions are mainly caused by the two types of fabrication errors, one is the scattering (deviation) in dimensions between the chips and the other is scattering in dimension difference in a chip. The dimension variation between chips causes the deviation in the measured resonant frequencies and DR as reported in Tables 5.6 and 5.7. We observed a large non-uniformity in the fabricated wafer, ranged 175 nm to 325 nm from the FEA simulations on type C design.

There is a relatively small dimension difference in a chip, which may cause tiny unbalancing of the resonator properties. This unbalancing in device dimensions should be same in all designs. However, the effect on the stiffness unbalance Δk is different, since the original beam width and the deformation mode are different. We estimated the Δk by assuming a constant dimension difference of 15 nm in resonator suspension beams width. The stiffness unbalance is calculated as described in Sections 5.2 for translational designs and by using Eq. 5.3 for torsional designs given in the Table 5.8. Using the measured resonant frequencies and the estimated stiffness unbalance, the measured anti-phase amplitude is normalized by using Eq. 5.4.

Each point is plotted to the designed *DR* value, frequency and Δk of the type C (spring-coupled) for translational designs (A1, C) and type D1 (spring-coupled) for torsional designs (B, D1) and plotted in Fig. 5.25. The normalized anti-phase amplitudes of the four types are generally same similar to SOG chips. After normalization, the anti-phase amplitude values are still distributed in the same design same as in SOG chips since the assumed a constant dimension difference which is ideal.

To compare the results in Figs. 5.25, we plotted the anti-phase amplitude of three decoupling ratio TFGs in section 3.3 of Chapter 3 against 1-g in Fig. 5.25(a). The anti-phase amplitude of TFG reduced to 28% by increasing the decoupling ratio from 0.09 to 0.29, whereas in type-C spring-coupled resonators it is reduced to 51%. The difference in reduction between the measurement and simulation is due to distribution.

Table 5.8 Calculated stiffness unbalances for 15 nm fabrication error.

DR	Translational		Torsional	
	Type A1 Δk (N/m)	Type C Δk (N/m)	Type B Δk (nN-m)	Type D1 Δk (nN-m)
0.09	0.367	0.305	2.982	1.73
0.13	0.389	0.278	3.305	1.624
0.29	0.395	0.243	3.396	0.951

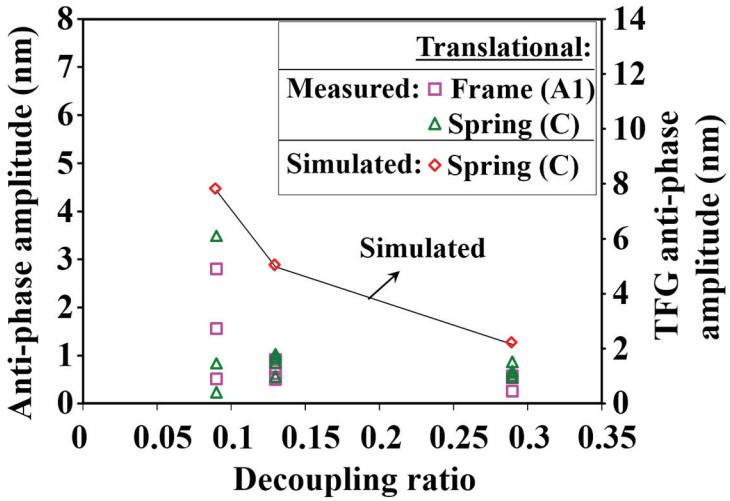

(a)

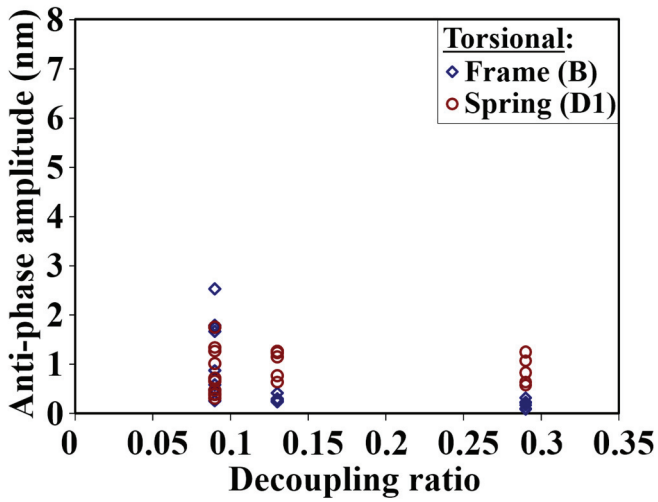

(b)

Figure 5.25 Normalized anti-phase amplitudes of (a) translational designs (b) torsional designs.

5.10 Resonator designs

There is no significant difference among resonators design after normalization in both in-plane coupled resonators and out-of-plane resonators. However, in the measurement, there are some differences. From that we obtained the designing guidelines for the coupled-resonators used in TFG.

In the out-of-plane coupled resonators, from the measured results shown in the Fig. 5.24, *DR* deviation is large in frame-coupled resonators and the *DR* values are smaller compared to spring-coupled ones. The difference would be caused by the different deformation modes of the beams. In frame-coupled designs, all of the beams deform in torsional mode except for the frame suspension beams, which deforms in a bending mode. Therefore, the fabrication variation in the wafer level resulted in the large *DR* deviation in the frame-coupled resonators. As we know from the Eq. 3.12, the smaller the DR is, the larger anti-phase amplitude becomes. So it is better to design spring-coupled resonator in the view point of *DR* deviation. The stiffness unbalance in spring-coupled designs are smaller than frame-coupled designs as given in Table 5.8. The spring-coupled resonators had narrower beams than frame-coupled resonators and the stiffness unbalance in spring-coupled designs is smaller. Therefore, we should select the spring-coupled resonators in the view point of Δk. Similarly in in-plane coupled resonators, from the measured results in Fig. 4.18, *DR* deviation is large in frame-coupled resonators and *DR* values are larger compared to spring-coupled resonators. Although, the beams were designed with in-plane bending beams, the frame-coupled resonators showed *DR* deviations. Since the DR values of frame-coupled designs larger, the anti-phase amplitude or acceleration output of frame-coupled resonators are smaller. So it is better to select the frame-coupled resonators in the view point of DR deviation in in-plane coupled resonators. The stiffness unbalance in spring-coupled designs are smaller than frame-coupled designs as given in Table 4.3. The spring-coupled resonators had narrower beam than frame-coupled resonators and the stiffness unbalance in spring-coupled designs is smaller. Therefore, we should select the spring-coupled resonators in the view point of Δk.

In comparison of motion types, the torsional motion types (B, D1) seem to show lower anti-phase amplitudes than the translational ones (A1, C). However, it is difficult to compare the absolute anti-phase amplitudes of translational and torsional motions, since the actual capacitance change of both translational and torsional motion types against parameters such as anti-phase amplitude and rate induced Coriolis displacement is

different. But, the linearity between the displacement and sense electrode capacitance is large in translation types compared to the torsional types. In the case of in-plane coupled resonators, both resonators has same motion type.

The merits and demerits of each type resonator are listed in Table 5.9 for out-of-plane coupled resonator and for in-plane coupled resonator in Table 5.10. If the resonators are fabricated within tight-control of process variations (or fabrication conditions), the DR shift can be minimized in both in-plane and out-of-plane coupled resonators. In the remaining aspect of stiffness unbalance, however may be the fabrication conditions, the spring-coupled resonators will have smaller stiffness unbalance. Therefore, spring-coupled designs (translational motion for out-of-plane) is best choice as sense resonators used in TFG.

Table 5.9 Comparison of the out-of-plane resonators for robust TFG design in out-of-plane sensing axis.

	Frame-coupled		Spring-coupled	
	Translational	Torsional	Translational	Torsional
DR deviation (interms of DR values)	Large (×)	Large (×)	Small (O)	Small (O)
Stiffness unbalance	Large (×)	Large (×)	Small (O)	Small (O)
Sensing linearity	Good (O)	Bad (×)	Good (O)	Bad (×)

Table 5.10 Comparison on the in-plane resonators for robust TFG design in in-plane sensing axis.

	Frame-coupled	Spring-coupled
DR deviation (interms of DR values)	Large (O)	Small (×)
Stiffness unbalance	Large (×)	Small (O)

5.11 Summary

To verify the frequency decoupling method for out-of-plane sensing axis TFG, we designed four types of out-of-plane coupled resonators: two frame-coupled and two spring-coupled with translational and torsional motion. These designs were fabricated with the SOG process. Frequency sweep responses showed resonant anti-phase vibration in out-of-plane coupled resonators. The fabrication error leads to unbalance in stiffness between two unit resonators that causes anti-phase mode vibrations, which will be manifested as angular rate output in TFG. The results also showed that a large decoupling ratio designs has lower anti-phase amplitude. Furthermore, the SOG chips showed large frequency deviations and large *DR* deviations that might be due to large fabrication non-uniformity across the wafer. We fabricated another set of coupled resonators with better fabrication conditions using standard SOI process. The SOI chips showed smaller anti-phase amplitudes, frequency deviations and *DR* deviations than SOG chips. The SOI measurements also showed that smaller anti-phase amplitudes at large *DR*. We proved that the frequency decoupling method is also effective to suppress the acceleration output caused by sensing resonators in *x*-axis TFGs. The measurement results of both in-plane and out-of-plane coupled resonators were compared for best choice of resonator to design anti-shock TFG design. In the comparison, we found that the spring-coupled resonators as best choice for the design of anti-shock TFG. Our results revealed that anti-shock TFGs in both in-plane and out-of-plane sensing axes can be designed by setting large decoupling ratio in sense resonators and selecting spring-coupling designs (translational motion) as sense resonators.

Chapter 6

Conclusions and future works

The reliability of gyroscope operation is very important in the automotive applications due to harsh environment conditions. A tuning fork gyroscope (TFG) is best suitable for this kind of application due to differential operation and common mode rejection. However, TFGs indeed produce acceleration output. There is no clear understanding on the mechanism of source of acceleration output and its suppression methods. In this thesis, we investigated the mechanism of acceleration output and proposed a design method to suppress the acceleration output.

6.1 Thesis contributions

In this dissertation, the source of acceleration sensitivity and its suppression method (frequency decoupling method) is theoretically and numerically analysed in a TFG and in-plane and out-of-plane coupled resonators were designed to investigate experimentally. The specific contributions of presented research include;

1) The source of the acceleration output is identified as excitation sense anti-phase vibration against a shock (acceleration) signal. The sense anti-phase vibration will appear on the gyro output as acceleration output. We have proposed a method to reduce the anti-phase vibration by decoupling two modes in sense resonators (frequency decoupling). In the proposed frequency decoupling method, which is "sense in-phase mode (ω_{in}) should be separated as far as possible from the sense anti-phase mode (ω_{anti})", anti-phase frequency is kept constant. The large frequency decoupling (decoupling ratio, $DR=(\omega_{anti}-\omega_{in})/\omega_{anti}$) value implies two modes separated largely. By using the decoupling method, large *DR* designs shows smaller anti-phase vibration amplitude (or acceleration output). To verify the source of acceleration output and frequency decoupling method, theoretical and numerical analysis is carried out on a TFG and experiments were carried out on in-plane and out-of-plane coupled resonators.

2) Theoretical analysis of unbalanced TFG showed that the differential amplitude i.e, the difference of two sensing resonators, has a peak amplitude at sense anti-phase frequency in mode-matched operation. This is confirmed by the numerical analysis, wherein the sensing resonator displacement against shock signal showed a peak at sense anti-phase frequency. The theoretical analysis showed that differential amplitude is proportional to stiffness unbalance and inverse to *DR* and cubic of anti-phase frequency. The numerical

analysis also showed that large *DR* TFGs have smaller acceleration output. The theoretical and numerical analysis also showed that the angular rate sensitivity of a TFG does not change by keeping anti-phase frequency constant.

3) In-plane coupled resonators were designed with two types of coupling schemes; one with frame-coupling and the other with spring-coupling. We fabricated symmetrically designed in-plane coupled resonators using SOI wafer. An artificial stiffness unbalance in between two resonators of a coupled resonator was created to simulate the actual fabricated TFG. The FEA simulation showed that two resonators are oscillated in anti-phase mode against applied in-phase oscillation. The FEA simulations showed smaller anti-phase amplitude in larger *DR* designs. In the measurements, the frequency response showed that resonators are oscillated in anti-phase mode against in-phase oscillation, since the fabricated resonators are always have some unbalance in stiffness and mass between resonators. The measurements also showed that smaller anti-phase output in large *DR* designs. However the measurement results showed discrepancies in anti-phase output in two types; frame-coupled and spring-coupled. So the measured results were normalized to the designed *DR*, frequencies and calculated stiffness unbalances with the theoretically derived frequencies. After normalization, there is no difference in two types of coupling effects on anti-phase amplitudes.

4) Four types of out-of-plane coupled resonators; two frame-coupled and two spring-coupled with translational and torsional motion, were designed and fabricated on SOI wafer. The measured frequency response showed that resonators are excited in anti-phase mode against in-phase oscillation. The measured results were normalized same as in-plane coupled resonators. The normalized results did not show any difference on anti-phase amplitudes in two types of coupling and two types of motion. The larger DR designs showed smaller anti-phase amplitudes. We confirmed from the theoretical and numerical analysis, and experiments that the source of acceleration sensitivity is the sense anti-phase vibration due to stiffness unbalance and acceleration output can be decreased by frequency decoupling method. From the measurements of in-plane and out-of-plane coupled resonators, we compared the resonators for selection of best resonator. Our comparison against *DR* deviation, stiffness unbalance revealed that spring-coupled (translational) designs are best choice as sense resonators used in TFG. From the theoretical and numerical analysis and experiments, we conclude that TFG can be designed with smaller acceleration sensitivity by setting large decoupling ratio and spring-coupled method in sense resonators.

6.2 Future works

In the presented work, the in-plane and out-of-plane coupled resonators are having in-phase and anti-phase resonance modes as primary and secondary modes. In this mode ordering case, if a shock signal consisting of wide frequency spectrum is applied along the sense-axis of TFG, sense resonators vibrate with large displacement amplitudes in in-phase and with smaller amplitudes in anti-phase mode. The large in-phase displacements may worse the shock performance of TFGs. So, it is better to design the anti-phase and in-phase resonance modes of sense resonators as primary and secondary modes. The higher stiffness of in-phase mode causes smaller in-phase vibration and transduction from in-phase to anti-phase. To design this kind of mode ordering, there is a need to find a new type of coupling springs that causes anti-phase modal stiffness smaller than in-phase modal stiffness.

In the coupled resonators, we fixed the anti-phase frequency and varied the in-phase frequency. By fixing the anti-phase frequency, we assumed that TFGs might have same rate sensitivity, which is confirmed by the theoretical and numerical analysis. In the future works, complete TFG will be fabricated with a small and a large *DR*s. These devices can be tested while oscillating the drive resonators and show the constant angular rate sensitivity in both the *DR* designs experimentally.

Appendices

Appendix A

The in- and anti-phase frequencies are derived for in-plane frame- and spring-coupled designs.

Frame-coupled design:

The lumped mass-spring modal of frame-coupled design is shown Fig. A.1

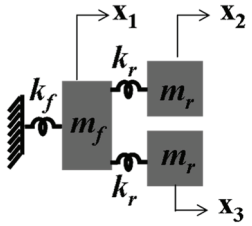

Figure A.1 Lumped mass-spring model of frame-coupled type design.

In the Figure, m_f and m_r represents the frame and resonator mass, respectively. k_f and k_r are stiffnesses of frame and resonator, respectively. Damping is ignored to solve the equations. The equations of motion are written as:

$$m_f\ddot{x}_1 + k_f x_1 + k_r(x_1 - x_2) + k_r(x_1 - x_3) = 0 \qquad \text{---- A.1}$$

$$m_r\ddot{x}_2 + k_2(x_2 - x_1) = 0 \qquad \text{---- A.2}$$

$$m_r\ddot{x}_3 + k_3(x_3 - x_1) = 0 \qquad \text{---- A.3}$$

By applying the Laplace transformation to the above equations:

$$(s^2 m_f + k_f + 2k_r)x_1(\mathrm{s}) + (-k_r)x_2(s) + (-k_r)x_3(s) = 0 \qquad \text{---- A.4}$$

$$(s^2 m_r + k_2)x_2(s) + (-k_2)x_1(s) = 0 \qquad \text{---- A.5}$$

$$(s^2 m_r + k_3)x_3(s) + (-k_3)x_1(s) = 0 \qquad \text{---- A.6}$$

From equation 5,

$$x_2(s) = \frac{k_2}{(s^2 m_r + k_2)}x_1(s) \qquad \text{---- A.7}$$

From equation 6,

$$x_3(\mathrm{s}) = \frac{k_3}{(s^2 m_r + k_3)}x_1(s) \qquad \text{---- A.8}$$

By substituting equations (7) & (8) in the equation (4)

$$\left(s^2 m_f + k_f + 2k_r\right)x_1(s) + \left(\frac{-k_2^2}{s^2 m_r + k_2}\right)x_1(s) + \left(\frac{-k_3^2}{s^2 m_r + k_3}\right)x_1(s) = 0 \qquad \text{---- A.9}$$

By solving the above equation for $x_1(s)$:

$$s^4 m_f m_r + s^2 \left[m_f k_r + m_r (k_f + 2k_r) \right] + k_f k_r = 0$$

By substituting s=jω:

$$\omega^4 m_f m_r - \omega^2 \left[m_f k_r + m_r (k_f + 2k_r) \right] + k_f k_r = 0$$

Finding the roots of the above equation:

$$\omega^2 = \frac{\left[m_f k_r + m_r (k_f + 2k_r) \right] \pm \sqrt{\left[m_f k_r + m_r (k_f + 2k_r) \right]^2 - 4 m_f m_r k_f k_r}}{2 m_f m_r} \qquad \text{---- A.10}$$

The two roots represent the in-phase motion of the frame-coupled design. The in-phase frequency (f_{in}) of two resonators is:

$$\omega_{in}^2 = \frac{\left[m_f k_r + m_r (k_f + 2k_r) \right] - \sqrt{\left[m_f k_r + m_r (k_f + 2k_r) \right]^2 - 4 m_f m_r k_f k_r}}{2 m_f m_r} \qquad \text{---- A.11}$$

The anti-phase frequency of the frame-coupled design is derived as follows.

The equation (8) is substituted in the equation (4), then

$$x_1(s) = \frac{k_r}{\left(s^2 m_f + k_f + 2k_r - \dfrac{k_r^2}{s^2 m_r + k_r} \right)} x_2(s) \qquad \text{---- A.12}$$

By substituting the equation (12) in the equation (5),

$$x_2(s) \left[(s^2 m_r + k_r) \left\{ s^4 m_f m_r + s^2 k_r (m_f + 3m_r) + k_r k_f + k_r^2 \right\} - k_r^2 (s^2 m_r + k_r) \right] = 0 \qquad \text{---- A.13}$$

The roots of the above equation can be derived as:

$$s^6 m_f m_r^2 + s^4 (2 m_f m_r k_r + 3 m_r^2 k_r) + s^2 (m_r k_f k_r + m_f k_r^2 + 3 m_r k_r^2) + k_f k_r^2 = 0$$

By substituting s=jω:

$$-\omega^6 m_f m_r^2 + \omega^4 (2 m_f m_r k_r + 3 m_r^2 k_r) - \omega^2 (m_r k_f k_r + m_f k_r^2 + 3 m_r k_r^2) + k_f k_r^2 = 0 \qquad \text{---- A.14}$$

The cubic roots of the ω^2 equation can be solved any mathematical software.

Since, at the anti-phase frequency, the coupling frame vibration is null, the anti-phase frequency (f_{anti}) can be considered as the resonance frequency of the individual resonator, which is

$$\omega_{anti}^2 = \sqrt{\frac{k_r}{m_r}} \qquad \text{---- A.15}$$

Spring-coupled design:

The lumped mass-spring modal of frame-coupled design is shown Fig. A.2

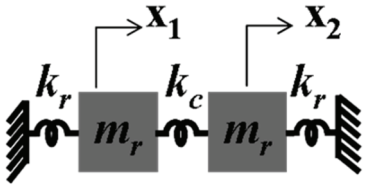

Figure A.2 Lumped mass-spring model of spring-coupled type design.

In the Fig. A.2, m_r represents the resonator mass. K_r and k_c are stiffnesses of resonator and coupling suspension stiffnesses, respectively. The equations of motion are written in 's' domain as:

$$(s^2 m_r + k_r + k_c)x_1(s) + (-k_c)x_2(s) = 0 \qquad \text{---- A.16}$$

$$(-k_c)x_1(s) + (s^2 m_r + k_r + k_c)x_2(s) = 0 \qquad \text{---- A.17}$$

By substituting equation (17) in equation (16), then

$$\left[(s^2 m_r + k_r + k_c)^2 - k_c^2\right]x_1(s) = 0 \qquad \text{---- A.18}$$

By substituting s=jω:

$$\omega^4 m_r^2 - 2\omega^2 m_r(k_r + k_c) + (k_r^2 + 2k_r k_c) = 0 \qquad \text{---- A.19}$$

The roots of the above equations are in- and anti-phase frequencies:

$$\omega_{in}^2 = \frac{k_r}{m_r} \qquad \text{---- A.20}$$

$$\omega_{anti}^2 = \frac{k_r + 2k_c}{m_r} \qquad \text{---- A.21}$$

Appendix B

Four types of suspension springs are used for suspending the resonators and anchoring with substrate.

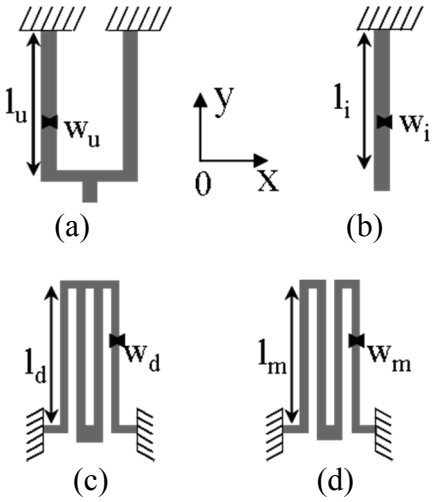

Figure B.1 Designed spring models of the in-plane coupled resonator (a) anchored spring (U-shape spring) and (b) suspension spring (guided beam) of frame-coupled design, and (c) anchored spring (folded spring) and (d) coupling spring (meander spring) of spring-coupled design.

The spring constants for the above sprigs are designed as follows. Energy method was used to derive the analytical formulae for linear spring constants. The spring constant (k) is derived as

$$k = \frac{F}{\delta} \qquad \text{---- B.1}$$

where F is applied force and δ is resulted displacement. Castigliano's theorem states that the partial derivative of the strain energy of a linear structure, U, with respect to a given load, P_i, is equal to the displacement at the point of application of the load, δ_i.

$$\delta_i = \frac{\partial U}{\partial P_i}$$

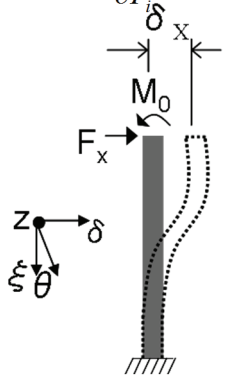

Figure B.2 Guided end beam with length L, width, w, and thickness t. The dotted line is beam displaced by δx.

Fig. B.2 is a schematic of one guided end beam having length L, width w, and thickness t. A lateral force, F_x, is applied at the end of the beam, resulting in a displacement, δ_x. An external bending moment, M_0, constrains the angle in the analysis. The beam bending moment is $M=M_0-F_x\xi$, where ξ is the distance from the guided end. The strain energy of the beam is found by integrating the strain energy density along the beam.

$$U = \int_0^L \frac{M^2}{2EI_z} d\xi \qquad \text{---- B.2}$$

where E is Young's modulus of elasticity and I_z is the bending moment of inertia about the z-axis. The moment of inertia of the rectangular beam cross section is given by

$$I_z = \int_{-t/2}^{t/2} \int_{-w/2}^{w/2} x^2 dx dz = \frac{tw^3}{12} \qquad \text{---- B.3}$$

The product EI_z is called the flexural rigidity of the beam.

A first invocation of Castigliano's theorem, combined with the constraint θ_0, gives a relation between the external moment and the load.

$$\theta_0 = \frac{\partial U}{\partial M_0} = \int_0^L \frac{M}{EI_z} \frac{\partial M}{\partial M_0} d\xi = \frac{1}{EI_z} \int_o^L (M_o - F_x \xi) d\xi = 0 \qquad \text{---- B.4}$$

Solving for the bending moment gives $M_0=F_x(L/2)$ and $M=F_x(L/2-\xi)$. The calculation is simplified by bringing the partial derivative inside the integral in Eq. B.4. The partial derivative in the integrated ($\partial M/\partial M_0$ in the Eq. B.4) is the moment resulting from a unit load (M_0) applied to the beam. Hence, this modification of Castigliano's second theorem is called the unit load method.

The unit load method is employed a second time to determine the deflection at the end of the beam.

$$\delta_x = \frac{\partial U}{\partial F_x} = \int_0^L \frac{M}{EI_z} \frac{\partial M}{\partial F_x} d\xi = \frac{F_x}{EI_z} \int_0^L \left(\frac{L}{2} - \xi \right)^2 d\xi = \frac{F_x L^3}{12EI_z} \qquad \text{---- B.5}$$

The guided end cantilever beam spring constant is

$$k_{x,beam} = \frac{F_x}{\delta_x} = \frac{12EI_z}{L^3} = \frac{tw^3}{L^3} \qquad \text{---- B.6}$$

The U-shaped spring constant is simply addition of two guided beams stiffnesses.

$$k_u = \frac{2t_u w_u^3}{L_u^3} \qquad \text{---- B.7}$$

The folded flexure spring behaves as a simple guided end beam. Therefore folded flexure spring constant is:

$$k_d = \frac{t_d w_d^3}{L_d^3} \qquad \text{---- B.8}$$

The meander spring constant is just one-fourth of guided end beam spring constant.

$$k_m = \frac{t_m w_m^3}{4L_m^3} \qquad \text{---- B.9}$$

Bibliography

[1] D. Piyabongkarn, R. Rajamani, and M. Greminger, “The Development of a MEMS Gyroscope for Absolute Angle Measurement”, IEEE Trans. Control Systems Tech., vol. 13, no. 2, pp. 185-195 (2005).

[2] S. A. Jerebets, "Gyro evaluation for the mission to Jupiter", in *Proc.* IEEE Aerospace Conference, Big Sky, MT, pp. 1-9 (2007).

[3] K. Liu et.al, “The development of micro-gyroscope technology”, Journal of micromechanics and microengineering, vol. 19, pp. 1-29 (2009).

[4] A. Lawrence, “Modern inertial technology”, Springer-Verlag, 1993.

[5] A. A. Michelson, H. G. Gale, and F. Pearson, “The Effect of the Earth's Rotation on the Velocity of Light,” Astrophysical Journal, vol. 61, pp. 140-145 (1925).

[6] V. Vali and R. W. Shorthill, “Fiber Ring Interferometer”, Applied Optics, vol. 15, no.5, pp.1099-1100 (1976).

[7] R. A. Bergh, H. C. Lefevre, and H. J. Shaw, “All single mode fiber optic gyroscope”, Optics Letters, vol. 6, no.4, pp. 198–200 (1981).

[8] A. H. Rosenthal, "Regenerative Circulatory Multiple Beam Interferometry for the Study of Light Propagation Effects", J.O.S.A., vol. 52, pp. 1143-1148 (1962).

[9] W. M. Macek, and D. T. M. Davis, "Rotation Rate Sensing With Travelling Wave Ring Lasers", Applied Physics Letters, vol. 2, pp. 67-68 (1963).

[10] W. W. Chow, J. G. Banacloche, and L. M. Pedrotti., "The Ring Laser Gyro", Reviews of Modern Physics, vol. 57, no.1, pp. 61-104 (1985).

[11] E. A. Donley, “Nuclear Magnetic Resonance Gyroscopes”, IEEE SENSORS 2010 conference.

[12] M. Larsen, “Nuclear Magnetic Resonance Gyroscope: For DARPA's micro-technology for positioning, navigation and timing program”, Frequency Control Symposium (FCS), pp.1-5 (2012).

[13] D. M. Rozelle, “The hemispherical Resonator Gyro: From Wineglass to the Planets”, http://www.northropgrumman.com/Capabilities/HRG/Documents/hrg.pdf

[14] A. Matthews and F. J. Rybak, "Comparison of hemispherical resonator gyro and optical gyros", in IEEE Aerospace and Electronic Systems Magazine, vol. 7, no. 5, pp. 40-46 (1992).

[15] N. Yazdi, F. Ayazi, and K. Najafi, “Micromachined inertial sensors”, in *Proc.* of the IEEE, vol. 86, no. 8, pp. 1640-1659 (1998).

[16] C. Acar and A. M. Shkel, “MEMS Vibratory gyroscopes: Structural Approaches to Improve Robustness”, ISBN: 978-0-387-09535-6.

[17] W. Lang, “Reflexions on the future of microsystems”, Sensors and Actuators A, vol. 72, pp.1-15 (1999).

[18] M. Kraft, “Micromachined inertial sensors: the state-of-the-art and a look into the future”, Meas. Control, vol. 33, pp. 164-168 (2000).

[19] A. Kourepenis, J. Borenstein, J. Connelly, R. Elliott, P. Ward, and M. Weinberg, "Performance of MEMS inertial sensors", in IEEE Position Location and Navigation

Symposium, Palm Springs, CA, pp. 1-8 (1998).

[20] J. Marek, “Slilicon Microsystems for Automotive Applications”, in *Proc.* 13th Eur. Conf. Solid-State Transducers (Eurosensors XIII), The Hague, The Netherlands, pp. 1-8 (1999).

[21] H. Kuisma, “Inertial Sensors for Automotive Applications”, Tech. Dig. 11th Int. Conf. Solid-State Sensors and Actuators (Transducers’01), Munich, Germany, pp. 430-433 (2001).

[22] A. M. Madni, L. E. Costlow and S. J. Knowles, “Common Design Techniques for BEI GyroChip Quartz Rate Sensors for Both Automotive and Aerospace/Defense Markets,” IEEE Sensors, vol. 3, no. 5, pp. 569–578 (2003).

[23] A. M. Madni and R. D. Geddes, “A Micromachined Quartz Angular Rate Sensor for Automotive and Advanced Inertial Applications”, Sensors Magazine, vol. 16, no. 8, (1999).

[24] H. Jeong et al. “Three-Axis MEMS Inertial Sensor for Automobile Applications”, IEEE SENSORS conference proceeding (2011).

[25] D. Karnick, G. Ballas, L. Koland, M. Secord, T. Braman, and T. Kourepenis, “Honeywell Gun-hard Inertial Measurement Unit (IMU) Development”, IEEE Position Location and Navigation Symp. (PLANS’04), Monterey, CA, pp. 49-55 (2004).

[26] G. T. Schmidt, “INS/GPS Technology Trends”, NATO RTO Sensors & Electronics Technology (RTO-SET) Panel: Symp. Emerging Military Capabilities Enabled by Advances in Navigation Sensors (SET’02), Istanbul, Turkey (2002).

[27] F. Ayazi, “Multi-DOF Inertial MEMS: From gaming to dead reckoning”, in *Proc.* 16th International Conference on Solid-State Sensors, Actuators and Microsystems (Transducers’11), Beijing, China, pp. 2805-2808 (2011).

[28] P. Greiff, B. Boxenhorn, T. King, and L. Niles, "Silicon monolithic micromechanical gyroscope," in *Proc.* International Conference on Solid-State Sensors and Actuators (Transducers '91), San Francisco, CA, pp. 966-968 (1991).

[29] J. Bernstein, S. Cho, A. T. King, A. Kourepenis, P. Maciel, and M. Weinberg, "A micromachined comb-drive tuning fork rate gyroscope", in *Proc.* IEEE Inverstigation of Micro Structures, Sensors, Actuators, Machines and Systems (MEMS’93), Fort Lauderdale, FL, pp. 143-148 (1993).

[30] T. Juneau, A. P. Pisano, and J. H. Smith, "Dual axis operation of a micromachined rate gyroscope," in *Proc.* International conference on Solid-State Sensors and Actuators (Transducers'97), Chicago, IL, pp. 883-886 (1997).

[31] M. Yachi, H. Ishikawa, Y. Satoh, Y. Takahashi, and K. Kikuchi, "Design methodology of single crystal tuning fork gyroscope for automotive applications", in *Proc.* IEEE Ultrasonics Symposium, Sendai, Japan, pp. 463-466 (1998).

[32] J. S. Burdess and T. Wren, "The theory of a piezoelectric disc gyroscope", IEEE Trans. Aerosp. Electron. Syst., vol. AES-22, pp. 410 -418 (1986).

[33] F. Paoletti, M. A. Gretillat, and N. F. de Rooij, "A silicon micromachined vibrating gyroscope with piezoresistive detection and electromagnetic excitation," in *Proc.* 9th IEEE International Workshop an Investigation of Micro Structures, Sensors, Actuators, Machines and Systems (MEMS’96), San Diego, CA, pp. 162-167 (1996).

[34] R. Voss et al., "Silicon angular rate sensor for automotive applications with piezoelectric drive and piezoresistive read-out," in *Proc*. International conference on Solid-State Sensors and Actuators (Transducers'97), Chicago, IL, pp. 847-850 (1997).

[35] H. Yang, M. Bao, H. Yin, and S. Shen, "A Novel Bulk Micromachined Gyroscope Based on a Rectangular Beam-Mass Gyroscope", Sensors Actuators A, vol. 96, pp. 145-151 (2002).

[36] S. Zhaohui, C. Xuemeng, H. Shusen, W. Yuelin, J. Jiwei, and L. Xinxin, "A High-Sensitivity Piezoresistive Gyroscope with Torsional Actuation and Axially-Stressed Detection", in *Proc.* IEEE Sensors Conf., Toronto, Canada, pp. 457-460 (2003).

[37] R. L. Kubena, D. J. Vickers-Kirby, R. J. Joyce, and F. P. Stratton, "New miniaturized tunneling-based gyro for inertial measurement applications", J. Vacuum Science & Technology B: Microelectronics and Nanometer Structures, vol. 17, no. 6, pp. 2948-2952 (1999).

[38] J. Harris, J. S. Burdess, D. Wood, R. Langford, G. Williams, and M. E. McNie, "Issues associated with the design, fabrication and testing of a crystalline silicon ring gyroscope with electromagnetic actuation and sensing", in Journal of Micromechanics and Microengineering, vol. 8, no. 4, pp. 284-92 (1998).

[39] F. Ayazi, and K. Najafi, "Design and fabrication of a high-performance polysilicon vibrating ring gyroscope", in *Proc.* IEEE Micro Electro Mechanical Systems Workshop (MEMS',98), pp.621 -626 (1998).

[40] R. Eley, C. H. J. Fox, S. MaWilliam, "Anisotropy effects on the vibration of circular rings made from crystalline silicon", Journal of Sound and Vibration, vol. 228, pp. 11–35 (1999).

[41] F. Ayazi, and K. Najafi, "A HARPSS polysilicon vibrating ring gyroscope", Journal of Microelectromechanical Systems, vol. 10, pp. 169–179 (2001).

[42] A. K. Rourke, S. McWilliam, and C. H. J. Fox, "Multi-modes trimming of imperfect rings", Journal of Sound and Vibration, pp. 695–724 (2001).

[43] G. He, and K. Najafi, "A single-crystal silicon vibrating ring gyroscope", in Dig. Tech. Papers, Solid State Sensors, Actuators and Microsystems Workshop (Hilton Head), pp. 718–721 (2002).

[44] J. H. Weng, W. H. Chieng, and J.-M. Lai, "Structural design and analysis of micromachined ring-type vibrating sensor of both yaw rate and linear acceleration", Sensors and Actuators A: Physical, vol. 117, pp. 230–240 (2005).

[45] B. J. Gallacher, J. A. Neasham, J. S. Burdess, and A. J. Harris, "Initial test results from a 3-axis vibrating ring gyroscope", in Journal of Physics: ConferenceSeries, vol. 34, no. 1, pp. 662-667 (2006).

[46] M. Esmaeili, M. Durali and N. Jalili, "Ring microgyroscope modeling and performance evaluation", Journal of Vibration and Control, vol. 12, pp. 537–553 (2006).

[47] S. Asokanthan, and J. Cho, "Dynamic response-based characterization of ring-based vibratory angular rate sensors", Journal of Mechanical Science and Technology, vol. 21, pp. 965–969 (2007).

[48] C. O. Chang, G. E. Chang, C. S. Chou, W.T.C. Chien, and P.-C. Chen, "In-plane free vibration of a single-crystal silicon ring", International Journal of Solids and

Structures, vol. 45, pp. 6114–6132 (2008).

[49] M. F. Zaman, A. Sharma, B. V. Amini, and F. Ayazi, “The resonating star gyroscope”, in Dig. Tech. Papers, IEEE International Conference on Micro Electro Mechanical Systems (MEMS), Miami, FL, USA, pp. 355–358 (2005).

[50] M. F. Zaman, A. Sharma, and F. Ayazi, “The resonatoing star Gyroscope: A Novel Mulitple-Shell Silicon Gyroscope with Sub-5 deg/hr Allan deviation bias Instability”, IEEE SENSORS JOURNAL, vol. 9, no. 6, pp. 616-624 (2009).

[51] Z. Hao, and F. Ayazi, "Support Loss in Micromechanical Disk Resonators," in *Proc.* of IEEE/ASME Conference on Microelectromechanicalsystems (MEMS '05), Miami, FL, pp. 137-141 (2005).

[52] H. Johari, and F. Ayazi, "Capacitive Bulk Acoustic Wave Silicon Disk Gyroscopes," in Tech. Digest of International Electron Device Meeting (IEDM’06), San Francisco, CA, pp. 513-516 (2006).

[53] Z. Hao and F. Ayazi, “Support loss in the radial bulk-mode vibrations of center supported micromechanical disk resonators”, in Sensors and Actuators A (Physical), vol. 134, no. 2, pp. 582-593 (2007).

[54] H. Johari, and F. Ayazi, "High frequency capacitive disk gyroscopes in (100) and (111) silicon”, in *Proc.* of IEEE/ASME Conference on Microelectromechanicalsystems (MEMS '07), Kobe, Japan, pp. 47-50 (2007).

[55] J. Shah, H. Johari, A. Sharma, and F. Ayazi, “CMOS ASIC for MHz Silicon BAW Gyroscope,” in IEEE International Symposium on Circuits and Systems (ISCAS’08), Seattle, Washington, pp. 2458-2461 (2008).

[56] H. Johari, J. Shah, and F. Ayazi, “High frequency xyz-axis single-disk silicon gyroscope,” in P*roc.* of IEEE/ASME Conference on Microelectromechanicalsystems (MEMS’08), Tucson, AR, pp. 856-9 (2008).

[57] H. Johari, “Micromachined Capacitive Silicon Bulk Acoustic Wave Gyroscopes”, Ph.D dissertation (2008).

[58] Y. Tao, X. Wu, D. Xiao, Y. Wu, H. Cui, X. Xi, and B. Zhu, “Design, analysis and experiment of a novel ring vibratory gyroscope”, Sensors and Actuators A: Physical, vol. 168, pp. 286–299 (2011).

[59] G. Pickett, “Flexural vibration of unrestrained cylinders and disks”, Journal of applied physics, vol. 16, pp. 820-831 (1945).

[60] Y. Ting, J. S. Huang, J. L. Huang, and C. M. Yang, “Effect of polarized electric field on piezoelectric cylinder vibratory gyroscope”, Sensors and Actuators A, vol. 128, pp. 248-256 (2006).

[61] J. Cho, J.A. Gregory, and K. Najafi, "Single-Crystal-Silicon Vibratory Cylindrical Rate Integrating Gyroscope (CING)", in *Proc.* 16th International Conference on Solid-State Sensors, Actuators, and Microsystems (TRANSDUCERS’11), Beijing, China, pp. 2813-2816 (2011).

[62] J. Cho, J.A. Gregory, and K. Najafi, “HIGH-Q, 3KHZ SINGLE-CRYSTAL-SILICON CYLNDRICAL RATE-INTEGRATING GYRO (CING)”, MEMS 2012, Paris, FRANCE, pp. 172-175 (2012).

[63] S. Kim, B. Lee, J. Lee, and K. Chun, "A gyroscope array with linked-beamstructure," in *Proc.* 14th International Conference on Micro Electro Mechanical Systems

(MEMS'01), Interlaken, Switzerland, pp. 30-33 (2001).

[64] J. A. Geen, "Very Low Cost Gyroscopes," in *Proc.* IEEE Sensors 2005, Irvine, CA, pp. 537-540 (2005).

[65] I. P. Prikhodko, S. A. Zotov, A. A. Trusov, and A. M. Shkel, "Foucault Pendulum on a Chip: Rate Integrating Silicon MEMS Gyroscope" in *Proc.* 24th IEEE International Conference on Micro Electro Mechanical Systems (MEMS'11), Cancun, Mexico, pp. 161-164 (2011).

[66] M. Weinberg, J. Connelly, A. Kourepenis, and D. Sargent, "Microelectromechanical instrument and systems development at the Charles Stark Draper Laboratory, Inc," in *Proc.* 16th IEEE Digital Avionics Systems Conference, Irvine, CA, pp. 8.5.33-8.5.40 (1997).

[67] M. Lutz, W. Golderer, J. Gerstenmeier, J. Marek, B. Maihofer, S. Mahler, H.Munzel, and U. Bischof, "A precision yaw rate sensor in silicon micromachining,"in *Proc.* International conference on Solid-State Sensors and Actuators (Transducers'97), Chicago, IL, pp. 847-850 (1997).

[68] G. I. Andersson, N. Hedenstierna, P. Svensson, and H. Pettersson, "A novel silicon bulk gyroscope", in *Proc.* 10th International Conference on Solid-State Sensors and Actuators (Transducers' 99), Sendai, Japan, pp. 902–905 (1999).

[69] N. Hedenstierna, S. Habibi, S. M. Nilsen, T. Kvisteroy, and G. U. Jensen, "Bulk micromachined angular rate sensor based on the butterfly'-gyro structure", in *Proc.* 14th International Conference on Micro Electro Mechanical Systems (MEMS'01), Interlaken, Switzerland, pp. 178-181 (2001).

[70] M. Fujiyoshi, Y. Nonomura, Y. Omura, K. Tsukada, S. Matsushige, and N. Kurata, "Modeling and Vibration Analysis of a Quartz Yaw Rate Sensor to Reduce Mechanical Coupling", in *Proc.* Int. Symp. on Micromechatronics and Human Science (MHS'01), Nagoya, Japan, pp. 105-108 (2001).

[71] J. A. Geen, "Single-chip surface micromachined integrated gyroscope with 50 deg/h Allan deviation," IEEE J. Solid-State Circuits, vol. 37, no. 12, pp. 1860-1866 (2002).

[72] M. F. Zaman, A. Sharma, and F. Ayazi, "High Performance Matched-Mode Tuning Fork Gyroscope," in *Proc.* 19th IEEE International Conference on Micro Electro Mechanical Systems (MEMS'06), Istanbul, Turkey, pp. 66-69 (2006).

[73] K. Azgin, Y. Temiz, and T. Akin, "An SOI-MEMS tuning fork gyroscope with linearly coupled drive mechanism," in *Proc.* 20th IEEE International Conference on Micro Electro Mechanical Systems (MEMS'07), Kobe, Japan, pp. 607-610 (2007).

[74] M. F. Zaman, A. Sharma, and F. Ayazi, "A 0.1deg/Hr bias drift electronicallymatched tuning fork microgyroscope," in *Proc.* 21st IEEE International Conference on Micro Electro Mechanical Systems (MEMS'08), Tucson, AZ, pp. 6-9 (2008).

[75] J. A. Geen, "Progress in integrated gyroscopes", in *Proc.* Position, Location, and Navigation Symposium (PLANS), Monterey, CA, USA, pp. 1–6 (2004).

[76] S. H. Lee, "Wafer-Level Packaging for Environment-Resistant Microinstruments," Ph.D. dissertation (2008).

[77] A. R. Schofield, A. A. Trusov, and A. M. Shkel, "Multi-Degree of Freedom Tuning Fork Gyroscope Demonstrating Shock Rejection", IEEE SENSORS Conf. (Georgia,

USA), pp. 120-123 (2007).

[78] C. Acar and A. M. Shkel, “MEMS Vibratory Gyroscopes: Structural Approaches to Improve Robustness”, Springer, ISBN 978-0387-09535-6

[79] S. S. Baek, Y. S. Oh, B. J. Ha, S. D. An, B. H. An, H. Song, and C. M. Song, "A symmetrical z-axis gyroscope with a high aspect ratio using simple and new process," in *Proc.* 12th IEEE International Conference on Micro Electro Mechanical Systems (MEMS’99), Orlando, FL, pp. 612-617 (1999).

[80] T. Tsuchiya, Y. Kageyama, H. Funabashi, and J. Sakata, "Vibrating gyroscope consisting of three layers of polysilicon thin films", Sensors & Actuators: A.Physical, vol. 82, pp. 114-119 (2000).

[81] IEEE Standard for Inertial Sensors Terminology, IEEE Std 528-2001, November 2001.

[82] T. B. Gabrielson, “Mechanical-Thermal Noise in Micromachined Sensors and Acoustic and Vibration Sensors”, IEEE Trans. Electron. Devices, vol. 40, no. 5, pp. 903-909 (1993).

[83] W. Geiger, W. U. Butt, A. Gaiβer, J. Frech, M. Braxmaier, T. Link, A. Kohne, P. Nommensen, H. Sandmaier, and W. Lang, “Decoupled Microgyros and the Design Principle DAVED”, Sensors and Actuators A, vol. 95, pp. 239-249 (2002).

[84] W. Geiger, B. Folkmer, J. Merz, H. Sandmaier, W. Lang, "A new silicon rategyroscope", in *Proc.* 11th IEEE International Conference on Micro ElectroMechanical Systems (MEMS’98), Heidelberg, Germany, pp. 615-620 (1998).

[85] W. Geiger, B. Folkmer, U. Sobe, H. A. S. H. Sandmaier, and W. A. L. W. Lang, "New designs of micromachined vibrating rate gyroscopes with decoupled oscillation modes", in *Proc.* International Conference on Solid State Sensors and Actuators (Transducers'97), Chicago, IL, pp. 1129-1132 (1997).

[86] S. Kobayashi, T. Hara, T. Oguchi, Y. Asaji, K. Yaji, and K. Ohwada, "Double-Frame Silicon Gyroscope Packaged Under Low Pressure By Wafer Bonding," in *Proc.* 10th International Conference on Solid-State Sensors and Actuators (Transducers' 99), Sendai, Japan, pp. 972-975 (1999).

[87] S. E. Alper, and T. Akin, "A symmetric surface micromachined gyroscope with decoupled oscillation modes", Sensors and Actuators: A. Physical, vol. 97, pp. 347-358 (2002).

[88] X. S. Liu, Z. C. Yang, X. Z. Chi, J. A. Cui, H. T. Ding, Z. Y. Guo, B. Lv, and G. Z. Yan, "An x-axis micromachined gyroscope with doubly decoupled oscillation modes," in *Proc.* 21st IEEE International Conference on Micro Electro Mechanical Systems (MEMS’08), Tucson, AZ, pp. 860-863 (2008).

[89] S. A. Bhave, J. I. Seeger, J. Xuesong, B. E. Boser, R. T. Howe, and J. A. Yasaitis, "An integrated, vertical-drive, in-plane-sense microgyroscope", in *Proc.* 12th International Conference on Solid-State Sensors, Actuators and Microsystems (Transducers'03), Boston, MA, pp. 171-174 (2003).

[90] H. Song, Y. S. Oh, I. S. Song, S. J. Kang, S. O. Choi, H. C. Kim, B. J. Ha, S. S. Baek, and C. M. Song, "Wafer level vacuum packaged de-coupled verticalgyroscope by a new fabrication process", in *Proc.* 13th International Conference on Micro Electro Mechanical Systems (MEMS’00), Miyazaki, Japan, pp. 520-524 (2000).

[91] M. Palaniapan, R. T. Howe, and J. Yasaitis, "Performance comparison of integrated z-axis frame microgyroscopes", in *Proc.* 16th International Conference on Micro Electro Mechanical Systems (MEMS'03), Kyoto, Japan, pp. 482-485 (2003).

[92] B. L. Lee, S. W. Lee, K. D. Jung, J. H. Choi, T. R. Chung, and Y. C. Cho, "A Decoupled Vibratory Gyroscope Using a Mixed Micromachining Technology", in *Proc.* IEEE Int. Conf. on Robotics & Automation (ICRA'01), Seoul, Korea, pp. 3412-3416 (2001).

[93] C. Acar and A. M. Shkel, "Structurally Decoupled Micromachined Gyroscopes with Post-Release Capacitance Enhancement", J. Micromech. Microeng., vol. 15, pp. 1092-1101 (2005).

[94] H. T. Lim, J. W. Song, J. G. Lee, and Y. K. Kim, "A Few deg/hr Resolvable Low Noise Lateral Microgyroscope", in *Proc.* IEEE Micro Electro Mechanical Systems Workshop (MEMS'02), Las Vegas, CA, pp. 627-630 (2002).

[95] S. E. Alper, K. Azgin, and T. Akin, "High-Performance SOI-MEMS Gyroscope with Decoupled Oscillation Modes", in *Proc.* 19th IEEE International Conference on Micro Electro Mechanical Systems (MEMS'06), Istanbul, Turkey, pp. 70-73 (2006).

[96] S.W. Yoon, S.W. Lee, N.C. Perkins, and K. Najafi, "Vibration sensitivity of MEMS tuning fork gyroscopes", in Dig. Tech. Papers, IEEE Sensors Conference, Atlanta, GA, USA, pp. 115–119 (2007).

[97] S. W. Yoon, S. Lee, and K. Najafi, "Vibration-induced errors in MEMS tuning fork gyroscopes", Sensors and Actuators A, vol. 180, pp. 32-44 (2012).

[98] Y. Mochida, Y. Kato, Y. Konaka, A. Mori, M. Kobayashi, S. Kobayashi, "PRECISE MEMS GYROSCOPE WITH LADDER STRUCTURE", in *Proc.* Transducers'07 & Eurosensors XXI (LYON, FRANCE), pp. 2529-2532 (2007).

[99] R. Neul, U. Gomez, K. Kehr, W. Bauer, J. Classen, C. Doring, E. Esch, S. Gotz, J. Hauer, B. Kuhlmann, C. Lang, M. Veith, and R. Willig, "Micromachined gyros for automotive applications", in *Proc.* IEEE Sensors, Irvine, CA, pp. 527-530 (2005).

[100] CoventorWare MEMS Design and Analysis Tutorial.

List of publications

Journal Papers

1) Thakur Praveen Singh, K. Sugano, T. Tsuchiya, and O. Tabata, "Frequency response of in-plane coupled resonators for investigating the acceleration sensitivity of MEMS tuning fork gyroscopes", Microsystem Technologies, Vol.18, pp.797-803 (2012)
2) Thakur Praveen Singh, K. Sugano, T. Tsuchiya, and O. Tabata, "Experimental verification of frequency decoupling effect on acceleration sensitivity in tuning fork gyroscopes using in-plane coupled resonators", Microsystem Technologies, Vol. 20, pp. 403-422 (2014)
3) Thakur Praveen Singh, K. Sugano, T. Tsuchiya, and O. Tabata, "Study on vibration-coupling control of out-of-plane coupled resonators for anti-shock tuning-fork-gyroscopes", IEEJ (E), 2014 (Accepted on June 17th)

International Conference Papers

1) Thakur Praveen Singh, K. Sugano, T. Tsuchiya, and O. Tabata, "Modal harmonic simulation of decoupled resonators for developing MEMS tuning fork gyroscope with low acceleration sensitivity", in *Proc.* of the 6th IEEE International Conference on Nano/Micro Engineered and Molecular Systems, Kaohsiung, Taiwan, pp.1297-1300 (2011).
2) Thakur Praveen Singh, K. Sugano, T. Tsuchiya, and O. Tabata, "Analysis of acceleration sensitivity in MEMS tuning fork gyroscope", in *Proc.* of The 16th International Conference on Solid-State Sensors Actuators and Microsystems (Tranasducer's 11), Beijing, China, pp.2706-2709 (2011).
3) Thakur Praveen Singh, K. Sugano, T. Tsuchiya, and O. Tabata, "Analysis of acceleration sensitivity in frequency decoupled MEMS tuning fork gyroscope", EUROSENSORS XXV conference, Athens, Greece, Procedia Engineering, Vol. 25, pp.1233-1236 (2011).
4) Thakur Praveen Singh, K. Sugano, T. Tsuchiya, and O. Tabata, "Vibration Analysis of Coupled Vertical Resonators for Acceleration Sensitivity reduction of out-of-plane Vibratory Gyroscopes", MRS Spring Meeting, San Francisco, USA (2012).